Deformation experiments of bubble and crystal bearing magmas: rheological and microstructural analysis

M. Pistone, Luca Caricchi, Pete Ulmer, L. Burlini, Paola Ardia, Éric Reusser, Federica Marone, Laurent Arbaret

Deformation experiments of bubble- and crystal-bearing magmas: Rheological and microstructural analysis

Mattia Pistone,[1] Luca Caricchi,[2] Peter Ulmer,[1] Luigi Burlini,[1,3] Paola Ardia,[4] Eric Reusser,[1] Federica Marone,[5] and Laurent Arbaret[6]

Received 29 October 2011; revised 24 March 2012; accepted 27 March 2012; published 23 May 2012.

[1] Simple shear deformation experiments on three-phase, hydrous, haplogranitic magmas, composed of quartz crystals (24–65 vol.%), CO_2-rich gas bubbles (9–12 vol.%) and melt in different proportions, were performed with a Paterson-type rock deformation apparatus. Strain rates from $5 \cdot 10^{-6}$ s^{-1} to $4 \cdot 10^{-3}$ s^{-1} were applied at temperatures between 723 and 1023 K and at pressure of 200 MPa. The results show that the three-phase suspension rheology is strongly strain rate dependent (non-Newtonian behavior). Two non-Newtonian regimes were observed: shear thinning (viscosity decreases with increasing strain rate) and shear thickening (viscosity increases with increasing strain rate). Shear thinning occurs in crystal-rich magmas (55–65 vol.% crystals; 9–10 vol.% bubbles) as a result of crystal size reduction and shear zoning. Shear thickening prevails in dilute suspensions (24 vol.% crystals; 12 vol.% bubbles), where bubble coalescence and outgassing dominate. At intermediate crystallinity (44 vol.% crystals; 12 vol.% bubbles) both shear thickening and thinning occur. Based on the microstructural observations using synchrotron radiation X-ray tomographic microscopy, bubbles can develop two different shapes: oblate at low temperature (<873 K) and prolate at high temperature (>873 K). These differences in shape are caused by different conditions of flow: unsteady flow, where the relaxation time of the bubbles is much longer than the timescale of deformation (oblate shapes); steady flow, where bubbles are in their equilibrium deformation state (prolate shapes). Three-phase magmas are characterized by a rheological behavior that is substantially different with respect to suspensions containing only crystals or only gas bubbles.

Citation: Pistone, M., L. Caricchi, P. Ulmer, L. Burlini, P. Ardia, E. Reusser, F. Marone, and L. Arbaret (2012), Deformation experiments of bubble- and crystal-bearing magmas: Rheological and microstructural analysis, *J. Geophys. Res.*, *117*, B05208, doi:10.1029/2011JB008986.

1. Introduction

[2] The ascent of hydrous magmas through the crust is accompanied by decreasing pressure, resulting in volatile oversaturation and crystallization [e.g., *Blundy et al.*, 2006]. In general, magmas are multiphase mixtures composed of crystals and gas bubbles suspended in a silicate melt phase. The relative proportions of these phases and their interaction control the rheological behavior, the modality of emplacement and the eruption of magmas.

[3] The rheological behavior of silicate melt is controlled by various factors, such as chemical composition, volatile content (mainly water), temperature, pressure, thermal history and strain rate. The presence of crystals produces a strongly nonlinear increase of viscosity with crystal content and the appearance of non-Newtonian behavior [e.g., *Chong et al.*, 1971; *Lejeune and Richet*, 1995; *Caricchi et al.*, 2007; *Mueller et al.*, 2010]. The presence of gas bubbles introduces additional complexity, in which viscosity can either increase or decrease with vesicularity [*Llewellin and Manga*, 2005]. The coexistence of crystals and bubbles demands consideration of the interaction between the different phases in magmas.

[4] Over the last three decades, numerous studies including field relationships, experimental determinations and numerical modeling were conducted to determine the rheology of magmas. These studies focused on the physical properties of crystal-bearing, bubble-free systems [*Arbaret*

[1]Department of Earth Sciences, Institute for Geochemistry and Petrology, ETH-Zurich, Zurich, Switzerland.
[2]Department of Earth Sciences, University of Bristol, Bristol, UK.
[3]Deceased 22 December 2009.
[4]Department of Geology and Geophysics, University of Minnesota, Minneapolis, USA.
[5]Swiss Light Source, Paul Scherrer Institute, Villigen, Switzerland.
[6]Institut des Sciences de la Terre d'Orléans, UMR 6113, Université d'Orléans/Centre National de la Recherche Scientifique, Orléans, France.

Corresponding author: M. Pistone, Department of Earth Sciences, Institute for Geochemistry and Petrology, ETH-Zurich, Clausiusstr. 25, CH-8092 Zurich, Switzerland. (mattia.pistone@erdw.ethz.ch)

0148-0227/12/2011JB008986

et al., 2007; *Bagdassarov and Dorfman*, 1998a; *Bagdassarov and Dorfman*, 1998b; *Caricchi et al.*, 2007, 2008; *Champallier et al.*, 2008; *Cordonnier et al.*, 2009; *Deubener and Brückner*, 1997; *Kohlstedt and Holtzman*, 2009; *Lavallée et al.*, 2007, 2008; *Lejeune and Richet*, 1995; *Mecklenburgh and Rutter*, 2003; *Mueller et al.*, 2010; *Paterson*, 2001; *Petford*, 2003; *Rutter et al.*, 2006; *Smith*, 1997] or bubble-bearing, crystal-free systems [*Bagdassarov and Dingwell*, 1992, 1993a, 1993b; *Kameda et al.*, 2008; *Lejeune et al.*, 1999; *Llewellin et al.*, 2002; *Okumura et al.*, 2006, 2008, 2009, 2010; *Rust and Manga*, 2002a, 2002b; *Stein and Spera*, 1992, 2002].

[5] To date, the properties of three-phase mixtures have not been intensively studied. To our knowledge, only one study on crystal- and bubble-bearing magmas has been reported: *Bagdassarov et al.* [1994] performed oscillatory experiments on a synthetic rhyolite containing crystals and bubbles under atmospheric pressure to determine the viscoelasticity of three phase mixtures in the temperature range 1023–1323 K. There are no physical models available describing the rheological behavior of three-phase magmatic mixtures. The combination of rheological and microstructural information collected in this study will allow us to develop a physical model, thereby increasing our understanding of the dynamics of magma migration in the crust and retrieving information on the physical properties of magmas erupted by volcanoes from the analysis of their microstructures [*Mastin*, 2005].

2. Analytical Methods

[6] The following analytical methods have been employed to determine compositional, volumetric and microstructural properties of starting materials before and after synthesis and of experimentally deformed samples.

2.1. Electron Microprobe (EPMA) and Scanning Electron Microscopy (SEM) Analyses

[7] Glass compositions were analyzed with a JEOL-JXA-8200 electron microprobe using 15 kV acceleration voltage, 2–5 nA beam current and 10–20 μm beam diameter. The counting time was set to 20 s on the peak and 10 s on each background position. Natural and synthetic standards were employed and data were ϕ–ρ–z corrected.

[8] Backscattered (BSE) images of the crystal- and bubble-bearing materials were acquired, either by electron microprobe or with a JEOL-JSM-6390LA SEM. An accelerating voltage of 15 kV and a probe current of 10 nA (EPMA) and 1 nA (SEM) were employed to obtain good contrast between melt and quartz grains. Images were analyzed for estimating volumetric content of the different phases using the Java-based software JMicro-Vision v1.2.7 (http://jmicrovision.com). Two classes of objects (voids/bubbles and crystals) were selected for size distribution analysis utilizing the image processing software ImageJ 1.43s [*Abramoff et al.*, 2004].

2.2. Synchrotron-Based X-Ray Tomographic Microscopy and 3D Visualization

[9] Cylindrical cores of 2 mm outer diameter and 2–4 mm length were drilled out from the starting materials and the outer portions of deformed samples, where the torsional deformation is highest. Cylinders are isotropic in the scan plane and, thus, represent the best geometry to capture maximum volume [*Ketcham and Carlson*, 2001]. Synchrotron-based X-ray Tomographic Microscopy (SRXTM) delivered high-resolution volumetric (3D) information in a non-destructive manner. These experiments profit from a high flux monochromatic X-ray beam and were performed at the TOMCAT (Tomographic Microscopy and Coherent Radiology Experiments [*Stampanoni et al.*, 2006]) beamline at the Swiss Light Source (Paul Scherrer Institute, Villigen, Switzerland). Specimens were mounted on a carbon fiber rod and rotated 180° during acquisition. Between 2000 and 3000 raw projections were acquired for each scan. The energy was set to 20 keV and the exposure time to 100 ms. The acquired images consist of 2048 × 2048 pixels and the magnification was 10×, resulting in an isotropic voxel size of 0.74 μm. Tomographic reconstructions were performed using a highly optimized algorithm based on Fourier methods [*Marone et al.*, 2010]. ImageJ 1.43s software was used to process the raw projections and to generate image stacks. The 3D visualization and analysis of gas bubbles were performed using ParaView 3.8-RC1 (Kitware, Inc.) and Avizo® Fire (Visualization Sciences Group) software. Quartz crystals were not selected for segmentation because of their very low density contrast with respect to the silicate glass matrix.

2.3. Determination of Water and Carbon Dioxide Concentrations

2.3.1. Karl-Fisher Titration (KFT)

[10] Water contents in powders (before the synthesis) and glasses (after the synthesis) were determined by Karl-Fischer titration [*Fischer*, 1935] using a CA 100 Moisture Meter (COSA Instruments Mitsubishi Chemical Corporation). The apparatus was calibrated with synthetic muscovite crystals (3.91–4.08 wt.%) using standard techniques as outlined in *Behrens et al.* [1996] with a background of 0.15–0.27 μg/s (corresponding to a measurement offset of 0.003–0.005 wt.%). Samples were progressively heated from room temperature to 1500 K. Precision of replicate analysis is about ±0.15 wt.% H_2O.

2.3.2. CO_2-Coulometry

[11] The carbon dioxide content in glasses and powders was measured with a CM 5200 CO_2-Coulometer at the Limno-Geology Laboratory of ETH. Applying the technique of *Herrmann and Knake* [1973] we performed a preliminary calibration with analytical grade calcite powder (Merck, 99.0 wt.% $CaCO_3$) and an in-house standard with a CO_2 content of 0.50 ± 0.01 wt.% [*Schwarzenbach*, 2011]. The CO_2-analyses were carried out in an oxygen current. Samples were weighted and sealed in tin capsules (5 mm in diameter and 9 mm in length) and melted at 1323 K. Background counts amounted to 8.21 μg/s (equivalent to a measurement offset of 0.003–0.005 wt.%). The relative precision is typically ±0.5% for samples containing more than about 1800 ppm of CO_2.

2.3.3. Fourier-Transform Infrared Spectroscopy (FTIR)

[12] Water and carbon dioxide contents of undeformed glasses were measured at CNRS - Institut des Sciences de la Terre d'Orléans (France) using a Nicolet Magna 760 Fourier transform infrared (FTIR) spectrometer, coupled with a

Table 1. Chemical and Modal Compositions of Starting Materials[a]

Series	Specimen	SiO_2 (EPMA)	Al_2O_3 (EPMA)	K_2O (EPMA)	Na_2O (EPMA)	CO_2 (FTIR)	CO_2 (Coul.)	H_2O (FTIR)	H_2O (KFT)
HGG	HGG	75.56 (0.09)	13.23 (0.02)	4.99 (0.01)	3.37 (0.07)	-	-	2.52 (0.06)	1.58 (0.40)
	$HGGB_3$-30					624 (40)		2.26 (0.04)	
$HGGB_3$	$HGGB_3$-50	73.77 (0.22)	13.11 (0.12)	4.40 (0.04)	3.95 (0.02)	-	0.40–0.56 (0.01)	-	2.58 (0.15)
	$HGGB_3$-60					-		-	
	$HGGB_3$-70					-		-	

Series	Specimen	μ^b	Φ^b	β^b	μ^c	Φ^c	β^c	ρ before HIP (kg/m^3)	ρ after HIP (kg/m^3)
HGG	HGG/[3]	1.00	0.00	0.00	0.97–0.98	0.00	0.02–0.03	2246	2245 (3) [1]
	$HGGB_3$-30/[8]	0.64	0.24	0.12	0.62–0.66	0.22–0.25	0.12–0.13	2367	2074 (13) [3]
	$HGGB_3$-50/[6]	0.44	0.44	0.12	0.44–0.49	0.42–0.45	0.09–0.11	2448	2192 (6) [1]
$HGGB_3$	$HGGB_3$-60/[3]	0.35	0.55	0.10	0.32–0.36	0.54–0.57	0.10–0.11	2488	2253 (12) [4]
	$HGGB_3$-70/[4]	0.26	0.65	0.09	0.24–0.27	0.64–0.66	0.09–0.10	2529	2346 (4) [1]

[a]Representative EPMA analyses of the bulk matrix glass; FTIR spectrometry, KFT and CO_2-Coulometry results on water and carbon dioxide contents of the starting glasses (in wt.%; CO_2 (FTIR) in ppm). Relative crystal (Φ), bubble (β) and glass (μ) contents of the starting material and their respective densities (ρ). Density values of the material before HIP are estimated by calculations based on chemical composition, including water and carbon dioxide contents (HGG glass: ρ = 2246 kg/m^3; quartz crystals: ρ = 2650 kg/m^3); density values of glasses after HIP are from pycnometer measurements. Values in round and square brackets represent relative average deviations and average standard errors respectively. Average standard errors: 0.01 wt% for H_2O and 5 ppm for CO_2 (FTIR); 0.01 wt% CO_2 (coulometry); 0.15 wt.% for H_2O (KFT); [number] = number of sample cores analyzed via helium pycnometry.
[b]Measured via pycnometry.
[c]Measured via image analysis.

Nicolet Nic-Plan microscope [*Gaillard et al.*, 2001]. Samples were fixed in epoxy and doubly polished. Except for pure glasses, samples containing the lowest crystal contents and low bubble contents were selected for FTIR measurements (bubble-, crystal- and fracture-free glass areas), since the FTIR instrument has a limited spatial resolution (>25–35 μm [*Devine et al.*, 1995]). The focal point was moved through the entire sample to ensure that clear optical paths were selected. Thick samples were prepared (>100 μm) to collect high-resolution spectra for carbon dioxide. Spectra were collected between 4000 and 6000 cm^{-1} for water and between 1350 and 3000 cm^{-1} for carbon dioxide quantification. They were evaluated employing a baseline correction described by *Dingwell et al.* [1996]. For the rhyolitic compositions investigated in this study, molar absorption coefficients for the hydroxyl group (4500 cm^{-1}) and molecular water (5230 cm^{-1}) were taken from *Okumura and Nakashima* [2005]; the molar absorptivity for the infrared absorption band of CO_2 (2349 cm^{-1}) was taken from *Behrens et al.* [2004]. Carbonate groups (1400–1500 cm^{-1}) were not detectable and were not expected to be present in (highly polymerized) rhyolitic glasses where CO_2 should exclusively occur as molecular CO_2 [*Blank and Brooker*, 1994]. The presence of quartz crystals and gas bubbles in the analyzed areas led to under- and over-estimations of CO_2 contents, respectively; such results were excluded from the final evaluation of CO_2 content, as evaluated by successive optical inspection of analysis areas. The H_2O and CO_2 contributions of air were examined and found to be negligible (<1% of both volatile species band intensity) by comparison of background spectra measured at different times of the same day.

2.4. Density Measurements by Pycnometry

[13] Given the densities of the glass phase and solid quartz crystals at room conditions, the relative volumes of crystals, bubbles and glass of synthetic starting materials were estimated by density measurements. Sample cores were weighed in air at 298 K using a precision scale. The volume of the cores was measured by helium pycnometry with a 10 cm^3 sample cell (Micromeritics Accupyc 1330). The interconnected porosity was estimated from the difference between the geometrical volume (measured by caliper) and the volume measured by the pycnometer [*Caricchi et al.*, 2008].

3. Starting Materials

[14] Starting materials for the experiments were prepared with the aim of producing suspensions of silicate melt, crystals and gas-pressurized bubbles.

3.1. Composition and Preparation of Volatile-Bearing Haplogranite Powders

[15] The silicate glass represents a hydrous, haplogranitic composition (anhydrous normative composition: $Ne_{14}Ks_{18}Qz_{68}$; HGG of *Ardia et al.* [2008]) containing H_2O and/or CO_2 (Table 1). The principal advantage of this composition is its chemical inertness [*Caricchi et al.*, 2007]. This is fundamental to maintain control on the composition of the silicate melt and on the crystal fraction during the experiments. Furthermore, the rheology and water solubility of the employed haplogranitic glass under the experimental conditions of this study have been well characterized [*Dingwell et al.*, 1996; *Holtz et al.*, 1992a, 1992b, 1995; *Malfait et al.*, 2011; *Schulze et al.*, 1996]. The H_2O- and CO_2-rich haplogranitic composition was obtained by mixing fine-grained (D_{50} = 1 μm) synthetic oxides (SiO_2, Al_2O_3, Na_2SiO_3), hydroxides ($Al(OH)_3$, $K_2Si_3O_7 \cdot 3H_2O$) and carbonates (Na_2CO_3, K_2CO_3) in appropriate proportions. All oxide powders were dried at 383–393 K prior to weighing and mixing, except for SiO_2 that was fired at 1273 K.

[16] The solubilities of water and carbon dioxide were estimated by the thermodynamic model of *Papale et al.* [2006] for rhyolitic composition at the conditions of the synthesis. To control the volume content of bubbles in the starting material and decrease the viscosity of the melt phase to the desired values, H_2O-saturated and CO_2-oversaturated

mixtures were prepared. Carbon dioxide content was fundamental in order to maintain constant bubble volume during the experiments, because of the lower solubility and compressibility of carbon-rich gases with respect to water-rich fluids [*Kerrick and Jacobs*, 1981]. The H_2O and CO_2 contents of the starting powders were verified by KFT and CO_2-coulometry, respectively. Replicate analyses for each sample were performed and resulted in 2.07 and 2.71 wt% H_2O in HGG and $HGGB_3$ respectively, and 2.81 wt% CO_2 in $HGGB_3$ (HGG is CO_2-free glass; see Table 1).

3.2. Preparation of Quartz-Bearing Samples

[17] Quartz crystals (DORSILIT 2500: 98.90 wt.% SiO_2; 0.41 wt.% Al_2O_3; 0.02 wt.% Fe_2O_3; 0.04 wt.% TiO_2; Alberto Luisoni AG, Switzerland) were employed as suspended particles (rough particles with aspect ratios between 1.0 and 3.5) for the experiments. The small amounts of titano-ferruginous impurities on the surface of the quartz grains facilitate wetting by the silicate melt during high temperature and pressure synthesis [*Mangan et al.*, 2004a, 2004b; *Rutter et al.*, 2006]. Crystals were fired for five hours in a one-atmosphere muffle furnace at 1273 K to dry the surfaces and to remove any fluid inclusions. Their size was selected by sieving and checked by Malvern Laser Diffraction Grain Sizer at the Limno-Geology Laboratory of ETH. The three-dimensional grain size distribution shows a mean value of 68 μm with a sorting of 2.43 and a positive skewness of 0.37. Considering the rather high melt viscosity ($\sim 10^8$ Pa $\cdot$ s at 973 K using the model of *Giordano et al.* [2008]), a relatively large grain size (63–125 μm) has been selected to ensure sufficient permeability for the melt to flow in response to applied mechanical deformation during experiments [*Rutter et al.*, 2006], while minimizing the tendency for impingement cracking during hot pressing and densification of the mixture [*Mecklenburgh and Rutter*, 2003]. After sieving quartz was again dried in air at 1173 K. To mix the powders with the appropriate amount of quartz particles, densities of the employed glasses (at 298 K and 1 atm) were estimated with the equation provided by *Lange and Carmichael* [1987]. Only the water content (previously determined by KFT) was included in the calculations, since CO_2 is basically insoluble at the conditions of synthesis.

[18] The previously prepared powders were thoroughly mixed with quartz crystals to obtain four different starting samples containing 30, 50, 60 and 70 vol.% particles (on a bubble-free base). The quartz crystal content in the starting powders was checked by powder X-ray diffractometry following the method of *Lejeune and Richet* [1995] using a Bruker AXS, D8 Advance diffractometer. We found a close correspondence between crystal contents prepared by weighing the components in the mixtures and powder X-ray diffraction: $HGGB_3$-50 = 51 $\pm$ 3 vol.%; $HGGB_3$-60 = 56 $\pm$ 5 vol.%; $HGGB_3$-70 = 69 $\pm$ 3 vol.%. At low concentration (30 vol.% in $HGGB_3$-30) the XRD-based estimation of the crystal concentration failed (maximum estimated concentration: 16 vol.% in $HGGB_3$-30).

3.3. Experimental Synthesis: Generation of Gas-Pressurized Bubbles

[19] The starting materials were pressed into cylindrical stainless steel canisters (220 mm long, 35 mm inner diameter, 3 mm wall thickness) using a uniaxial cold press. The powder was separated from the inner walls of the canister by a thin (25 μm) molybdenum foil to avoid chemical contamination. Filled canisters were stored at 383 K to remove any adsorbed humidity and welded shut by arc-welding. Tightness of the seal was checked under vacuum in a water bath and by weighing.

[20] The canisters were hot isostatically pressed (HIP) for 24 h in a large capacity (170 mm in diameter; 500 mm high), industrial, internally heated pressure vessel (Sinter-HIP-Kompaktanlage; ABRA Fluid AG, Switzerland) at 124 MPa and 1373 K at the Rock Deformation Laboratory of ETH. The temperature was nearly constant over the entire volume of the vessel (maximum difference of 18 K along the length of a sample).

[21] The cooling process was divided in two steps: a rapid decrease of temperature (60 K/minute) down to the inferred glass transition temperature (viscosity at T_g considered equivalent to 10^{12} Pa $\cdot$ s) followed by slow cooling (0.6 K/minute) to room temperature. The first cooling segment aimed at avoiding any crystallization; the second segment was conducted to obtain thermally relaxed glasses [*Webb and Dingwell*, 1990a; *Dingwell and Webb*, 1990; *Dingwell et al.*, 1993; *Dingwell*, 1995]. During cooling the confining pressure decreases with decreasing temperature. Decompression occurring during cooling (3.76 MPa/minute in the first cooling stage; 0.13 MPa/minute in the second one) is not pronounced and nucleation of eventual bubbles is inferred to be negligible [*Hurwitz and Navon*, 1994]. A total of 4 samples of haplogranitic composition ($HGGB_3$), with different crystal and bubble contents were produced (Table 1). All capsules containing carbonates showed signs of inflation (especially at container lids) after synthesis, indicating that some gas exsolved from the melt and did not produce bubbles. The weight of the canisters after the HIP run was compared with the initial weights and revealed no significant differences (less than 3 g over 400 g in total) suggesting that only insignificant amounts of gas was released during the synthesis. An additional glass containing neither crystals nor bubbles (HGG) was synthesized to measure the properties of the melt phase.

3.4. Characterization of Starting Materials

3.4.1. Glass Compositions: Chemical Homogeneity and Stability

[22] Glass compositions were analyzed by electron microprobe (Table 1). No significant chemical changes were detected in the haplogranitic glasses after synthesis due to resorption of quartz, crystallization, or contamination by molybdenum. Analyses of glasses from experimentally deformed samples confirm the chemical stability of the investigated system ($\Delta SiO_2 = -0.04$ wt.%, $\Delta Al_2O_3 = -0.21$ wt.%, $\Delta Na_2O = -0.02$ wt.%, $\Delta K_2O = +0.03$ wt.%).

[23] Water and carbon dioxide concentrations of $HGGB_3$ glasses (FTIR) are reported in Table 1. KFT measurements of H_2O in the hydrous glasses corrected for crystal content [*Champallier et al.*, 2008] are, likewise, reported in Table 1 and are generally in good agreement with FTIR measurements. The results of CO_2-coulometry corrected for crystal and bubble content (ground glasses had an average grain size of 44 μm; bubbles were present) are reported in Table 1. The amounts of CO_2 contained in the gas phase (bubbles) were estimated by mass balance calculations considering

Table 2. Summary of Representative Bubble Number Densities (BNDs) of Starting Materials[a]

Sample	Total Number of Bubbles	Total Average Area of Analyzed Image (mm^2)	V_B (μm^3)	V_B (mm^3)	BND (mm^{-3})
$HGGB_3$-30	4375	6.48	1.02E+08	1.02E-01	5.16E+03
$HGGB_3$-50	4912	6.48	2.00E+07	2.00E-02	2.95E+04
$HGGB_3$-60	5774	6.50	1.68E+07	1.68E-02	3.44E+04
$HGGB_3$-70	3343	6.52	1.13E+07	1.13E-02	3.54E+04

[a]Abbreviations: V_B = total volume of bubbles; BND = bubble number density.

600 ppm of dissolved CO_2 (Table 1) in the glass; the amounts of CO_2 in the gas phase are 0.34–0.50 wt%.

3.4.2. Relative Crystal, Bubble and Glass Contents

[24] The relative crystal, bubble and glass contents of the synthetic starting materials ($HGGB_3$) were determined by two methods:

[25] (1) Density difference between the crystal-bearing powders before and the crystal- and bubble-bearing samples after synthesis using pycnometry. The reference densities of pure glass (HGG; ρ = 2246 kg/m^3; Table 1) and quartz crystals (ρ = 2650 kg/m^3) at room conditions were previously estimated with the method of *Lange and Carmichael* [1987]. 57 sample cores were drilled in different portions of the canisters to check for homogeneity. The relative contents of crystals and glass were subsequently rescaled to account for the presence of bubbles and, finally, the total bubble content was corrected by adding the interconnected porosity to the closed porosity (Table 1).

[26] (2) Image analysis. 52 backscattered electron (BSE) images of the starting materials with an area of about 2–6 mm^2 taken in different portions of the canisters were evaluated and results are in close agreement with those obtained by density measurements (Table 1). The sample HGG represents an exception, as it shows a very limited amount of very tiny isolated bubbles (2 vol.%), not detected by the density measurements.

3.4.3. Bubble Size Distribution (BSD) and Bubble Number Density (BND)

[27] The bubble size distribution (BSD) was measured in BSE images. We did not determine the three-dimensional diameter of the bubbles as reported in previous studies [*Rust and Manga*, 2002b; *Larsen et al.*, 2004; *Gardner*, 2007]. The three-dimensional recalculation of the distributions observed in two dimensions was estimated due to the large number of bubbles analyzed in differently oriented 2D sections through the sample. Each analysis was performed on areas of 2–6 mm^2 (Table 2). Analysis included determination of bubble area and sphericity. Results include the total volume of bubbles (V_B; in μm^3 and mm^3) and the bubble number density (BND; in mm^{-3}) in the selected sample area (in mm^2) for different bins (size class width of 5 μm in bubble diameter).

[28] Analyses were performed on samples after the synthesis and after static experiments at a pressure of 200 MPa and a temperature of 773 K for different durations (maximum 1 h). In both series, starting materials and the central parts of deformed samples contain a volumetrically dominant proportion of bubbles with diameters ranging from 5 to 15 μm. Larger bubbles, up to 30 μm in diameter, are present in much lower number fraction, whereas even larger bubbles (up to 150 μm in diameter) are rather rare any volumetrically minor (Figure 1).

3.4.4. Microstructural Observations of the Starting Crystal- and Bubble-Bearing Glasses

[29] BSE images of $HGGB_3$ show homogeneous crystal, bubble and glass distributions (Figure 2). Quartz crystals display roughly isometric shape, do not show evidences of reaction during the synthesis and samples are free of microlites. Bubbles are spherical in shape (sphericity 0.8–0.9) and coalescence or near-coalescence of bubble pairs was not observed. Samples containing higher amounts of crystals ($HGGB_3$-60 and $HGGB_3$-70) exhibit numerous bubbles in proximity of solid particles; inversely, in specimens with lower degree of crystallinity ($HGGB_3$-30 and $HGGB_3$-50) most bubbles are not in contact with crystals. These observations suggest that during synthesis most bubbles nucleated homogeneously from the melt in agreement with previous studies on bubble nucleation indicating that quartz crystal surfaces are not efficient sites for bubble nucleation [*Hurwitz and Navon*, 1994; *Mangan et al.*, 2004a, 2004b].

4. Rheological Experiments and Microstructures

4.1. Methods and Apparatus

[30] Twenty-nine torsion (simple shear) deformation experiments were performed at the Rock Deformation Laboratory of the Geological Institute at ETH (P1xxx runs); three experiments (OR119, OR125 and OR127; Table 3) were carried out at the Rock Deformation Laboratory at CNRS - Institut des Sciences de la Terre d'Orléans (France). All experiments were performed using a high temperature and high pressure, internally heated Paterson gas-medium apparatus [*Paterson and Olgaard*, 2000]. The experiments were carried out isothermally (673–1023 K) over the entire sample length, at constant pressure (200 MPa; except for P1140, conducted at 250 MPa), and fixed bulk shear strain rate ($5 \cdot 10^{-6}$ s^{-1}–$4 \cdot 10^{-3}$ s^{-1}). During the experimental runs the deformation rate was changed by progressive strain rate stepping [*Caricchi et al.*, 2007; *Paterson and Olgaard*, 2000], from lower to higher deformation rates (except for the experiments P1353, P1491 and P1493; Table 3). The strain rate was increased only after steady stress conditions were achieved at a given strain rate. The conversion of internal torque to stress is computed by applying an appropriate value of the stress exponent of the sample [*Caricchi et al.*, 2007; *Caricchi*, 2008; *Paterson and Olgaard*, 2000]. Experiments were carried out under undrained conditions for the melt (no escape of melt from the sample) and drained conditions for fluids (escape of gas contained in the bubbles). The same cylindrical specimens already used for volume measurements by helium pycnometry (diameter between 11.91 and 15.01 mm, length between 2.51 mm and 16.47 mm; Table 3) were employed for the torsion experiments. The experiments were performed following the experimental procedure described in *Caricchi et al.* [2007] and *Caricchi* [2008].

[31] Iron and copper jackets were employed at higher (923–1023 K) and lower temperatures (673–923 K) respectively owing to different strength of these metals. The applied shear stresses were recorded by an internal load cell

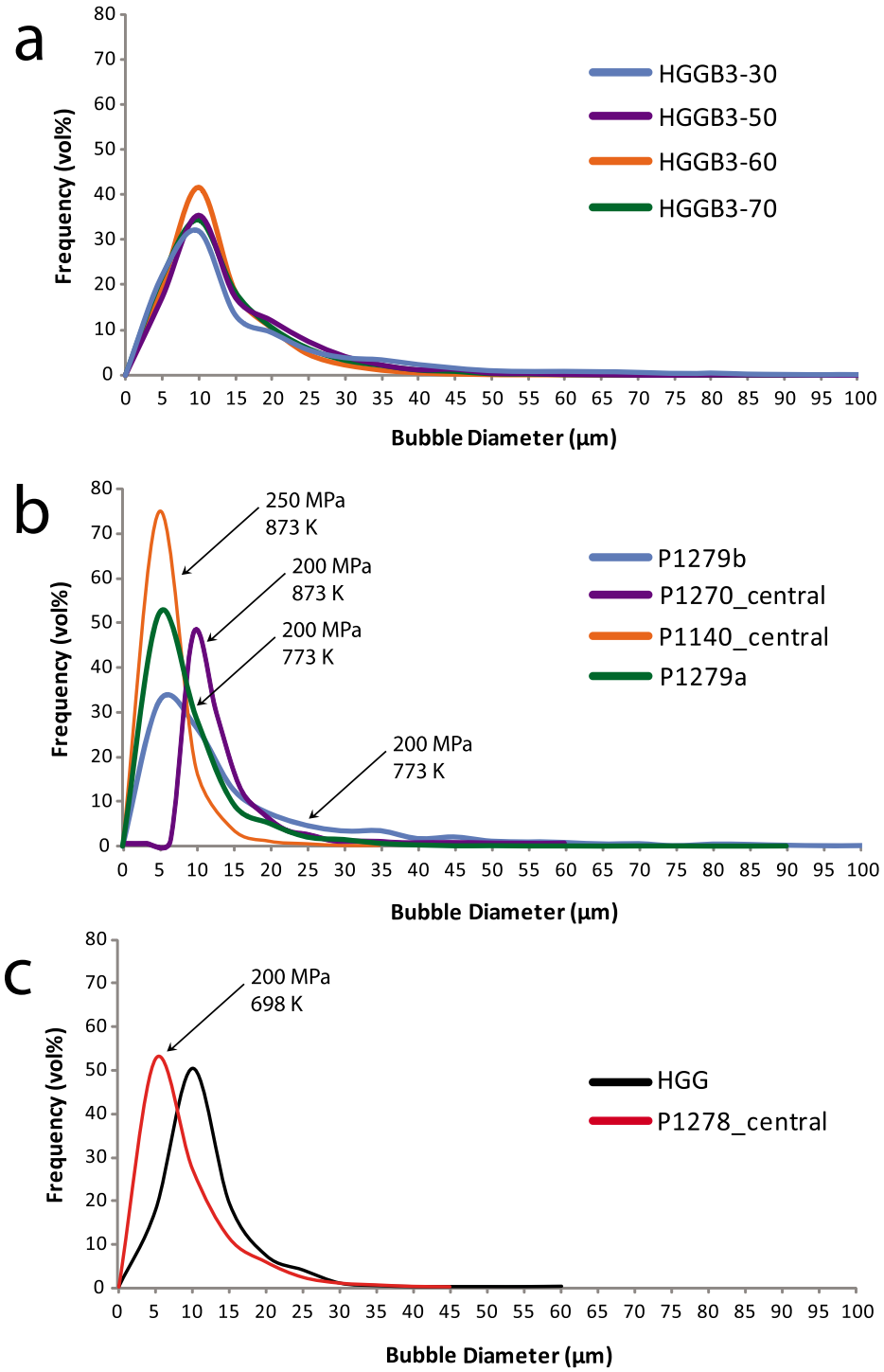

Figure 1. Bubble size distributions (BSDs): (a) starting material ($HGGB_3$-30, $HGGB_3$-50, $HGGB_3$-60, $HGGB_3$-70, where "-number" refers to approximately vol.% solid crystals on a bubble-free basis); (b) static experiments (P1279b and P1279a) and deformation-free sample cores from torsion experiments (P1270_central and P1140_central); (c) pure glass from HIP test (HGG) and static run (P1278_central). For further details, see text.

positioned inside the pressure vessel [*Paterson*, 1970], with a torque resolution of ±0.1 N · m [*Paterson and Olgaard*, 2000] that induces uncertainties in the reported shear stress values of ±1.5 MPa for a typical sample of 15 mm diameter in torsion tests [*Pieri et al.*, 2001]. Standard deviations for peak stresses and calculated viscosities do not exceed 0.29 MPa and 1 Pa · s respectively. Experiments were terminated by releasing the stress and immediately starting

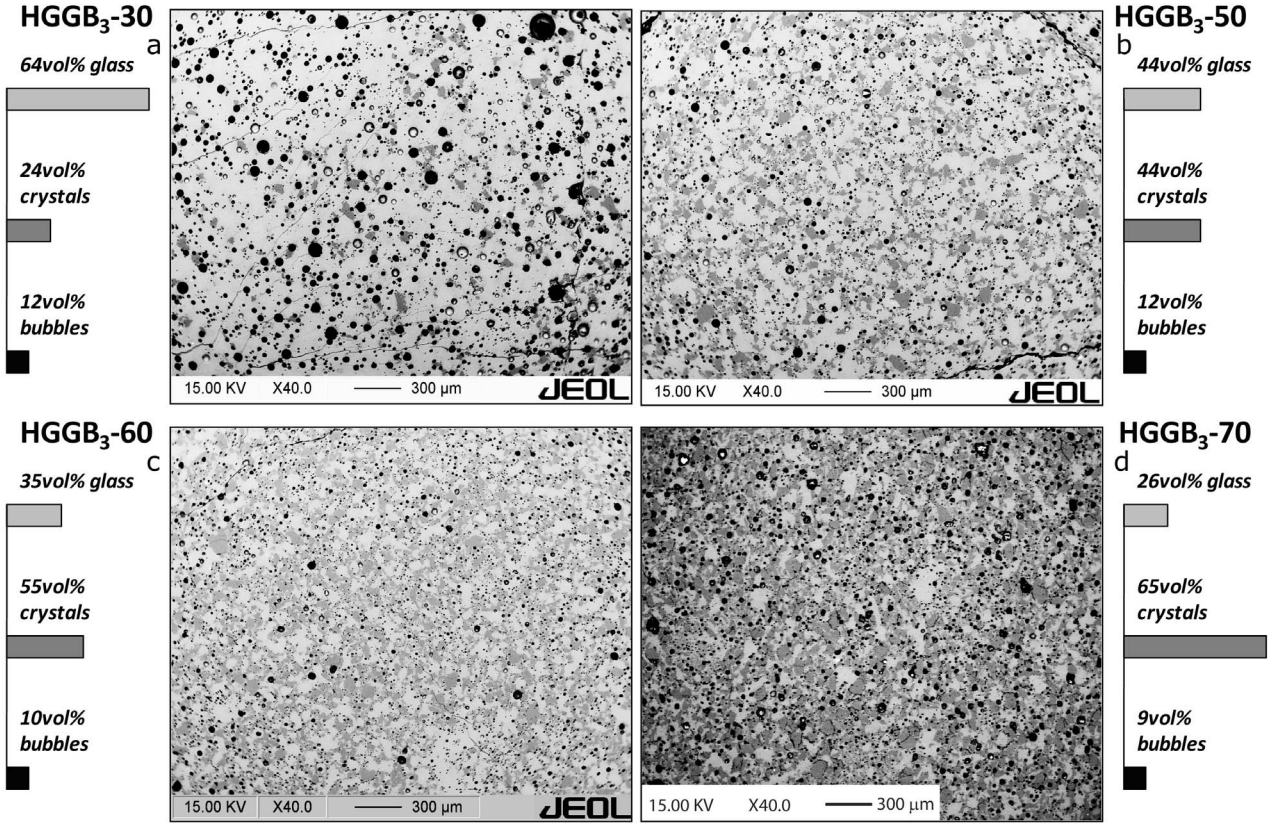

Figure 2. BSE images of the starting synthetic haplogranitic glasses (light-gray areas) containing quartz crystals (dark-gray areas) and bubbles (round black circles). (a) $HGGB_3$-30 ($\mu = 0.64$, $\Phi = 0.24$; $\beta = 0.12$); (b) $HGGB_3$-50 ($\mu = 0.44$, $\Phi = 0.44$; $\beta = 0.12$); (c) $HGGB_3$-60 ($\mu = 0.35$, $\Phi = 0.55$; $\beta = 0.10$); (d) $HGGB_3$-70 ($\mu = 0.26$, $\Phi = 0.65$; $\beta = 0.09$). Abbreviations: μ = melt volume fraction; Φ = crystal volume fraction; β = bubble volume fraction.

controlled cooling and depressurizing. Sample and jacket were immersed in epoxy. Longitudinal tangential cross sections, where the maximum strain is best appreciated, and radial cross sections, where the strain varies from zero at the center to maximum on the outer portion of the sample [*Paterson and Olgaard*, 2000], were cut and carefully polished for the subsequent analysis of the microstructures.

4.2. Experimental Results

[32] Experimental results are listed in Table 3. Bulk effective shear viscosity is calculated by deriving a flow law describing the variation of shear stress as function of the strain rate [*Brückner and Deubener*, 1997]. Figure 3 reports the *apparent shear viscosity* (ratio between shear stress and strain rate; *Caricchi et al.* [2007, 2008]) that is used for simplicity. In all experiments a first phase of linear stress increase with strain (elastic response) is followed by a transient yielding stage (strain hardening) and finally, by flow at constant values of stress. Most samples containing the same relative amount of crystals and bubbles were deformed at the same temperature to test experimental reproducibility. The experimental results have been divided in five groups:

[33] HGG (*crystal-free melt*, containing up to maximum 2 vol.% bubbles; Figure 3a)

[34] $HGGB_3$-30 (*dilute suspension*; 24 vol.% crystals and 12 vol.% bubbles; Figure 3b)

[35] $HGGB_3$-50 (*moderate crystallinity*; 44 vol.% crystals and 12 vol.% bubbles; Figure 3c)

[36] $HGGB_3$-60 (*high crystallinity*; 55 vol.% crystals and 10 vol.% bubbles; Figure 3d)

[37] $HGGB_3$-70 (*crystal mush*; 65 vol.% crystals and 9 vol.% bubbles; Figure 3e)

[38] Results for each group are presented in terms of stress versus shear strain and logarithm of apparent viscosity versus shear strain. Relative viscosities (η_r = suspension viscosity/suspending fluid viscosity [*Rust and Manga*, 2002a]) versus shear strain rate are reported in Figure 4.

4.2.1. HGG: Crystal-Free Melt

[39] The viscosity of the haplogranitic melt (HGG, Table 1) was measured between 673 and 773 K and the results are compared with various model calculations [*Giordano et al.*, 2008; *Hui and Zhang*, 2007; *Hui et al.*, 2008, 2009; *Zhang et al.*, 2003] and previous experimental viscosity determinations conducted on the same composition [*Ardia et al.*, 2008] at 550 MPa (Figure 5). Higher temperature (>773 K) experiments were impeded by the dominant effect of the copper sleeve over the sample during deformation. The experiments revealed both Newtonian and Non-Newtonian behavior of the pure melt in the temperature and strain rate range investigated ($4.80 \cdot 10^{-5}$ s^{-1} to $3.89 \cdot 10^{-3}$ s^{-1}). Non-Newtonian, shear-thinning behavior occurred with increasing strain rate resulting in decreasing

Table 3. Summary of Rheological Results From Torsion Experiments at 200 MPa Confining Pressure[a]

Starting Material	Experiment N°	l (mm)	ø (mm)	γ	γ' (s-1)	t (min)	M (N · m)	τ (MPa)	σ (N · m; MPa)	n	Log η effective (β + Φ + μ) (Pa · s)	Log η_r (β + Φ + μ)	σ (Pa · s)	Dominant Non-Newtonian Effect	$\Delta\eta_r$	Experimental Duration
HGG									*673 K Φ = 0.00 β = 0.00 μ = 1.00*							
	P1277	5.47	14.96	0.13	5.00E-05	44	26.82	40.80	0.02	1.0	11.91	−0.02	0.00	Shear Thinning	−0.35	50 minutes
				0.17	1.08E-04	6	25.61	38.95	0.00	1.0	11.56	−0.37	0.00			
									698 K Φ = 0.00 β = 0.00 μ = 1.00							
	P1278	6.38	14.91	0.04	4.80E-05	15	5.35	8.22	0.00	1.0	11.22	−0.02	0.00	Shear Thinning	−0.26	44 minutes
				0.14	1.15E-04	14	15.09	23.19	0.00	0.9	11.30	0.06	0.00			
				0.59	5.17E-04	15	35.54	47.78	0.00	1.7	10.97	−0.28	0.00			
									723 K Φ = 0.00 β = 0.00 μ = 1.00							
	P1353	2.68	14.83	0.13	1.13E-04	19	3.43	5.36	0.04	1.0	10.67	−0.02	0.00	Shear Thinning	−0.86	1 hour, 9 minutes
				0.27	4.58E-04	5	2.29	3.58	0.00	1.0	9.89	−0.80	0.00			
				0.44	7.26E-04	4	3.05	4.76	0.07	1.6	9.82	−0.88	0.01			
				0.45	**9.56E-06**	**26**	**4.52**	**7.06**	**0.02**	**1.0**	**11.87**	**1.17**	**0.00**			
				0.57	1.79E-04	11	4.79	5.65	0.05	50.0	10.50	−0.20	0.00			
				0.61	1.61E-04	4	4.34	6.78	0.00	1.1	10.62	−0.07	0.00			
									773 K Φ = 0.00 β = 0.00 μ = 1.00							
	P1352	3.09	14.84	0.98	4.58E-04	36	0.50	0.78	0.00	1.0	9.23	−0.02	0.00	Shear Thinning (?)	?	1 hours, 51 minutes + 1 hour
				2.09	**6.12E-04**	**30**	**3.48**	**5.42**	**0.00**	**1.0**	**9.95**	**0.70**	**0.00**			
				3.71	**1.24E-03**	**22**	**8.74**	**13.61**	**0.01**	**0.8**	**10.04**	**0.79**	**0.00**			
				5.95	**2.87E-03**	**13**	**12.07**	**15.68**	**0.00**	**2.6**	**9.74**	**0.49**	**0.00**			
				8.17	**3.89E-03**	**10**	**14.31**	**19.52**	**0.03**	**1.8**	**9.70**	**0.45**	**0.00**			
$HGGB_3$-30									*723 K Φ = 0.24 β = 0.12 μ = 0.64*							
	P1269	8.16	14.87	0.04	5.13E-05	11	1.30	2.02	0.00	1.0	10.57	−0.13	0.00	Shear Thickening ==>	0.37 and −0.39	48 minutes
				0.15	1.04E-04	18	6.15	9.52	0.02	1.0	10.96	0.26	0.00	Shear Thinning		
				0.52	4.81E-04	13	26.62	41.23	0.00	1.0	10.93	0.24	0.00			
				0.83	9.25E-04	6	28.28	33.85	0.01	10.8	10.56	−0.13	0.00			
	P1271	7.08	14.79	0.05	5.12E-05	17	4.74	7.46	0.00	1.0	11.16	0.46	0.00	Pseudo-Newtonian	−0.06	41 minutes
				0.12	1.11E-04	9	9.57	15.06	0.00	1.1	11.13	0.43	0.00			
				0.55	4.67E-04	15	37.21	58.58	0.07	1.1	11.10	0.40	0.00			
									773 K Φ = 0.24 β = 0.12 μ = 0.64							
	P1264	7.74	14.80	0.06	7.23E-05	15	0.15	0.23	0.00	1.0	9.48	0.23	0.00	Shear Thickening	0.72	1 hour, 12 minutes
				0.49	5.13E-04	14	4.54	7.14	0.00	0.6	10.14	0.89	0.00			
				3.31	1.10E-03	43	11.10	17.44	0.01	0.9	10.20	0.95	0.00			
	P1265	9.21	14.79	0.26	5.28E-04	8	1.04	1.64	0.00	1.0	9.49	0.24	0.00	Shear Thickening	0.43	33 minutes + 10 minutes
				0.58	1.07E-03	5	2.80	4.41	0.00	0.7	9.62	0.37	0.00			
				1.90	2.45E-03	9	8.61	13.56	0.00	0.7	9.74	0.49	0.00			
				3.64	2.53E-03	11	13.28	20.90	0.00	1.0	9.92	0.67	0.00			
	P1493	4.54	14.83	0.81	3.06E-04	17	3.32	5.19	0.01	1.0	10.23	0.98	0.00	Shear Thinning ==>	0.26 and −0.55	3 hours, 38 minutes +
				1.17	3.06E-04	20	3.44	5.38	0.01	1.0	10.24	0.99	0.00	Shear Thickening ==>	and −0.27	2 hours, 11 minutes
				1.35	9.96E-05	27	2.99	3.64	0.01	7.9	10.56	1.31	0.00	Shear Thinning		
				1.60	7.02E-05	64	3.14	4.29	0.00	1.9	10.78	1.53	0.00			
				1.65	9.87E-05	8	3.13	4.88	0.01	1.0	10.69	1.44	0.00			

Table 3. (continued)

Starting Material	Experiment N°	l (mm)	ø (mm)	γ	γ' (s-1)	t (min)	M (N · m)	τ (MPa)	σ (N · m; MPa)	n	Log η effective ($\beta + \Phi + \mu$) (Pa · s)	Log ηr ($\beta + \Phi + \mu$)	σ (Pa · s)	Dominant Non-Newtonian Effect	$\Delta\eta_r$	Experimental Duration
				2.20	3.05E-04	21	3.42	4.11	0.01	12.6	10.13	0.88	0.00			
				2.51	5.12E-04	10	3.77	6.28	0.01	5.3	10.09	0.84	0.00			
				2.98	5.08E-04	16	4.90	7.65	0.01	1.0	10.18	0.93	0.00			
				3.43	1.00E-03	8	10.16	15.87	0.02	0.9	10.20	0.95	0.00			
				3.72	5.10E-04	10	8.41	10.67	0.01	3.6	10.32	1.07	0.00			
				4.80	1.00E-03	17	9.97	12.03	0.02	11.2	10.08	0.83	0.00			
$HGGB_3$-50									*773 K Φ = 0.44 β = 0.12 μ = 0.44*							
	P1272	6.65	14.88	0.07	4.95E-05	23	8.03	12.41	0.00	1.0	11.39	2.14	0.00	Shear Thinning	−0.60	56 minutes
				0.16	1.06E-04	15	16.67	25.76	0.00	1.0	11.38	2.13	0.00			
				0.76	5.37E-04	18	26.36	33.10	0.00	3.5	10.79	1.54	0.00			
	P1275	5.45	14.89	0.08	4.95E-05	26	9.52	14.68	0.00	1.0	11.46	2.21	0.00	Shear Thinning	−0.72	50 minutes + 7 minutes
				0.15	8.39E-05	15	18.20	28.08	0.00	0.8	11.52	2.27	0.00			
				0.47	5.71E-04	9	28.83	36.13	0.00	4.2	10.80	1.55	0.00			
									823 K Φ = 0.44 β = 0.12 μ = 0.44							
	P1266	6.13	14.93	**0.10**	**1.98E-04**	**8**	**0.14**	**0.22**	**0.00**	**1.0**	**8.98**	**0.75**	**0.00**	Shear Thickening[c](?)	?	21 minutes + 11 minutes
				0.53	5.50E-04	13	5.93	9.08	0.03	1.0	10.21	1.99	0.00			
	P1268	6.50	14.91	0.02	5.01E-05	7	0.23	0.35	0.00	1.0	9.80	1.57	0.00	Shear Thickening ==> Shear Thinning[c]	0.74 and −0.51	1 hour, 31 minutes
				0.09	1.53E-04	7	1.99	3.06	0.00	0.5	10.30	2.07	0.00			
				0.55	5.21E-04	15	11.83	18.17	0.01	0.7	10.54	2.31	0.00			
				1.55	9.25E-04	28	20.55	31.57	0.02	1.0	10.53	2.30	0.00			
				3.39	1.91E-03	16	34.68	53.28	0.03	1.4	10.45	2.22	0.00			
				5.24	2.81E-03	11	40.12	51.37	0.06	2.7	10.26	2.03	0.00			
				7.03	4.26E-03	7	39.95	45.87	0.04	−96.4	10.03	1.80	0.00			
	P1276	6.62	14.88	0.05	8.66E-05	10	0.14	0.22	0.00	1.0	9.35	1.13	0.00	Shear Thickening ==> Shear Thinning	1.01 and −0.18	31 minutes
				0.22	4.59E-04	6	6.81	10.53	0.00	1.0	10.36	2.13	0.00			
				0.65	1.02E-03	7	14.88	23.00	0.00	1.0	10.35	2.12	0.00			
				1.37	2.03E-03	6	27.28	42.17	0.00	1.1	10.32	2.09	0.00			
				2.64	2.93E-03	7	32.49	43.95	0.00	2.1	10.18	1.95	0.00			
									873 K Φ = 0.44 β = 0.12 μ = 0.44							
	P1270	8.81	14.88	0.30	5.03E-04	10	1.57	2.43	0.00	1.0	9.68	2.42	0.00	Shear Thinning	−0.37	1 hour, 5 minutes + 16 minutes
				1.14	1.01E-03	14	3.26	5.04	0.02	1.0	9.70	2.44	0.00			
				2.84	2.01E-03	14	5.10	6.90	0.02	1.5	9.54	2.27	0.00			
				7.10	2.97E-03	24	6.02	8.14	0.02	2.4	9.44	2.18	0.00			
				7.69	3.20E-03	3	5.99	6.81	0.00	−17.0	9.33	2.07	0.00			
$HGGB_3$-60									*823 K Φ = 0.55 β = 0.10 μ = 0.35*							
	P1274	6.70	14.90	0.06	5.20E-05	18	4.60	7.09	0.00	1.0	11.12	2.90	0.00	Shear Thinning	−0.39	1 hour, 30 minutes
				0.17	1.13E-04	17	10.54	16.22	0.00	0.9	11.15	2.92	0.00			
				1.60	4.94E-04	48	38.14	58.73	0.01	1.1	11.07	2.85	0.00			
				1.66	1.06E-03	1	47.80	61.33	0.14	3.4	10.76	2.53	0.00			

Table 3. (continued)

Starting Material	Experiment N°	l (mm)	ø (mm)	γ	γ' (s-1)	t (min)	M (N · m)	τ (MPa)	σ (N · m; MPa)	n	Log η effective ($\beta + \Phi + \mu$) (Pa · s)	Log ηr ($\beta + \Phi + \mu$)	σ (Pa · s)	Dominant Non-Newtonian Effect	$\Delta\eta_r$	Experimental Duration
									873 K Φ = 0.55 β = 0.10 μ = 0.35							
	P1140[b]	3.05	11.91	0.08	4.74E-05	29	1.23	3.64	0.01	1.0	10.88	3.61	0.00	Shear Thinning	−0.29	3 hours, 3 minutes
				0.25	9.65E-05	29	2.30	6.78	0.00	1.2	10.84	3.58	0.00			
				2.31	2.91E-04	118	4.34	11.23	0.03	2.0	10.59	3.32	0.00			
	P1191	5.06	14.92	**0.11**	**5.05E-05**	**36**	**0.09**	**0.11**	**0.00**	**4.1**	**9.27**	**2.01**	**0.02**	Shear Thickening	0.11	1 hour, 13 minutes + 12 minutes
				0.24	1.01E-04	22	1.20	1.83	0.00	1.0	10.26	2.99	0.00			
				0.45	2.20E-04	15	3.37	5.04	0.00	1.0	10.36	3.10	0.00			
	P1193	5.33	14.95	0.12	5.03E-05	39	0.52	0.60	0.00	1.0	10.08	2.82	0.00	Shear Thickening	0.34	50 minutes
				0.20	1.16E-04	11	2.01	3.07	0.04	0.6	10.42	3.16	0.01			
	P1197	4.97	14.95	0.12	4.46E-05	45	0.25	0.30	0.00	7.2	9.82	2.56	0.01	Shear Thickening	0.27	1 hour, 31 minutes
				0.20	1.01E-04	13	0.58	0.88	0.00	1.4	9.93	2.67	0.00			
				0.47	2.99E-04	15	2.32	3.53	0.01	0.8	10.07	2.81	0.00			
				1.05	9.71E-04	10	7.83	11.93	0.01	0.9	10.09	2.83	0.00			
									873 K Φ = 0.55 β = 0.10 μ = 0.35							
	OR119	5.00	14.93	0.07	3.97E-05	28	3.55	5.50	0.01	1.0	11.14	3.87	0.00	Shear Thinning	−0.69	2 hours, 43 minutes
				0.16	8.65E-05	18	4.86	6.27	0.00	2.7	10.86	3.59	0.00			
				0.32	2.66E-04	10	10.11	13.70	0.01	1.5	10.71	3.45	0.00			
				6.12	9.00E-04	107	18.28	24.78	0.03	2.0	10.44	3.18	0.00			
	OR125	6.85	14.85	0.07	3.79E-05	30	1.39	2.17	0.01	1.0	10.75	3.49	0.00	Shear Thinning	−0.67	3 hours, 29 minutes
				0.16	8.32E-05	18	2.15	2.93	0.01	1.8	10.54	3.28	0.00			
				0.41	2.77E-04	15	3.92	5.33	0.01	2.0	10.28	3.02	0.00			
				8.42	9.13E-04	146	8.11	11.04	0.02	1.6	10.08	2.82	0.00			
	OR127	5.16	14.86	0.07	3.98E-05	29	1.23	1.92	0.01	1.0	10.68	3.41	0.00	Shear Thinning	−0.51	2 hours, 20 minutes
				0.14	8.67E-05	13	2.19	3.40	0.01	1.4	10.59	3.33	0.00			
				0.51	2.70E-04	23	4.50	6.12	0.01	1.6	10.35	3.09	0.00			
				4.59	9.02E-04	75	9.60	13.04	0.05	1.6	10.16	2.90	0.00			
									923 K Φ = 0.55 β = 0.10 μ = 0.35							
	P1273	6.62	14.89	0.02	5.00E-05	7	0.10	0.15	0.00	1.0	9.47	3.07	0.00	Shear Thinning	−0.27	47 minutes + 9 minutes
				0.29	5.06E-04	9	0.71	1.10	0.00	1.2	9.33	2.93	0.00			
				0.87	1.10E-03	9	1.58	2.44	0.00	1.0	9.35	2.95	0.00			
				2.00	2.09E-03	9	2.44	3.76	0.00	1.5	9.25	2.85	0.00			
				3.16	2.38E-03	8	3.41	5.26	0.00	1.0	9.34	2.94	0.00			
				4.26	3.69E-03	5	4.31	5.82	0.00	1.9	9.20	2.80	0.00			
$HGGB_3$-70									*873 K Φ = 0.65 β = 0.09 μ = 0.26*							
	P1198	4.63	14.84	0.18	4.68E-05	65	12.12	18.89	0.02	1.0	11.60	4.34	0.00	Shear Thinning	−0.85	2 hours, 9 minutes
				0.37	1.04E-04	30	18.15	24.75	0.01	2.0	11.37	4.11	0.00			
				0.74	3.06E-04	20	34.04	46.42	0.01	1.7	11.18	3.92	0.00			
				1.58	1.04E-03	14	46.49	58.86	0.03	3.9	10.75	3.49	0.00			
	P1205	5.94	14.86	0.13	4.65E-05	47	6.57	10.19	0.01	1.0	11.33	4.07	0.00	Shear Thinning	−0.35	1 hour, 32 minutes
				0.35	9.22E-05	40	10.58	16.42	0.01	1.4	11.25	3.98	0.00			
				0.44	2.95E-04	5	20.78	28.22	0.09	1.7	10.98	3.72	0.00			
	P1240	6.04	14.86	0.08	2.80E-04	5	7.64	11.86	0.01	1.0	10.62	3.36	0.00	Shear Thickening	0.13	7 minutes + 26 minutes
				0.16	6.69E-04	2	24.31	37.73	0.02	0.8	10.75	3.49	0.00			

Table 3. (continued)

Starting Material	Experiment N°	l (mm)	ø (mm)	γ	γ' (s-1)	t (min)	M (N · m)	τ (MPa)	σ (N · m; MPa)	n	Log η effective ($\beta + \Phi + \mu$) (Pa · s)	Log η_r ($\beta + \Phi + \mu$)	σ (Pa · s)	Dominant Non-Newtonian Effect	$\Delta\eta_r$	Experimental Duration
									883 K Φ = 0.65 β = 0.09 μ = 0.26							
	P1262	6.26	14.82	0.06	5.08E-05	20	3.60	5.63	0.00	1.0	11.04	3.96	0.00	Shear Thinning	−0.59	1 hour, 1 minute + 9 minutes
				0.15	1.08E-04	13	7.55	11.81	0.00	1.0	11.04	3.95	0.00			
				0.55	5.23E-04	13	21.22	29.06	0.02	1.5	10.75	3.66	0.00			
				1.57	1.46E-03	12	35.41	46.17	0.01	2.0	10.50	3.42	0.00			
				1.91	2.10E-03	3	43.56	59.64	0.29	1.8	10.45	3.37	0.00			
									923 K Φ = 0.65 β = 0.09 μ = 0.26							
	P1260	6.04	14.86	0.06	4.62E-05	21	3.36	5.22	0.00	1.0	11.05	4.65	0.00	Shear Thinning	−0.97	1 hour, 31 minutes
				0.16	9.09E-05	18	6.15	9.55	0.00	1.1	11.02	4.62	0.00			
				0.94	5.03E-04	26	14.15	21.97	0.02	2.1	10.64	4.24	0.00			
				2.24	9.06E-04	24	15.61	19.18	0.01	6.0	10.33	3.93	0.00			
				3.46	1.46E-03	14	20.66	28.06	0.00	1.7	10.28	3.88	0.00			
				4.49	2.85E-03	6	26.26	33.96	0.00	2.8	10.08	3.68	0.00			
									973 K Φ = 0.65 β = 0.09 μ = 0.26							
	P1263	6.41	14.82	0.10	1.16E-04	14	1.11	1.73	0.00	0.8	10.52	4.90	0.00	Shear Thickening	0.40	40 minutes + 7 minutes
				0.44	5.18E-04	11	6.32	9.89	0.01	0.9	10.93	5.30	0.00			
				1.11	9.28E-04	12	9.21	12.62	0.00	1.5	10.38	4.76	0.00			
				1.52	2.31E-03	3	41.41	64.80	0.14	0.6	10.84	5.22	0.00			
	P1491	16.47	14.83	0.14	5.13E-05	16	0.18	0.28	0.01	1.1	9.65	4.03	0.01	Shear Thickening ==>	1.36 and −0.80	4 hours +
				0.21	7.80E-05	18	0.65	1.01	0.01	1.0	10.10	4.47	0.00	Shear Thinning[d]		1 hour, 37 minutes
				0.31	1.04E-04	16	1.19	1.86	0.00	1.0	10.25	4.62	0.00			
				0.86	1.51E-04	61	6.93	10.81	0.01	1.0	10.86	5.23	0.00			
				0.96	1.16E-04	16	3.25	5.07	0.00	1.0	10.64	5.01	0.00			
				1.03	3.90E-05	31	3.19	3.75	0.00	57.8	10.98	5.35	0.00			
				1.09	4.29E-05	20	3.40	3.83	0.00	−8.8	10.94	5.32	0.00			
				1.21	3.05E-04	7	2.84	3.22	0.00	−10.9	10.03	4.40	0.00			
				1.24	2.84E-05	19	2.46	2.93	0.00	16.6	11.01	5.38	0.00			
				1.26	1.02E-05	22	2.43	2.86	0.00	97.8	11.44	5.81	0.00			
				1.26	4.80E-06	13	2.53	2.91	0.00	−19.8	11.77	6.15	0.00			
									1023 K Φ = 0.65 β = 0.09 μ = 0.26							
	P1267	6.69	14.87	0.08	1.09E-04	12	0.37	0.58	0.00	0.6	10.05	5.12	0.00	Shear Thinning	−0.72	48 minutes + 38 minutes
				0.55	5.20E-04	15	1.84	2.85	0.00	1.0	10.42	5.49	0.00			
				1.07	8.82E-04	10	2.56	3.46	0.00	1.6	9.82	4.89	0.00			
				1.91	1.26E-03	11	3.27	4.43	0.00	2.0	9.70	4.77	0.00			

[a]Relative viscosity is calculated from the effective viscosity according to [*Brückner and Deubener*, 1997]. Some experiments report longer durations (denoted by "+additional time") due to initial influence of metal jacket. Abbreviations: β = bubble volume fraction; Φ = crystal volume fraction; μ = melt volume fraction; l = sample length; $\varnothing$ = sample diameter; γ = maximum shear strain reached at corresponding strain rate; $\dot{\gamma}$ = bulk shear strain rate; t = time spent at a given strain rate; M = maximum internal torque reached at corresponding strain rate in a progressive strain rate stepping sequence (from low to high strain rate) or minimum internal torque reached at corresponding strain rate in a reverse strain rate stepping sequence (from high to low strain rate); τ = maximum shear stress reached at corresponding strain rate in a progressive strain rate stepping sequence (from low to high strain rate) or minimum shear stress reached at corresponding strain rate in a reverse strain rate stepping sequence (from high to low strain rate); σ = standard deviation; n = stress exponent; Log $\eta_{effective}$ = logarithm of effective shear viscosity of the three-phase magmas reached at corresponding strain rate; Log η_r = logarithm of relative viscosity of the 3-phase magmas. Both effective and relative viscosities are bulk parameters; $\Delta\eta_r$ = variation in relative viscosity during deformation (positive when magmas shear thicken; negative when magmas shear thin). Run# in italics = iron-jacketed assemblages; all others = copper-jacketed assemblages. Bold font = data affected by rheology of metal jacket (P1191, P1266 and P1353) and alumina rods of the assembly (P1352).

[b]Experiment performed at 250 MPa.

[c]Strain weakening due to cracking.

[d]Strain hardening inducing cracking.

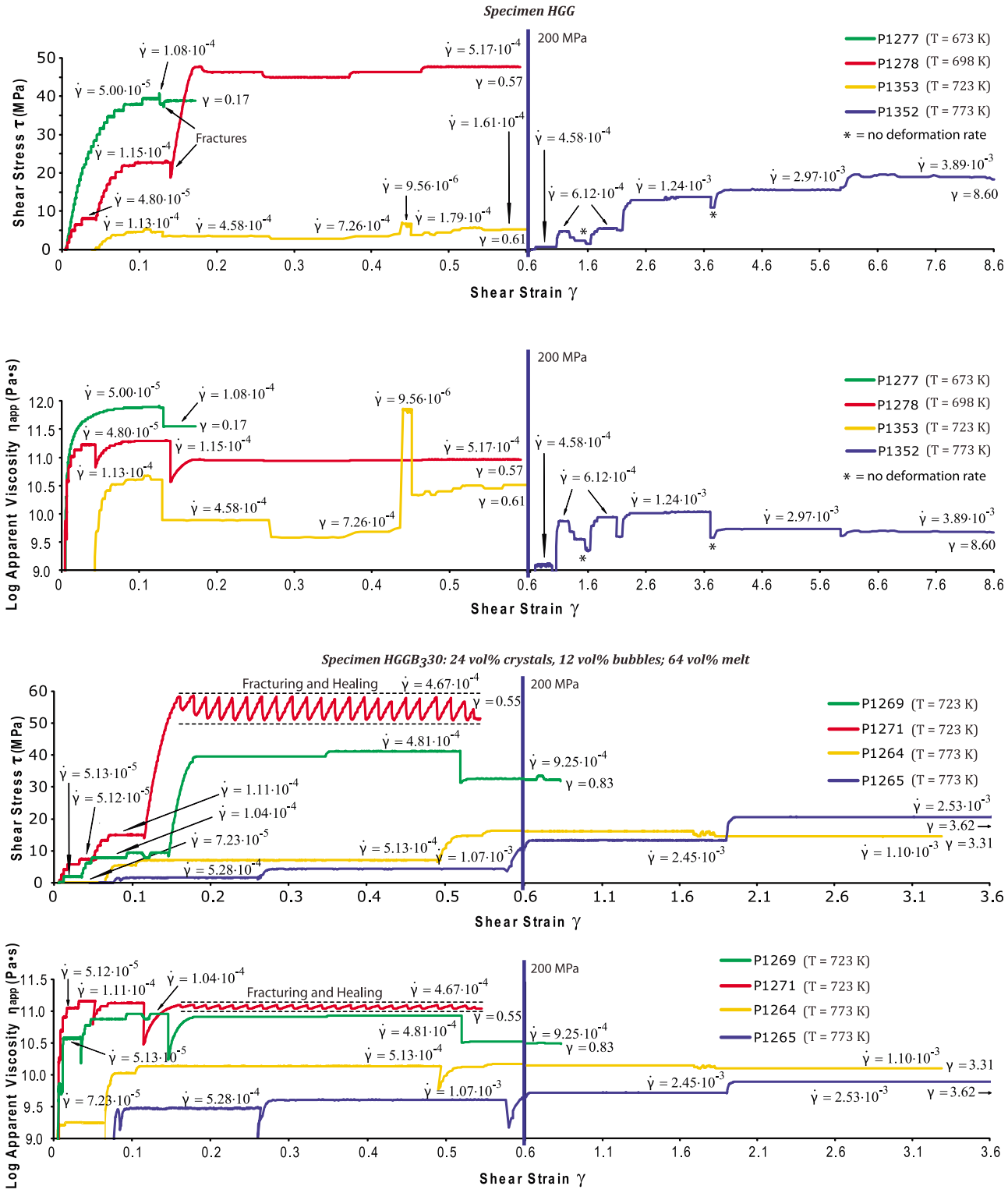

Figure 3. Shear stress (τ) versus shear strain (γ) and logarithm of apparent viscosity (η_{app}) versus shear strain (γ) diagrams (representative experiments): (a) HGG (pure glass); (b) $HGGB_3$-30 ($\mu = 0.64$, $\Phi = 0.24$; $\beta = 0.12$); (c) $HGGB_3$-50 ($\mu = 0.44$, $\Phi = 0.44$; $\beta = 0.12$); (d) $HGGB_3$-60 ($\mu = 0.35$, $\Phi = 0.55$; $\beta = 0.10$); (e) $HGGB_3$-70 ($\mu = 0.26$, $\Phi = 0.65$; $\beta = 0.09$). The diagrams comprise two strain windows: the left-hand one highlights lower strain rates in the range of 0–0.6 strain; the right-hand one displays higher strain rates exceeding 0.6 in strain. Abbreviations: γ = strain; $\dot{\gamma}$ = strain rate (expressed in s^{-1}). Further values of strain rate are reported in Table 3.

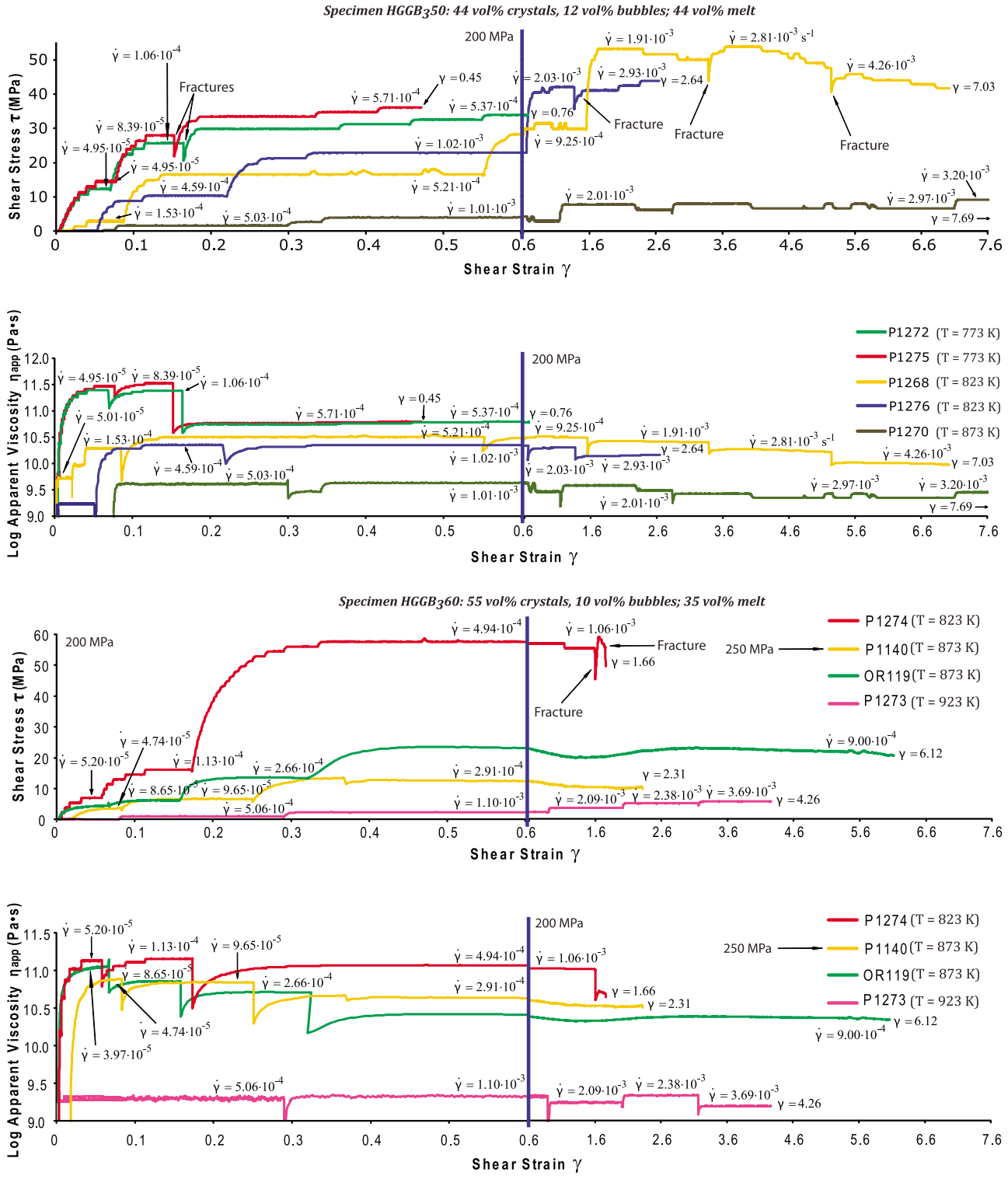

Figure 3. (continued)

viscosity [*Webb and Dingwell*, 1990b; *Brückner and Deubener*, 1997]. The Non-Newtonian onset was observed: at $1.08 \cdot 10^{-4}$ s^{-1} at 673 K; at $4.58 \cdot 10^{-4}$ s^{-1} to $5.17 \cdot 10^{-4}$ s^{-1} at 698–723 K; at $2.97 \cdot 10^{-3}$ s^{-1} at 773 K. At lower strain rates (<$5.00 \cdot 10^{-4}$ s^{-1}) HGG melt displays Newtonian behavior (Figure 3a). Following the approach of *Caricchi et al.* [2007], the influence of strain was tested in experiments P1352 and P1353 (Figure 3a). This test permitted evaluation of the reproducibility in peak stress that resulted within 0.85 MPa, which converts to a viscosity of 0.07 log units; we do not observe variation of viscosity with increase of applied strain (absence of thixotropic or

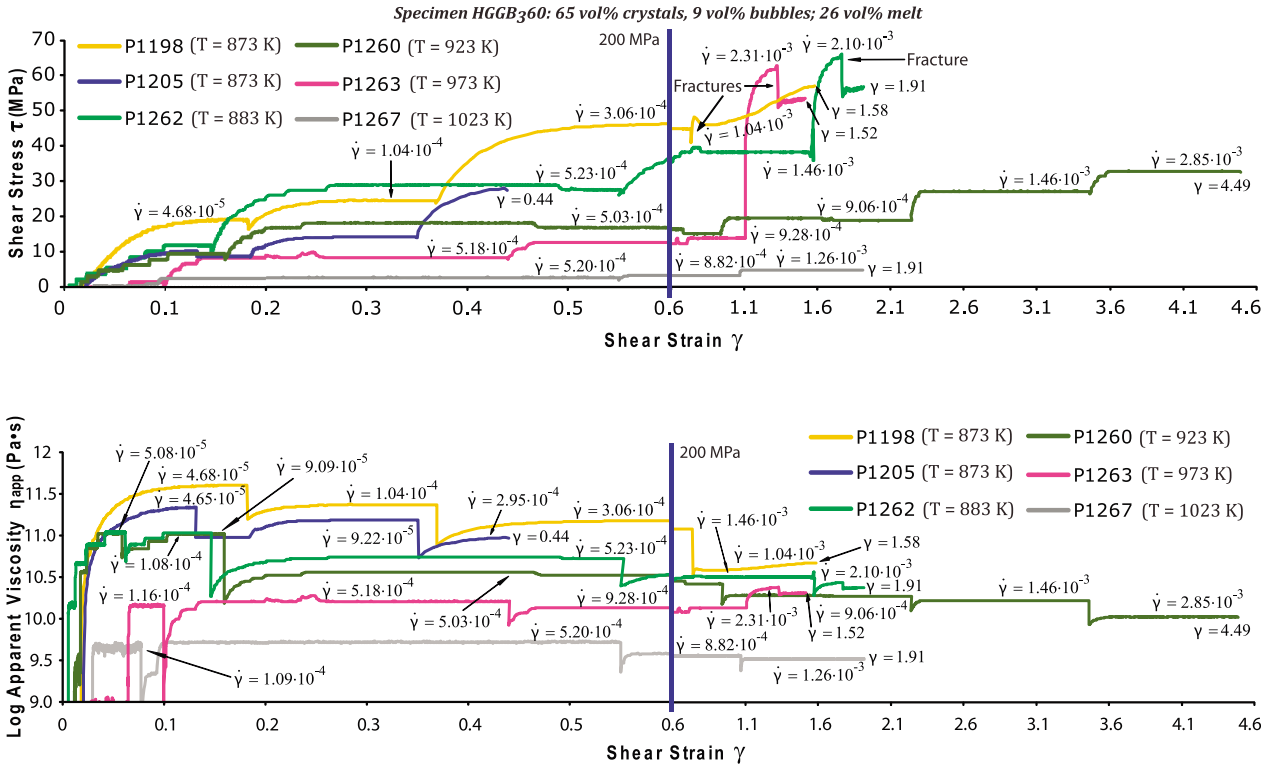

Figure 3. (continued)

rheopectic behavior [*Barnes*, 1997]). The Newtonian viscosities of these pure melt samples were subsequently used to determine the relative viscosity. We extrapolated the viscosity measurements obtained between 673 and 773 K to higher temperatures (823–1023 K) required for the crystal-bearing samples using a Vogel-Fulcher-Tammann type equation and the relative parameters from the model of *Giordano et al.* [2008] ($A = -6.55$; $B = 11185.2$ J; $C = 67.3$ K; A has been corrected according to our measured melt viscosities) (Figure 5).

4.2.2. $HGGB_3$-30: 12 vol.% Bubbles and 24 vol.% Crystals

[40] Five experiments were conducted at two different temperatures (723 and 773 K) on crystal-poor magmas. Experiments performed at identical temperature testify good reproducibility (with a maximum uncertainty in apparent viscosity of 0.80 log units; Figure 3b). The behavior of the sample is influenced by strain rate variation, except for run P1271 where the viscosity of the sample is invariant (decrease of effective viscosity of 0.06 Pa · s, the sample was affected by fracturing in the last strain rate step; Figure 3b). Other experiments reveal Non-Newtonian behavior. At 723 K (P1269) and relatively low strain rates ($5.13 \cdot 10^{-5}$ to $1.04 \cdot 10^{-4}$ s^{-1}), an increase of viscosity of 0.39 log units with increasing strain rate occurs (shear thickening [*Barnes*, 1989]). At higher strain rates ($4.81 \cdot 10^{-4}$ to $9.25 \cdot 10^{-4}$ s^{-1}) shear thinning predominates (effective viscosity decreases by 0.37 log units). At 773 K (P1264 and P1265), shear thickening dominates. In run P1264 a considerable increase of viscosity (0.72 log units) occurs between $7.23 \cdot 10^{-5}$ and $5.13 \cdot 10^{-4}$ s^{-1}, followed by a Newtonian plateau. In experiment P1265 the increase of viscosity with increasing strain rate (0.43 log units) is observable over the entire range of applied strain rates ($5.28 \cdot 10^{-4}$ to $2.53 \cdot 10^{-3}$ s^{-1}). No variation of viscosity with increasing strain was recorded during the experiments (Figure 3b). Run P1271 (723 K) displays brittle response at $4.67 \cdot 10^{-4}$ s^{-1} and the peak value of stress is used to calculate the effective viscosity. The stress evolution with strain suggests a continuous fracturing and healing process, which terminates with the total failure of the sample (Figure 3b). The influence of strain at low crystallinity was tested in experiment P1493 (Table 3 and Figure 4b). We do not observe any evident variation of the viscosity with increasing applied strain; for instance, the same strain rate was applied at different values of strain (see: $3.00 \cdot 10^{-4}$ s^{-1} applied at 0.81, 1.17 and 2.20 in strain; or $5.00 \cdot 10^{-4}$ s^{-1} applied at 2.51, 2.98 and 3.72 in strain; Table 3) and the viscosity did not vary by more than 0.25 log units (Figure 4b). In contrast, the viscosity is strongly related to the change in deformation rate. A summary of the viscosity variations as function of strain rate in sample $HGGB_3$-30 is displayed in Figure 4b and reported in Table 3.

4.2.3. $HGGB_3$-50: 12 vol.% Bubbles and 44 vol.% Crystals

[41] Six experiments were performed at three different temperatures (773, 823 and 873 K) on magmas with moderate crystallinity and strain rates ranging between $4.95 \cdot 10^{-5}$ s^{-1} and $4.26 \cdot 10^{-3}$ s^{-1} (run P1266 is not displayed in Figure 3c; all runs are listed in Table 3). Variation of viscosity with increasing strain rate occurs in all runs (Figures 3c and 4c). At 773 K (P1272 and P1275), an initial Newtonian regime at low strain rates ($4.95 \cdot 10^{-5}$ to $8.39 \cdot 10^{-5}$ s^{-1}) is followed by decreasing viscosity at higher strain rates ($8.39 \cdot 10^{-5}$ s^{-1} to $5.37 \cdot 10^{-4}$ s^{-1}). In contrast, at

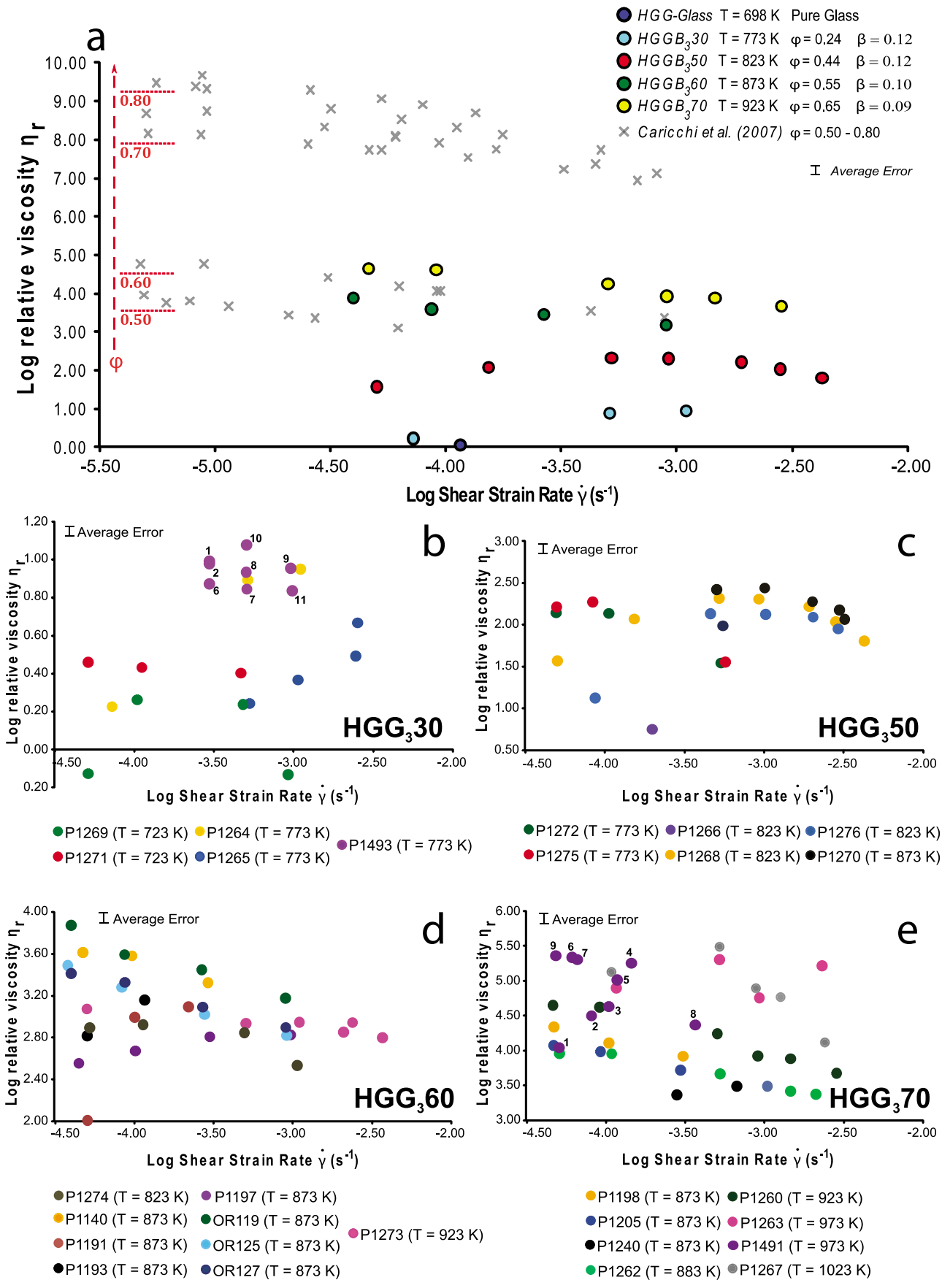
a
HGG-Glass T = 698 K Pure Glass
HGGB3 30 T = 773 K φ = 0.24 β = 0.12
HGGB3 50 T = 823 K φ = 0.44 β = 0.12
HGGB3 60 T = 873 K φ = 0.55 β = 0.10
HGGB3 70 T = 923 K φ = 0.65 β = 0.09
Caricchi et al. (2007) φ = 0.50 - 0.80
Average Error
0.80
0.70
0.60
0.50
φ
Log relative viscosity ηr
Log Shear Strain Rate γ̇ (s-1)
b
HGG3 30
c
HGG3 50
d
HGG3 60
e
HGG3 70
P1269 (T = 723 K)
P1264 (T = 773 K)
P1493 (T = 773 K)
P1271 (T = 723 K)
P1265 (T = 773 K)
P1272 (T = 773 K)
P1266 (T = 823 K)
P1276 (T = 823 K)
P1275 (T = 773 K)
P1268 (T = 823 K)
P1270 (T = 873 K)
P1274 (T = 823 K)
P1197 (T = 873 K)
P1140 (T = 873 K)
OR119 (T = 873 K)
P1191 (T = 873 K)
OR125 (T = 873 K)
P1273 (T = 923 K)
P1193 (T = 873 K)
OR127 (T = 873 K)
P1198 (T = 873 K)
P1260 (T = 923 K)
P1205 (T = 873 K)
P1263 (T = 973 K)
P1240 (T = 873 K)
P1491 (T = 973 K)
P1262 (T = 883 K)
P1267 (T = 1023 K)

Figure 4

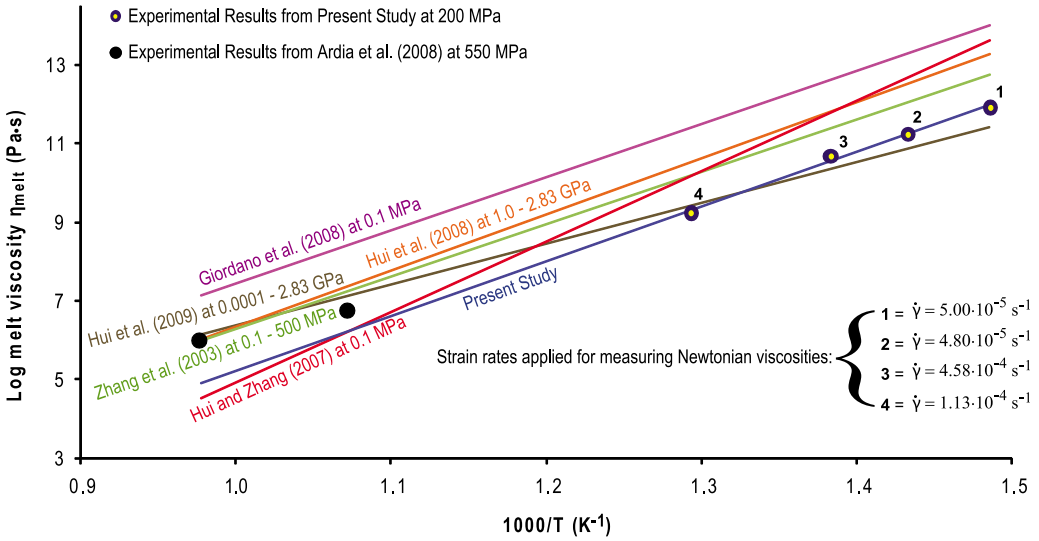

Figure 5. Logarithm of melt viscosity (η_{melt}) versus reciprocal temperature (1000/T). Viscosity measurements (at lowest applied strain rates; Table 3) were conducted in the reciprocal temperature interval 1.3–1.5 K^{-1} (673–773 K). Evident discrepancies exist between the viscosity trend obtained in this study and the various viscosity models displayed as lines: 2 orders of magnitude lower than viscosities estimated by *Giordano et al.* [2008]; 1–1.5 orders of magnitude lower than viscosities predicted by *Zhang et al.* [2003] and *Hui et al.* [2008]. The *Hui and Zhang* [2007] and *Hui et al.* [2009] models infer a different slope. For reference, experimental results obtained on the same haplogranitic composition at 550 MPa from *Ardia et al.* [2008] are included. Abbreviations: $\dot{\gamma}$ = bulk shear strain rate.

823 K (P1268 and P1276) increasing viscosity with increasing deformation rate is recorded (0.74 log units) at low strain rates followed by a Newtonian plateau at moderate deformation rates ($4.59 \cdot 10^{-4}$ to $1.02 \cdot 10^{-3}$ s^{-1}), switching to decreasing viscosity with increasing shear rate (0.51 log units) at higher strain rates ($1.91 \cdot 10^{-3}$ to $4.26 \cdot 10^{-3}$ s^{-1}). In run P1268 (823 K), decreasing viscosity with increasing strain (shear weakening) was recorded in the high strain rate range ($1.91 \cdot 10^{-3}$ to $4.26 \cdot 10^{-3}$ s^{-1}); this behavior is related to sample cracking (Figure 3c). At 873 K (P1270), shear thinning (viscosity decrease of 0.37 log units) is observed. Two replicate experiments performed at both 773 and 823 K testify good reproducibility (with a maximum uncertainty in apparent viscosity of 0.50 log units; Figure 3c). In all experiments (except run P1270 at 873 K) fracturing occurred and the brittle/ductile transition was encountered at comparable values of strain rate: from $1.00 \cdot 10^{-4}$ s^{-1} to $5.00 \cdot 10^{-4}$ s^{-1} at 773 K; from $2.00 \cdot 10^{-3}$ s^{-1} to $3.00 \cdot 10^{-3}$ s^{-1} at 823 K. At high temperature (873 K) no brittle behavior was detected in the investigated strain rate range. Viscosity variations as function of strain rate in sample HGGB$_3$-50 are displayed in Figure 4c.

4.2.4. HGGB$_3$-60: 10 vol.% Bubbles and 55 vol.% Crystals

[42] Nine experiments were performed at 823 to 923 K on 10 vol.% bubble- and 55 vol.% crystal-bearing samples (Table 3 and Figure 3d). Figure 3d displays selected typical experiments. Seven replicate experiments were conducted at 873 K to test reproducibility and sample homogeneity. Differences occur under identical conditions as exemplified by runs P1197 and OR119 that reveal a discrepancy of almost one order of magnitude in viscosity at a strain rate of $1.00 \cdot 10^{-4}$ s^{-1}. This difference is most probably associated to some heterogeneity of the samples used in the experiments. In contrast, two runs performed at different pressures, (OR119 and P1140), do not display any discrepancy in apparent viscosity (within an uncertainty of 0.02 log units; Figure 3d) at $1.00 \cdot 10^{-4}$ s^{-1}. A decrease of apparent viscosity with increasing deformation rate (shear thinning) occurred in all experiments at all temperatures (Figures 3d and 4d): at 823 K (P1274) viscosity decreased by 0.39 log units; at 873 K by as much as 0.69 log units; at 923 K (P1273) by 0.27 log units. Runs P1140 and OR119 reveal a variation of apparent viscosity with increasing strain (shear weakening) in the last strain rate step. Transition to brittle behavior, evidenced by sharp drops of applied stress, was observed in experiment P1274 at 823 K and strain rate of $1.06 \cdot 10^{-3}$ s^{-1} followed by short stress recovery, probably associated with fracture healing. The changes of viscosity with changing strain rates in sample HGGB$_3$-60 are displayed in Figure 4d.

Figure 4. Logarithm of relative viscosity (η_r) as a function of shear strain rate ($\dot{\gamma}$) for: (a) summary of the principal results from representative runs; (b) HGGB$_3$-30 ($\mu = 0.64$, $\Phi = 0.24$; $\beta = 0.12$); (c) HGGB$_3$-50 ($\mu = 0.44$, $\Phi = 0.44$; $\beta = 0.12$); (d) HGGB$_3$-60 ($\mu = 0.35$, $\Phi = 0.55$; $\beta = 0.10$); (e) HGGB$_3$-70 ($\mu = 0.26$, $\Phi = 0.65$; $\beta = 0.09$). The results are compared with ones from the study of *Caricchi et al.* [2007] (crystal-bearing magmas in the same chemical system). Runs P1491 and P1493 were not performed with simple progressive strain rate stepping; numbers identify the sequence of applied strain rates; some data points of these 2 runs fall outside the diagrams. Abbreviations: μ = melt volume fraction; Φ = crystal volume fraction; β = bubble volume fraction.

4.2.5. $HGGB_3$-70: 9 vol.% Bubbles and 65 vol.% Crystals

[43] The higher crystallinity (i.e., strength) of these samples allowed performing experiments at higher temperatures (873–1023 K; Table 3) because the applied stresses are significantly higher than the resistance to deformation of the metallic jacket. Figure 3e displays the results from selected typical experiments. Experiments were terminated between 1.30 and 2.00 in total strain, except for a couple of tests stopped at much lower strain (P1240 at 0.16 and P1205 at 0.44) and one run terminated at 4.49 total strain (P1260). All experiments displayed in Figure 3e are characterized by decreasing viscosity with increasing strain rate. Only experiment P1263 (973 K) is affected by increasing viscosity with increasing strain rate in two discrete strain rate steps. In run P1198 (873 K) strain hardening has been noticed in the last strain rate step. The transition to brittle behavior was observed at two different temperatures (at 883 and 973 K; runs P1262 and P1263) for a deformation rate of about $2 \cdot 10^{-3}$ s^{-1}. Differences in stress and, consequently, apparent viscosity of maximum 0.5 log units were observed between run P1240 and runs P1198 and P1205 at identical experimental conditions (at 873 K and 200 MPa), which is most probably associated with internal sample heterogeneities promoting variable patterns of textural evolution with increasing deformation. Shear thinning represents the dominant Non-Newtonian effect, marked by a viscosity decrease ranging between 0.35 (P1205) to 0.97 log units (P1260). The influence of strain on viscosity was tested in experiment P1491 (Table 3 and Figure 4e). We observe a clear increase of viscosity (by more than one order of magnitude) with increasing strain when a deformation rate of $1.51 \cdot 10^{-4}$ s^{-1} was applied (Table 3). This viscosity increase (1.29 log units) with increasing strain is related to accumulation of stress before the sample fractures. Continuing the same experiment after a break of 2 min without deformation revealed that the application of successive strain rates did not produce any observable strain effect on viscosity. Again, the most evident variation in viscosity is caused by changing the deformation rate during the experimental run (Figure 4e). The change of viscosity while changing strain rate in $HGGB_3$-70 is displayed in Figure 4e.

[44] Figure 4a summarizes the logarithmic values of relative viscosity for four representative samples (P1264, P1268, OR119, P1260) as function of strain rate. The viscosities measured in the presence of bubbles and crystals are much lower than those measured in samples containing only crystals and the viscosity difference between the two data sets increases with increasing crystal content [*Caricchi et al.*, 2007]. An additional difference is the shear thickening behavior observed in this study at relative low strain rates, which was never observed in bubble-free samples by *Caricchi et al.* [2007].

4.3. Temperature Dependence

[45] Deformation runs were performed to investigate the effect of temperature on the strength of specimens containing different crystal and bubble fractions. As anticipated, increasing temperature reduces the strength of the samples. At equivalent strain rate conditions, a 50 K temperature increase leads to the following decrease of viscosity: in pure HGG melt and in crystal-poor magmas (HGG_3-30) by 0.8–1.0 log units (at $1 \cdot 10^{-4}$ s^{-1} to $1 \cdot 10^{-3}$ s^{-1}); at higher crystallinity (HGG_3-50 and HGG_3-60) by 0.3–0.8 log units; at highest crystal content (HGG_3-70) by 0.3–0.5 log units. The minimum/eutectic temperature for the employed hydrous (2.52 wt.% H_2O) haplogranitic composition is 1053 K at 200 MPa [*Holtz et al.*, 2001; *Ardia et al.*, 2008]. Therefore, samples have been deformed under subsolidus conditions but at strain rate and temperature conditions at which the melt behaves as a Newtonian fluid (supercooled liquid) and does not exhibit any crystallization, maintaining the initial characteristics of the samples.

4.4. Microstructural Observations

[46] SEM and EPMA BSE images were acquired on tangential polished sections of the experimental samples, where the maximum simple shear deformation is best appreciated. Within such sections, geometrical boundaries must be considered close to the metal jacket and alumina spacers where deformation is strongly hampered; thus, bubbles are slightly elongated or totally undeformed and do not corroborate the effective deformation applied in the sample. This section describes the evolution of crystal and bubble size distributions (Figures 6 and 7) and the microstructural characteristics of various samples after deformation (Figures 8–11). High melt viscosity inhibits crystal settling or bubble ascent during experiments. Bubbles behave as strain markers and constitute a fundamental indicator to track melt flow in the multiphase magma.

4.4.1. Evolution of Crystal Size Distribution During Deformation

[47] The crystal size distributions (CSD) of deformed specimens were characterized and compared with the CSD of the starting material (Figure 6). An evident shift of CSDs is found in the samples with higher crystal fractions (ϕ = 0.44–0.65 vol.%) from a mean value of 55–60 μm in the undeformed sample ($HGGB_3$ series produced by HIP experiment) to 50 μm in the specimen containing 24 vol.% crystals down to 10 μm in specimens containing 44 and 65 vol.% crystals. Run product P1140 (55 vol.% crystals) displays a broad CSD comparable to the starting material but shifted to lower values (25–35 μm). An apparent relationship between CSDs and total applied shear strain is inferred by increasing shift of CSD peaks with increasing total bulk strain, except for run P1262 (Figure 6). All CSDs are positively skewed.

4.4.2. Evolution of Bubble Content in Sheared Magmas

[48] Analysis of bubble deformation fabrics was focused on the variations of bubble content during deformation. Comparing undeformed and sheared samples containing 24 and 44 vol.% crystals (Figure 6), we observed a decrease of bubble volume from 12 to 7–10 vol.% in crack-free areas of about 1 mm^2, except for run P1269, which maintained the initial bubble content (12 vol.%). Samples with higher crystallinity (55–65 vol.%) do not reveal any significant variation of bubble fraction (within an error of $\pm$0.2 vol.%) except run P1140 (55 vol.% crystals) displaying a small decrease of 1.0 ± 0.35 vol.%, possibly related to the higher applied confining pressure (250 MPa).

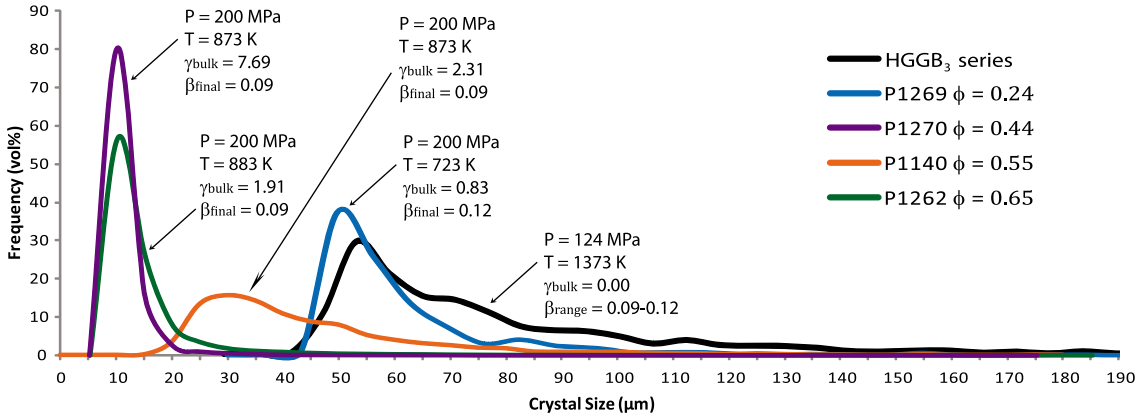

Figure 6. Crystal size distribution (CSD) for representative experimental samples (P1269, P1270, P1140 and P1262; Table 3) compared to the CSD of the starting material ($HGGB_3$ series; CSD investigated by 2D image analysis). Because of low aspect ratio (<3) crystal sizes are considered as the diameter of a solid spherical particle with an equivalent area. Abbreviations: γ_{bulk} = final bulk strain; Φ = crystal volume fraction; β_{range} = bubble volume fraction in the starting material $HGGB_3$; β_{final} = final bubble volume fraction after deformation.

4.4.3. BSD and BND in Sheared Magmas

[49] During high temperature and pressure static experiments, larger bubbles tend to shrink and the population of bubbles with 5–10 μm in diameter clearly increases (Figures 1b and 1c). In run product P1270_central a coarser population of bubbles (with a peak of BSD at 10–15 μm; Figure 1b) is noticed; in this sample, bubbles are slightly deformed and probable incipient coalescence occurred. The amount of bubbles present at high pressure and temperature does not change with temperature and/or duration of the experiment, compared to the starting material (Figure 1a).

[50] BSDs from tangential sections of experimental specimens were compared with the deformation-free inner, axial portions of the same samples and undeformed samples used in static tests (Figure 1b versus Figure 7; see also Table 2). BSDs from deformed crystal-poor magmas are more positively skewed, coarser (the maximum size peak of the distribution is shifted to higher values) and slightly broader ranging between 10 and 30 μm. At lower temperature (723 K) and low strain, bubbles do not exceed 75 μm whereas at higher temperature (773 K) and high strain deformed bubbles attain maximum sizes of 95 μm (P1265) and 115 μm (P1264). At higher crystallinity (44–55 vol.%) different BSDs (Figure 7b) are recorded. At 44 vol.% crystals (P1270) a coarser and broader BSD with a wide peak between 15 and 20 μm and a maximum equivalent diameter of 60 μm is observed. At crystallinity of 55 vol.% (P1140) the BSD is not different from the BSD observed in the undeformed portion of the same sample; the peak is shifted from 5 to 10 μm and a maximum equivalent bubble diameter of 30 μm as opposed to 35 μm in the undeformed portion is recorded. Following an approach similar to *Gardner* [2007], Figure 7c presents a diagram where the bubble number density (BND) is expressed as a function of effective viscosity for both the external (maximum strain; viscosity value from the last strain rate step of the run) and the inner axial portion of samples (zero strain; starting Newtonian viscosity measured at lowest strain rate of the run). All specimens at low crystallinity show similar BNDs around $4.0 \cdot 10^3$ mm^{-3}. In all cases, except for P1269, the deformed portion has lower BND than the inner axial sample core by an average of $4.0 \cdot 10^3$ mm^{-3}. Furthermore, BND increases with temperature and crystallinity (P1270 versus P1264, P1265, P1269) by $0.4 \cdot 10^4$ mm^{-3} (Table 4). Finally, at the highest crystallinity (and highest pressure in the case of P1140) BND is most elevated (about 1.5 order of magnitude higher than at lower crystallinity); a decrease of $1.4 \cdot 10^5$ mm^{-3} with decreasing viscosity is observed (Figure 7c).

4.4.4. Microstructures of $HGGB_3$-30: 12 vol.% Bubbles and 24 vol.% Crystals

[51] At low strain rate and low strain (Figure 8a, run P1269) bubbles show the same degree of deformation in different portions of the sample (at equivalent distance from sample axis) suggesting dominant homogeneous deformation, although deformation is lesser in bubble-poor bands. Figure 8a shows few bubbles appearing less deformed around crystals and trails of bubbles aligning along preferential directions (at approximately 50°; according to our reference frame: positive values counterclockwise; negative values clockwise; Figure 8a), but do not reveal any sign of coalescence. As outlined in section 4.2.2, fracturing occurred in this sample at low temperature (723 K) and cracks are highlighted in Figure 8a by red lines. The fractures are generally less than 100 μm in length and antithetically arranged at angles ranging from −50 to −80° (mean value of −60°), relative to the shear plane. Other visible major cracks are related to cooling. Shear cracks pass through solid crystals and gas bubbles and display a different shape with respect to bubbles not affected by fracturing (yellow inset box in Figure 8a). At relatively high strain rate and strain, bubble-poor portions develop in the samples (e.g., see yellow highlighted areas on the right image in Figure 8b) and evidence for bubble coalescence (purple ellipses in Figure 8b) can be observed (Figure 8b, P1264 and P1265). Bubbles are clearly stretched and assume an irregular shape with sharp terminations. Elongated bubbles exhibit long extension axes (maximum 100–150 μm). A crucial observation is the existence of bubble-poor regions characterized by the presence of small bubbles (maximum 10–15 μm long, Figure 8b) and lower local bubble density. There is not clear

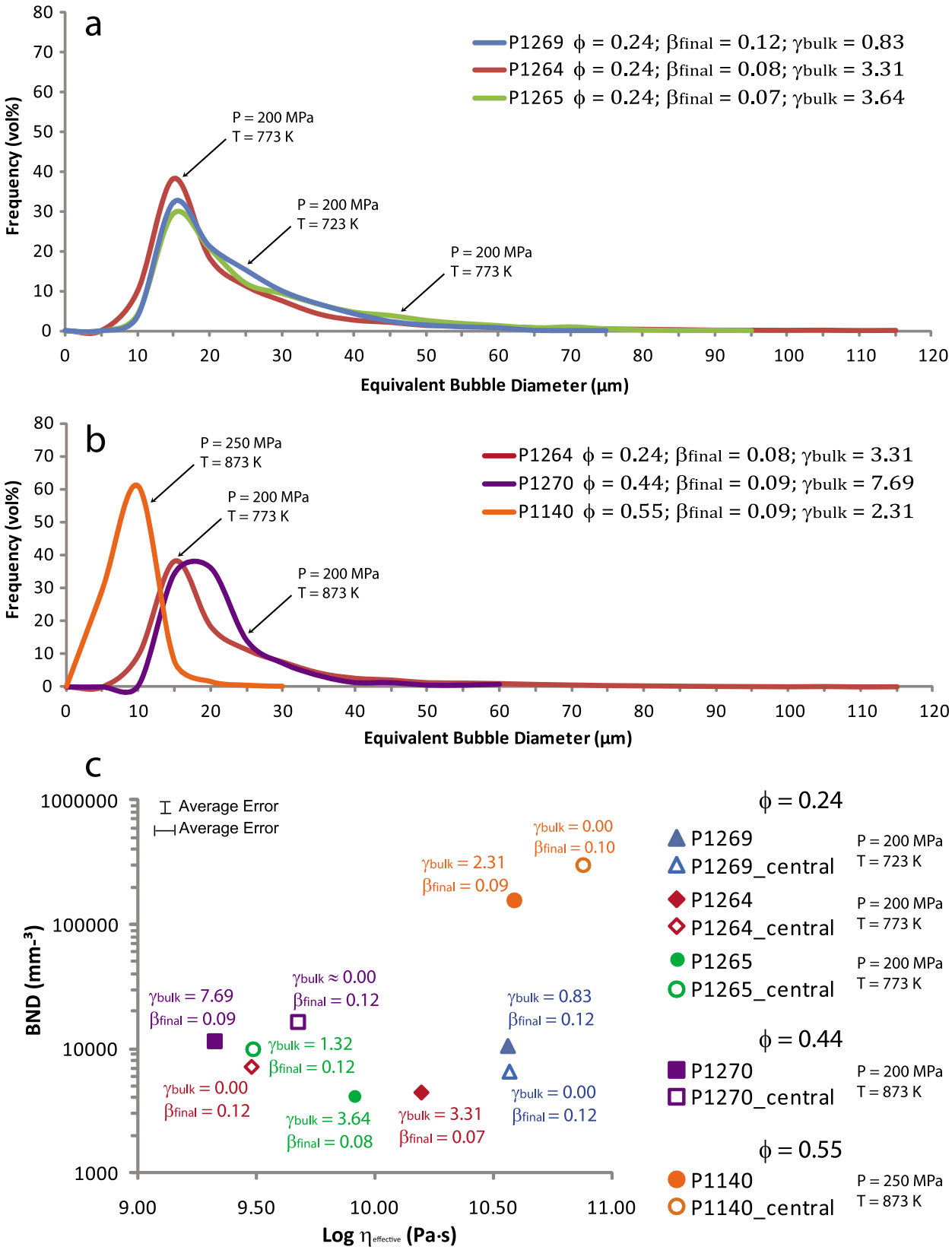

Figure 7. Bubble size distributions (BSDs) and bubble number density (BND) versus logarithm of effective viscosity ($\eta_{effective}$). BSD from: (a) deformation experiments of $HGGB_3$-30; (b) deformation experiments with variable crystal contents. (c) BND of deformed tangential sections compared to undeformed inner sample cores of the same specimens. Abbreviations: γ_{bulk} = final bulk strain; Φ = crystal volume fraction; β_{final} = final bubble volume fraction after deformation.

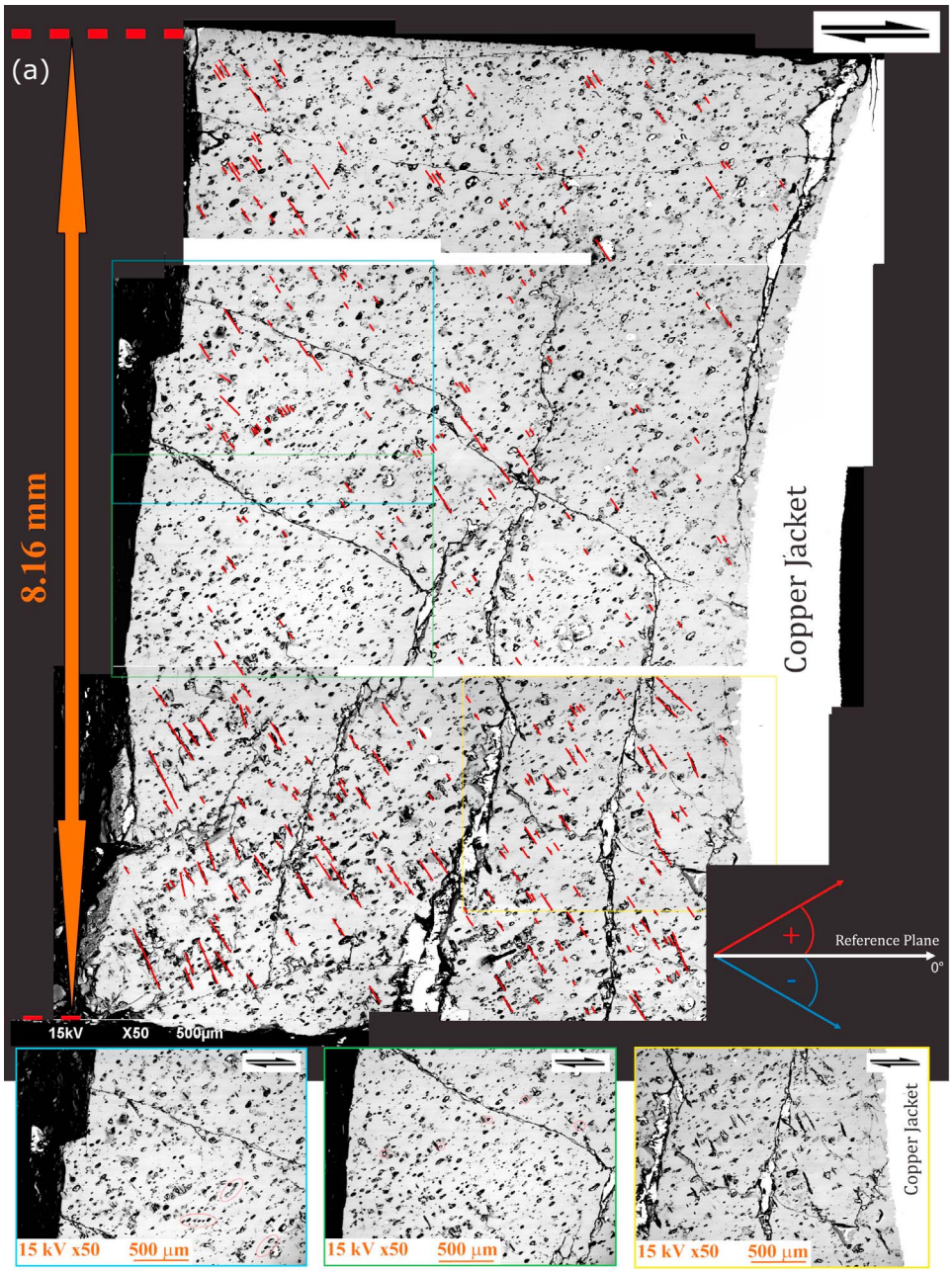

Figure 8. BSE images of crystal-poor magmas (tangential section of $HGGB_3$-30; $\mu = 0.64$, $\Phi = 0.24$; $\beta = 0.12$) deformed at different conditions of strain, strain rate and temperature: (a) P1269 ($\gamma = 0.83$; last $\dot{\gamma} = 9.25 \cdot 10^{-4}$ s^{-1}; T = 723 K); red lines indicate tracks of shear fracturing; red circles mark bubble alignments. (b) P1264 ($\gamma = 3.31$; last $\dot{\gamma} = 1.10 \cdot 10^{-3}$ s^{-1}; T = 773 K) on Figure 8b, left, and P1265 ($\gamma = 3.64$; last $\dot{\gamma} = 2.53 \cdot 10^{-3}$ s^{-1}; T = 773 K) on the Figure 8b, right. Purple ellipses highlight gas planes; yellow highlighted areas displays bubble-poor regions; green circle shows spherical (undeformed) bubble in proximity of solid quartz crystal.

distinction in crystal density between bubble-poor and bubble-rich portions in the same sample. In these portions the stretched bubbles display slightly lower angles (12–13°) with respect to the bubbles in the rest of the sample testifying a locally higher strain (e.g., in Figure 8b (right): $\gamma = 4.33$–4.70 instead of 3.64) demonstrating localization of deformation. Both images displays signs of shear fracturing occurred in the end of both experimental runs (e.g., in Figure 8b (left)).

4.4.5. Microstructures of $HGGB_3$-50: 12 vol.% Bubbles and 44 vol.% Crystals

[52] Intermediate crystallinity samples are characterized by inhomogeneous deformation (Figure 9). Crystal-poor bands are present and characterized by the presence of bubbles with their maximum axis orientated sub-parallel to the shear plane (Figure 9a, P1270), which suggests strain localization in these regions. Figure 9a (P1270) shows three principal sub-horizontal shear bands and a set of synthetic

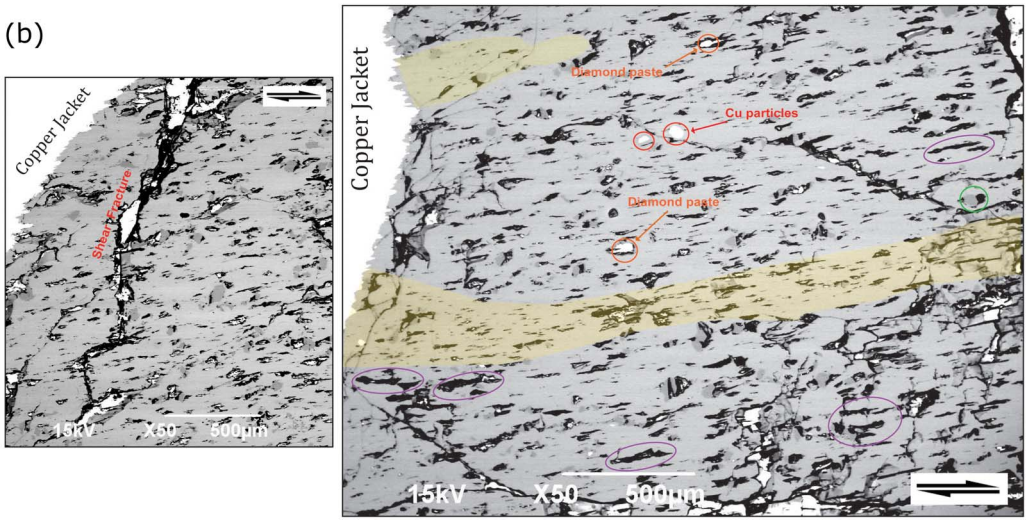

Figure 8. (continued)

and antithetic structures. These structures in the central shear band are oriented at average values of 12° and −11° respectively; below the same shear zone, they are oriented at 22 and −18° respectively. Shear bands of variable thickness are separated by crystal-rich layers (250–300 μm thick) ranging from about 5 mm length and 400 μm width (central one) to 2.5 mm length and 170 μm width (upper one) to 2 mm in length and 120 μm width (lower one). Structural trends were estimated based on the bubble orientations (see 4.4). In the crystal-poor shear localization zones, both synthetic and antithetic structures (composed by melt and bubbles) become less inclined to totally sub-horizontal. In contrast, in the crystal-rich portions higher angles (up to 65° and −39° respectively) are observed. The bar diagram in Figure 9a reveals a slight bimodal distribution of structure angles (much more evident for the synthetic structures: 0–15° and 20–40°) highlighting strain partitioning. Only locally the main axes of gas bubbles are orientated at 18–19°, close to the orientation given by the total applied strain (Table 3). Quartz crystals are arranged in layer-like structures that separate the shear zones from each other. In proximity of shear bands, quartz grains are smaller (about 2–30 μm) than inside the crystal-rich regions (about 30–135 μm) and are more frequently fractured. A bubble-rich layer is contained within the largest shear band that is interpreted as a gas channel generated by bubble coalescence during deformation. Figure 9b (sample P1268) displays a sample to which similar total strain and deformation rate were applied in the last strain rate step. This sample lacks the net distinction between sub-horizontal crystal-poor shear zones and crystal-rich regions. In addition, the shear bands appear to be less continuous than in P1270 (Figure 9a). Evidence for bubble coalescence is widespread; coalesced bubbles display different shapes ranging from thin channels to irregular inflated blobs surrounded by crystals (red rectangles in Figure 9b). In the wider shear bands bubbles develop sigmoidal shape and are considerably more stretched and locally affected by bubble ruptures and broken-off tips (blue inset in Figure 9b).

4.4.6. Microstructures of HGGB$_3$-60: 10 vol.% Bubbles and 55 vol.% Crystals

[53] The increase of crystal content appears to be associated with an increasing number density of crystal-poor shear bands. An anastomosing pattern of shear zones (melt-enriched planes) is established in the samples (Figure 10 depicts run P1140). Shear bands display limited sizes (about 100 μm long and 40–50 μm wide) with average angles of 4–15° (based on the elongation of the constituent deformed bubbles therein); occasionally synthetic shear zones at higher angle (up to 40°) occur. Antithetic bands (with average angles ranging between −2° and −18°) are less frequent. In Figure 10 the macroscopic (about 3 mm long and 180 μm wide) bubble- and melt-enriched region contains stretched bubbles with the maximum elongation axis orientated from 0° to 14°. Within shear bands, bubbles are highly stretched and both bubble coalescence and rupture can be observed (green contour in Figure 10). Bubbles located near crystal aggregates are relatively undeformed. Crystals of reduced size (3–50 μm) are present around the shear bands, but at increasing distance, clusters of quartz crystals preserve their original crystal size (63–125 μm) with only occasional fracturing that generates splintery forms (see light blue box in Figure 10). Using bubbles as strain markers, it is evident that silicate melt has rearranged at very high angles (up to 80° and −48° respectively) in the vicinity of particle clusters and at low angles (20°–30° and −2° respectively) where crystals are smaller in size and do not form local closest packing (Figure 10). A bimodal distribution of angles is found for synthetic structures (0–20° and 25–80°; Figure 10); this is less evident for antithetic ones.

4.4.7. Microstructures of HGGB$_3$-70: 9 vol.% Bubbles and 65 vol.% Crystals

[54] At high crystallinity (65 vol.%), shear localization bands are rather thin (about 110 μm thick in average; length up to about 500 μm) oriented at approximately 15°–20° to the shear plane and appear to be associated with a local decrease of the crystal size down to 1 μm or less (Figure 11a, run P1262). The stretching of bubbles increases in some

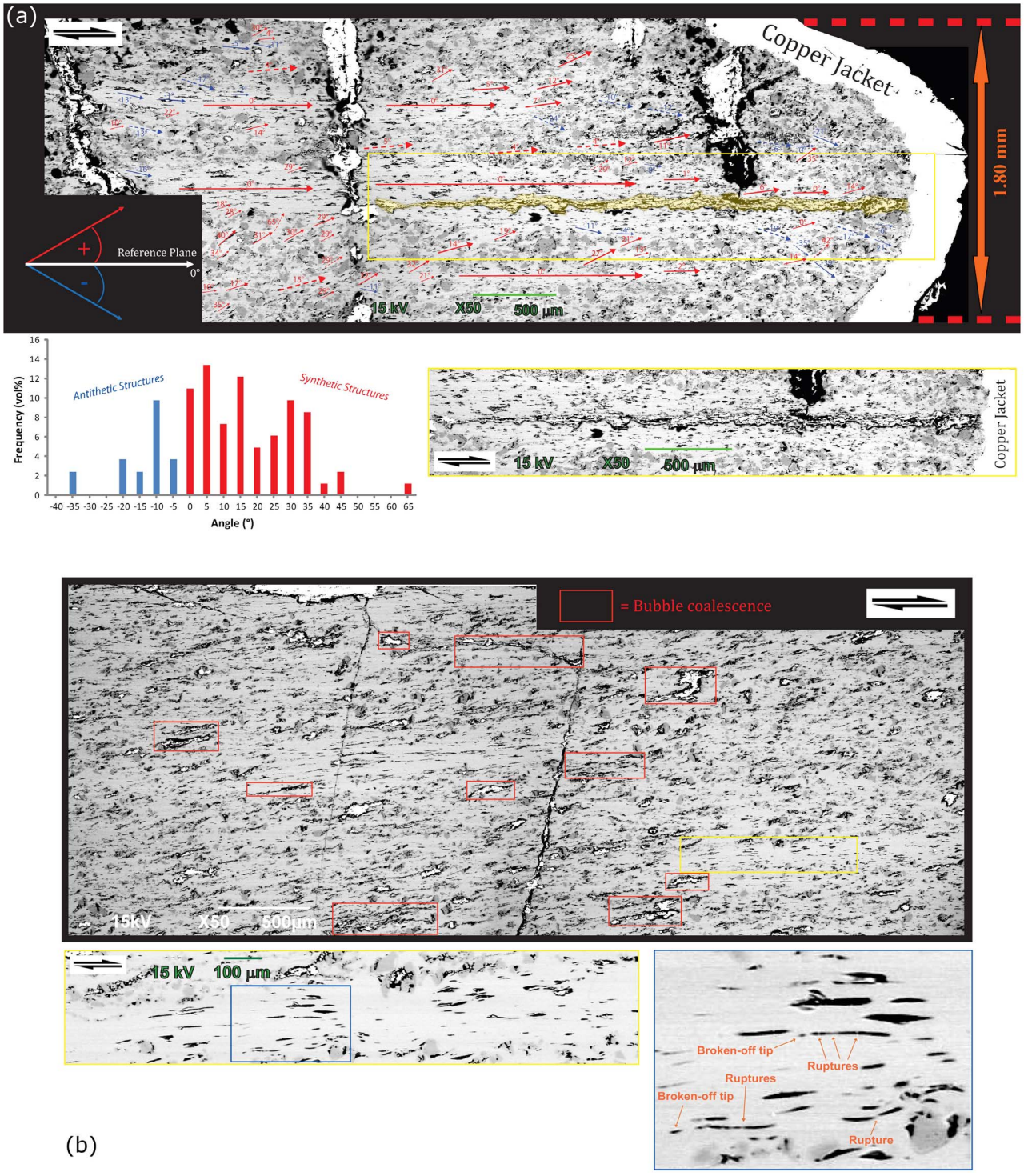

Figure 9. BSE images of magmas with intermediate crystallinity (tangential section of $HGGB_3$-50; μ = 0.44, Φ = 0.44; β = 0.12) deformed at different conditions of strain, strain rate and temperature: (a) P1270 (γ = 7.69; last $\dot{\gamma} = 3.20 \cdot 10^{-3}$ s^{-1}; T = 873 K); (b) P1268 (γ = 7.03; last $\dot{\gamma} = 4.26 \cdot 10^{-3}$ s^{-1}; T = 823 K). The angles of synthetic and antithetic structures are: positive counterclockwise (red arrows); negative clockwise (blue arrows). Continuous arrows are based on bubble elongation; dashed arrows are based on crystal alignment. Bar diagram at the bottom of Figure 9 shows distribution of (antithetic and synthetic) structure angles.

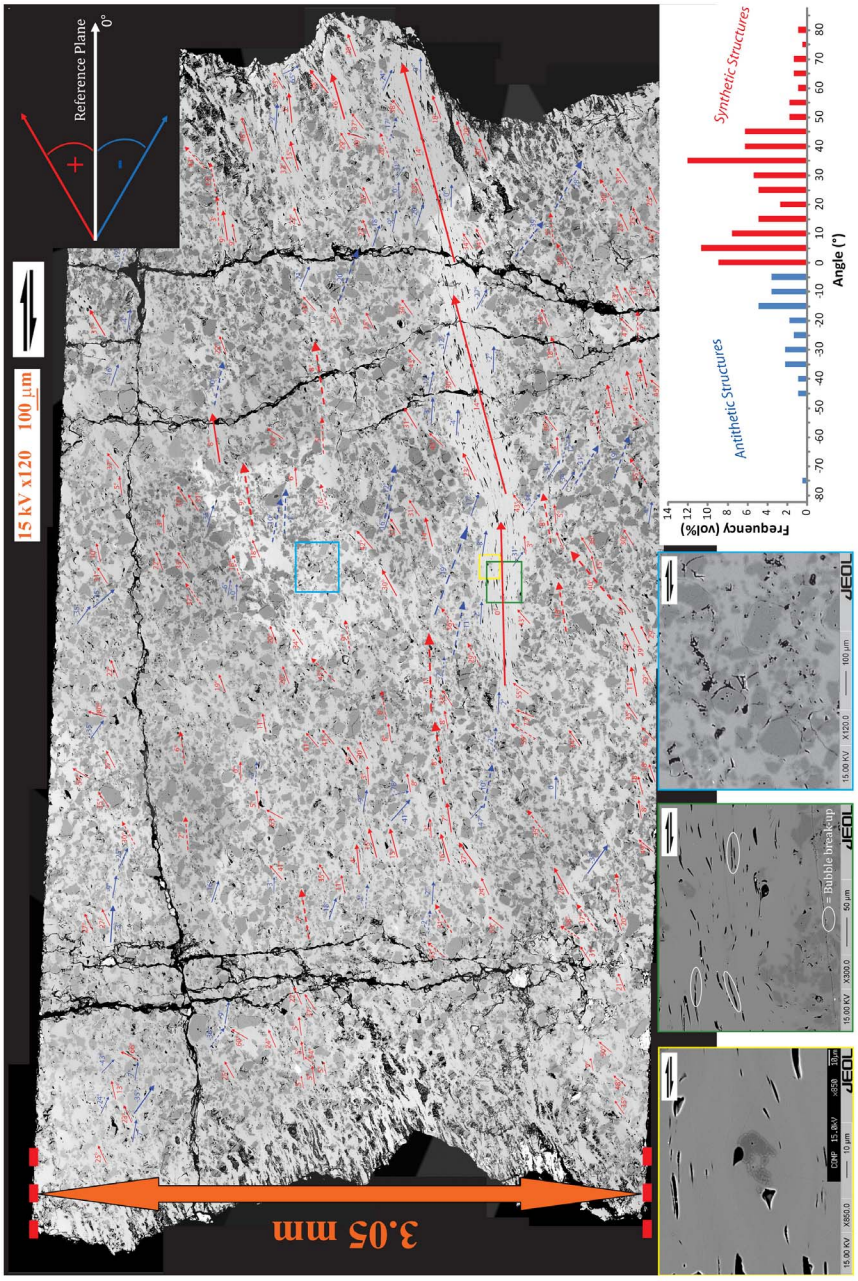

Figure 10. BSE images of crystal-rich magmas (tangential section of HGGB$_3$-60; $\mu = 0.35$, $\Phi = 0.55$; $\beta = 0.10$): P1140 ($\gamma = 2.31$; last $\dot{\gamma} = 2.91 \cdot 10^{-4}$ s^{-1}; T = 873 K; 250 MPa).

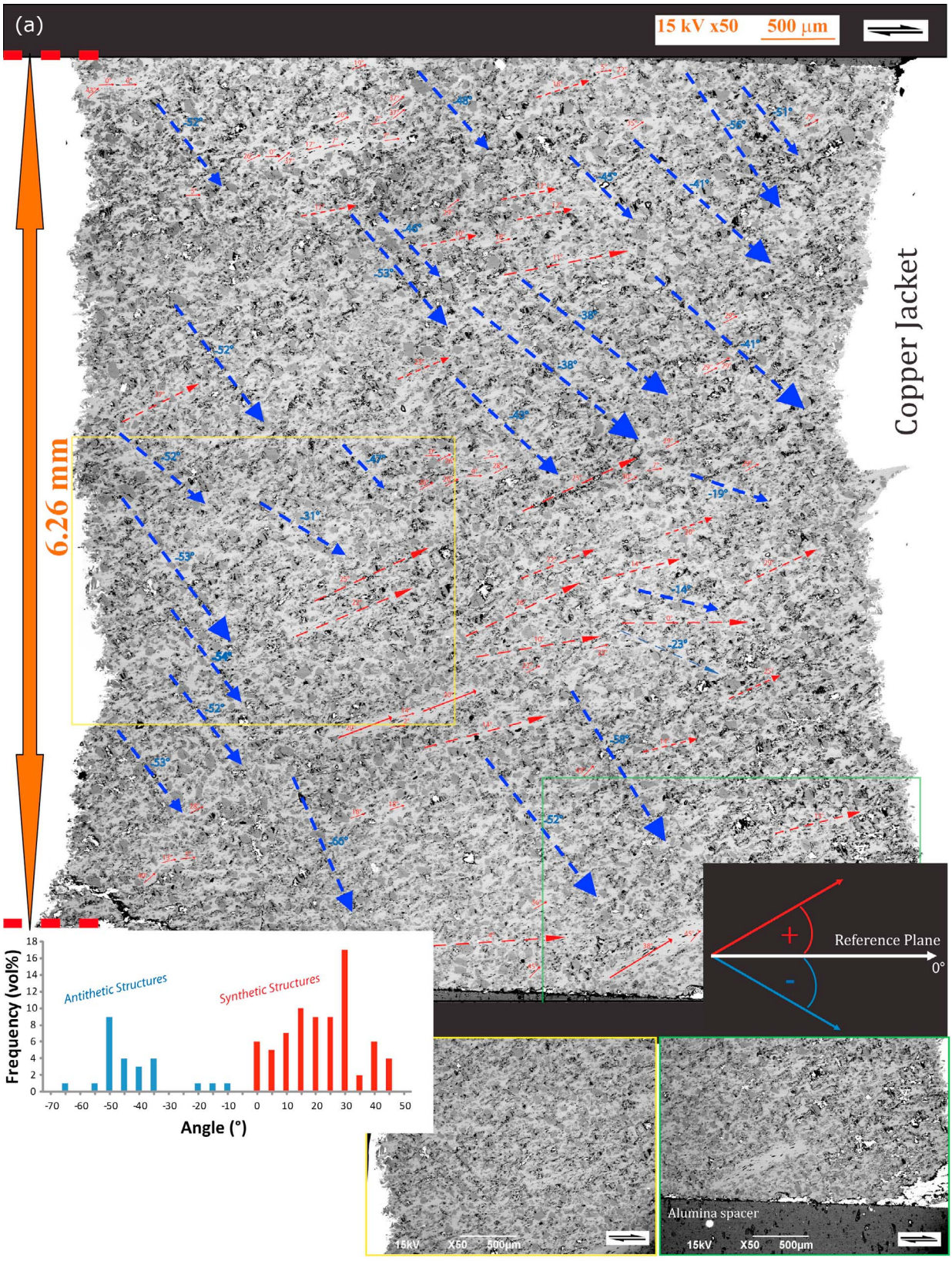

Figure 11. BSE images of crystal mushes (tangential section of $HGGB_3$-70; μ = 0.26, Φ = 0.65; β = 0.09) deformed at different conditions of strain, strain rate and temperature: (a) P1262 (γ = 1.91; last $\dot{\gamma} = 2.10 \cdot 10^{-3}$ s^{-1}; T = 883 K); (b) P1263 (γ = 1.52; last $\dot{\gamma} = 2.31 \cdot 10^{-3}$ s^{-1}; T = 973 K). The images at the bottom of Figure 11b have been taken with different electron beam spot size: low (62) spot size on the left image; high (74) spot size on the right image.

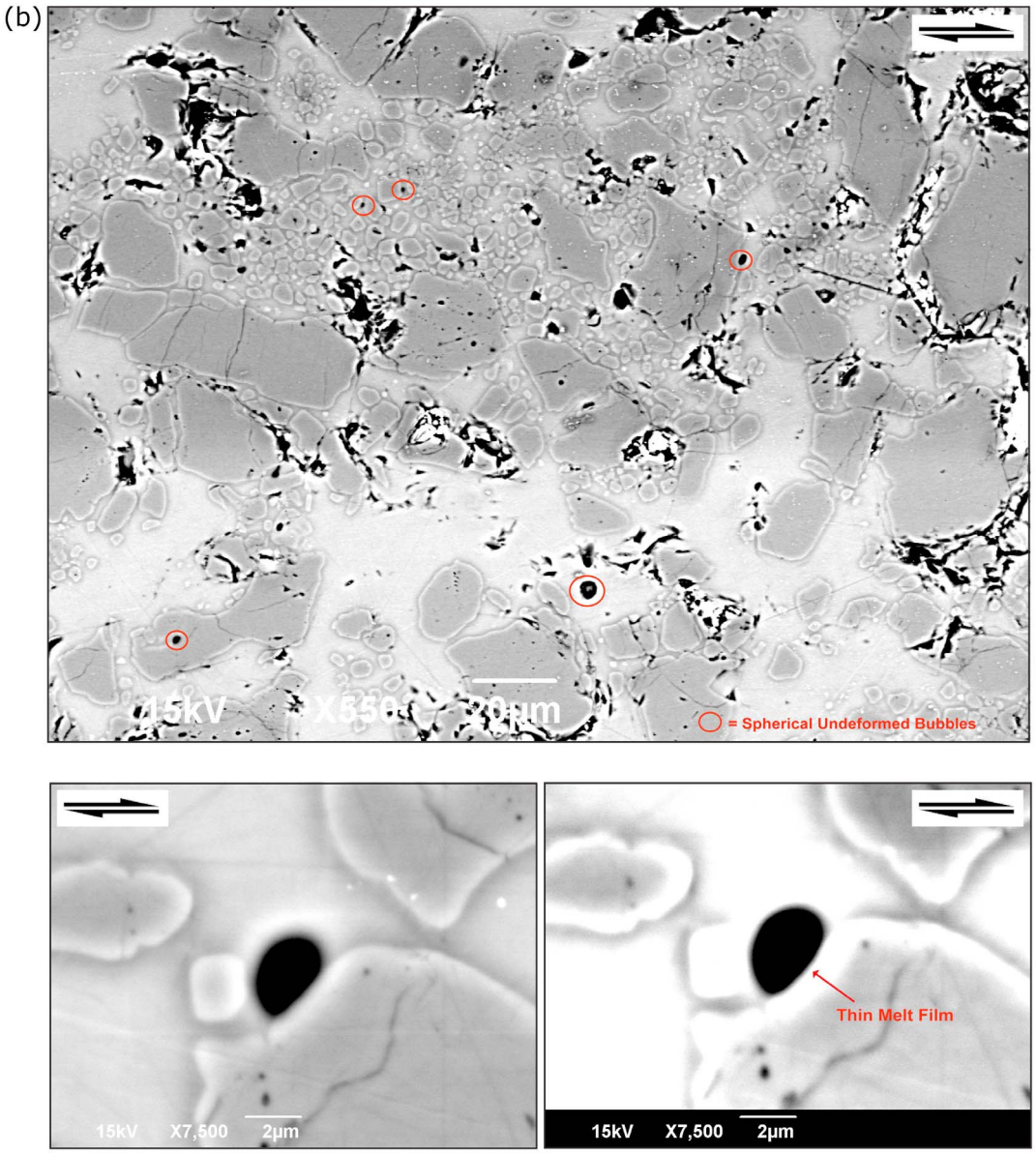

Figure 11. (continued)

regions, demonstrating strain localization (up to a shear strain of 5; compared to a bulk of 1.91). Bubbles are not homogeneously deformed within the same band owing to local strain patterns modified by the presence of crystals. Away from shear bands bubbles are undeformed. Bubble coalescence is not evident. Deformation produced strong alignments of quartz crystals at high angles (mean angle of $-50°$; blue arrows in Figure 11a). In proximity of crystal chains bubbles are spherical, suggesting absence of deformation. The observed antithetic and synthetic structures marked in Figure 11a generate two distinct dominantly unimodal distributions with peak values of $-50°$ and $30°$ respectively (inset in Figure 11). Figure 11b (run P1263) displays the intense concentration of crystals (formation of solid crystal clusters), partly affected by intense brittle fragmentation producing clusters with jigsaw-fit texture of quartz crystals (minimum average crystal size of 2 μm; Figure 11b, top) coexisting with spherical (or almost spherical) undeformed bubbles (Figure 11b, bottom). Bubbles are never in direct contact with solid crystals; but there is always a thin film of melt separating single bubbles from the quartz crystals (Figure 11b, bottom right). This sample is devoid of strain localization (i.e., absence of shear bands).

4.5. Summary of Rheological Observations

[55] Here, we summarize the observed effects of crystals and bubbles on bulk rheology and discuss parameters that potentially control the physical behavior of three-phase mixtures.

4.5.1. Effect of Crystals

[56] The increase of the suspended solid fraction produces an increase of relative viscosity (Figure 12), defined as the

Table 4. Summary of Representative Bubble Number Densities (BNDs) of Deformed Samples at 200 MPa and Various Temperatures and Strain Rates[a]

Sample	Total Number of Bubbles	Total Average Area of Analyzed Image (mm^2)	V_B (μm^3)	V_B (mm^3)	BND (mm^{-3})
P1269	2101	2.34	2.38E+07	2.38E-02	1.06E+04
P1269_central	872	7.41	1.59E+07	1.59E-02	6.60E+03
P1264	2822	2.34	4.43E+07	4.43E-02	5.10E+03
P1264_central	769	7.41	1.29E+07	1.29E-02	7.16E+03
P1265	3257	2.34	6.28E+07	6.28E-02	3.63E+03
P1265_central	967	7.41	1.20E+07	1.20E-02	9.71E+03
P1270	378	2.20	2.96E+06	2.96E-03	1.15E+04
P1270_central	2706	7.41	2.14E+07	2.14E-02	1.52E+04
P1140	2172	5.40	1.25E+06	1.25E-03	1.57E+05
P1140_central	4818	2.66	1.60E+06	1.60E-03	3.01E+05

[a]Abbreviations: V_B = total volume of bubbles; BND = bubble number density.

ratio between measured bulk effective viscosity of the system (composed of crystals, bubbles and melt in different relative proportions) and the Newtonian viscosity of the suspending melt phase at the same temperature. The results collected in this study are compared with a selection of experiments from *Caricchi et al.* [2007] performed in absence of gas bubbles and covering almost identical strain rates and crystallinities. At about 70 vol.% crystals, the addition of 9 vol.% bubbles results in a decrease of relative viscosity of about 4 orders of magnitude (compare $\phi = 0.70$, $\beta = 0.00$ from *Caricchi et al.* [2007] with $\phi = 0.65$, $\beta = 0.09$ from this study; see Figure 12a). Figure 12b shows an evident variation in the rheological behavior of multiphase suspensions as function of crystal fraction from a selection of typical experiments (P1264, P1268, OR119 and P1260). For crystallinities lower than 0.44, the relative viscosity increases with increasing strain rate (shear thickening), while for higher crystallinity (ϕ = 0.55–0.65), an opposite trend is observed (shear thinning). The contrasting behavior is less pronounced at lower strain rates ($5 \cdot 10^{-5}$ s^{-1} to $5 \cdot 10^{-4}$ s^{-1}) but more evident at higher strain rates ($1 \cdot 10^{-3}$ s^{-1} to $3 \cdot 10^{-3}$ s^{-1}). At crystal fraction of 0.44 a transition between the two Non-Newtonian regimes (shear thickening and shear thinning) is found.

4.5.2. Effect of Bubbles

[57] A first order estimate of the effect of bubbles was attempted considering two end-member cases: i) bubbles behave as rigid objects (capillary number lower than 1; $Ca < 1$ [*Llewellin et al.*, 2002]), ii) bubbles are inviscid and deform (capillary number higher than 1; $Ca > 1$ [*Llewellin et al.*, 2002]). In the first case the bulk viscosity could be calculated considering bubbles as crystals [*Llewellin and Manga*, 2005], which would increase the bulk viscosity (B^+ = effective viscosity with rigid bubbles; Figure 12b). Figure 12a shows that this is not the case, since the data from this study have generally lower viscosities than those measured for bubble-free systems at the same conditions. Considering bubbles as inviscid deforming objects (B^- = effective viscosity with soft bubbles; Figure 12b [*Llewellin and Manga*, 2005]), the presence of 10 vol.% bubbles would only reduce the viscosity by less than 0.1 log unit [*Manga and Loewenberg*, 2001; *Caricchi et al.*, 2011], which definitely does not explain the difference between the *Caricchi et al.* [2007] data and our results for a crystallinity of about 70 vol.% (Figures 4a and 12a). Neither simplified model can describe the transition from shear thickening to shear thinning with increasing crystallinity. Additionally, microstructural observations display a more complicated heterogeneous scenario that cannot be captured with these simplified models.

[58] To account for the presence of bubbles in a more rigorous way, it is necessary to consider the flow conditions during deformation. The bubble relaxation time (λ), representing a measure of the timescale over which a bubble can respond to changes in its shear environment [*Pal*, 2003; *Llewellin et al.*, 2002]:

$$\lambda = k \frac{r \eta_{Newtonian}}{\Gamma} \quad (1)$$

Where k is a dimensionless constant, r is the bubble radius before deformation, $\eta_{Newtonian}$ is the Newtonian shear viscosity of the melt phase and Γ is the bubble-liquid interfacial tension. Since bubble contents considered in this study are low (9–12 vol.%), we assumed $k = 1$ corresponding to an infinitely dilute (bubble-) suspension [*Taylor*, 1934]. Table 5 displays the relaxation times of bubbles with different radii (from 5 to 50 μm; in the range of our sample material prior to deformation), using Newtonian shear viscosities (Figure 5) and surface tension values (Γ) for haplogranitic melt similar to that employed by *Bagdassarov et al.* [2000] (0.22–0.24 N/m; Table 5). These calculations reveal that our experiments were performed in two different flow regimes:

[59] - unsteady flows at low temperatures (673–823 K), where bubble relaxation time is much longer than the timescale of deformation ($\lambda \gg t_{deformation}$);

[60] - steady flows at the high temperatures (873–1023 K), where bubbles are in their equilibrium deformation state ($\lambda < t_{deformation}$).

[61] Samples deformed under unsteady flow conditions contain bubbles with irregular edges (e.g., Figure 8b) whereas specimens deformed in steady flow conditions display bubbles with ellipsoidal shapes (e.g., Figure 10). Synchrotron-based X-ray tomography (Figure 13) has been conducted to visualize the three-dimensional bubble shapes. This analysis confirms that the experiments performed in different flow regimes according to equation (1), produced bubbles that are oblate and prolate in unsteady and steady conditions respectively. We additionally notice that 823 K is the boundary dividing unsteady flow conditions at lower temperatures (dynamic capillary number, Cd, and capillary number, Ca, > 1 [*Llewellin et al.*, 2002]) from steady conditions at higher temperature (Cd and $Ca < 1$ [*Llewellin et al.*, 2002]). The calculations were performed for different bubble diameters, ranging from 5 to 50 μm.

5. Discussion

[62] Experimental deformation results and microstructural observations have to be combined to unravel the processes responsible for the complex rheological behavior of samples containing different relative proportions of crystals and bubbles. The microstructures generated during deformation

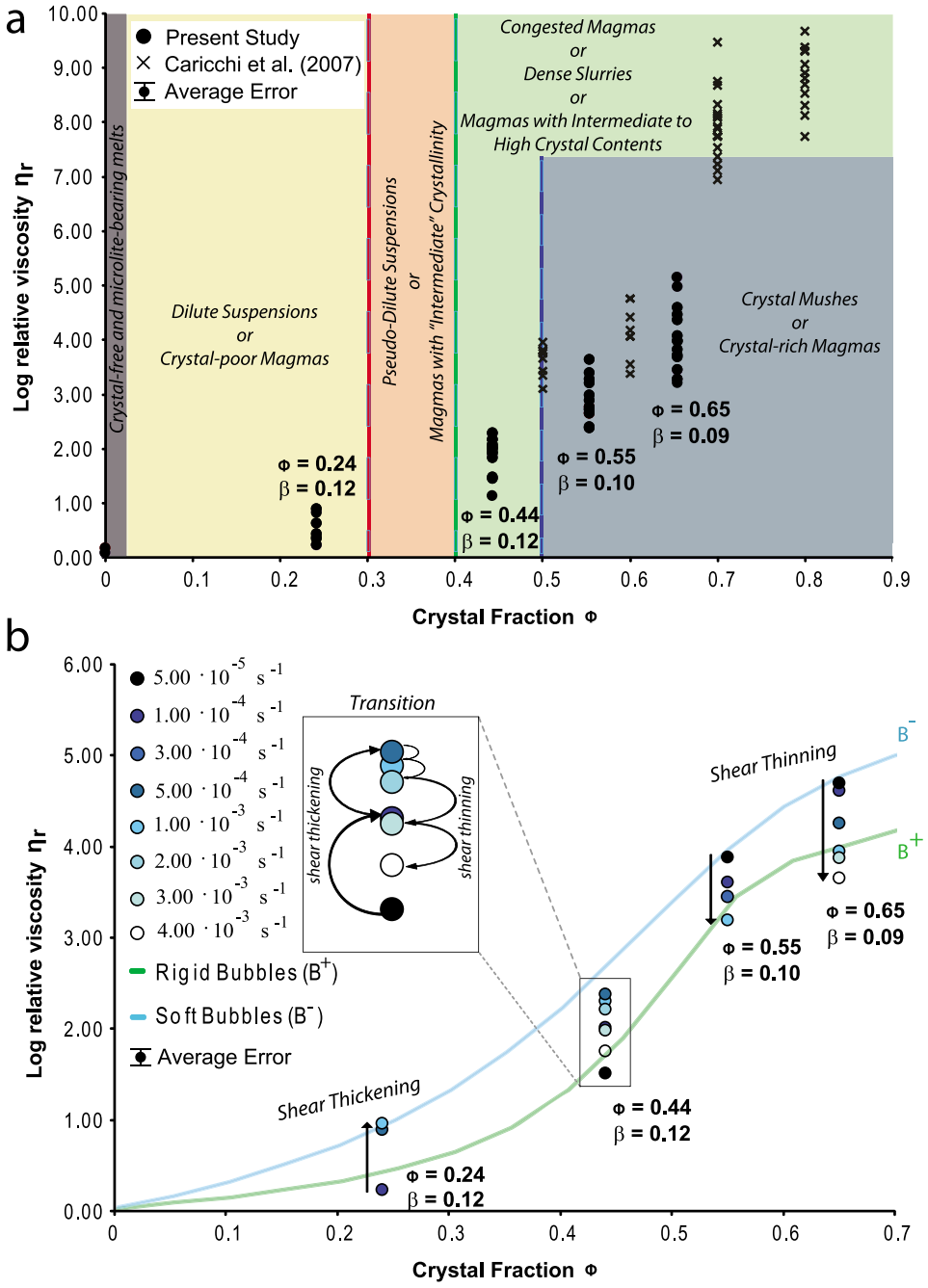

Figure 12. Logarithm of relative viscosity (η_r) as a function of solid fraction (ϕ): (a) comparison of the results of this study with the study of *Caricchi et al.* [2007] conducted in the same system (crystal-bearing haplogranitic magmas); diversely colored fields indicate different categories of magmas; (b) representative experiments exhibiting shear thickening at low crystal fraction ($\Phi = 0.24$), shear thinning at high crystallinity ($\Phi = 0.55$–0.65) and both effects at intermediate crystal contents ($\Phi = 0.44$); in addition, normalizations of the relative viscosity employing *rigid bubble rheology* (B^+) and *soft bubble rheology* (B^-) are shown (based on the work of *Llewellin and Manga* [2005] and references therein).

indicate heterogeneous deformation in the different samples investigated. Heterogeneous accommodation of strain is evidenced by the formation of melt-rich shear bands in crystal-rich magmas or by bubble coalescence in low crystal content-bearing magmas.

[63] Other authors highlighted the importance of viscous heating as fundamental contributor to the shear thinning behavior [*Holtzman et al.*, 2005; *Hess et al.*, 2008]. As already discussed for crystal-bearing magmas by *Caricchi et al.* [2007], viscous heating is unable to account for the magnitude of viscosity decrease that is observed in our experiments (Table 3). Therefore, shear thinning can be exclusively attributed to the presence and mutual interaction of quartz crystals and gas bubbles. At our experimental

Table 5. Bubble Relaxation Times at Different Temperatures Employed During Experiments[a]

	λ, Unsteady Conditions of Flow (hours)				λ, Transition (hours)	λ, Steady Conditions of Flow (hours)				
Bubble Radius (μm)	T(K) = 673, $\eta_{Newtonian}$ (Pa · s) = 8.12E+11, Γ (N/m) = 0.22	T(K) = 698, $\eta_{Newtonian}$ (Pa · s) = 1.67E+11, Γ (N/m) = 0.22	T(K) = 723, $\eta_{Newtonian}$ (Pa · s) = 4.72E+10, Γ (N/m) = 0.22	T(K) = 773, $\eta_{Newtonian}$ (Pa · s) = 1.69E+09, Γ (N/m) = 0.22	T(K) = 823, $\eta_{Newtonian}$ (Pa · s) = 1.61E+08, Γ (N/m) = 0.23	T(K) = 873, $\eta_{Newtonian}$ (Pa · s) = 1.74E+07, Γ (N/m) = 0.23	T(K) = 883, $\eta_{Newtonian}$ (Pa · s) = 1.15E+07, Γ (N/m) = 0.23	T(K) = 923, $\eta_{Newtonian}$ (Pa · s) = 2.39E+06, Γ (N/m) = 0.23	T(K) = 973, $\eta_{Newtonian}$ (Pa · s) = 4.03E+05, Γ (N/m) = 0.24	T(K) = 1023, $\eta_{Newtonian}$ (Pa · s) = 8.09E+04, Γ (N/m) = 0.24
2.50	2599.64	531.18	149.04	5.27	0.49	0.05	0.03	0.01	0.00	0.00
5.00	5199.29	1062.36	298.08	10.54	0.99	0.11	0.07	0.01	0.00	0.00
7.50	7798.93	1593.55	447.12	15.81	1.48	0.16	0.10	0.02	0.00	0.00
10.00	10398.58	2124.73	596.15	21.08	1.98	0.21	0.14	0.03	0.00	0.00
12.50	12998.22	2655.91	745.19	26.36	2.47	0.26	0.17	0.04	0.01	0.00
15.00	15597.87	3187.09	894.23	31.63	2.97	0.32	0.21	0.04	0.01	0.00
17.50	18197.51	3718.28	1043.27	36.90	3.46	0.37	0.24	0.05	0.01	0.00
20.00	20797.15	4249.46	1192.31	42.17	3.96	0.42	0.28	0.06	0.01	0.00
22.50	23396.80	4780.64	1341.35	47.44	4.45	0.47	0.31	0.06	0.01	0.00
25.00	25996.44	5311.82	1490.39	52.71	4.95	0.53	0.35	0.07	0.01	0.00
27.50	28596.09	5843.00	1639.42	57.98	5.44	0.58	0.38	0.08	0.01	0.00
30.00	31195.73	6374.19	1788.46	63.25	5.94	0.63	0.42	0.09	0.01	0.00
32.50	33795.37	6905.37	1937.50	68.53	6.43	0.69	0.45	0.09	0.02	0.00
35.00	36395.02	7436.55	2086.54	73.80	6.92	0.74	0.49	0.10	0.02	0.00
37.50	38994.66	7967.73	2235.58	79.07	7.42	0.79	0.52	0.11	0.02	0.00
40.00	41594.31	8498.92	2384.62	84.34	7.91	0.84	0.56	0.11	0.02	0.00
42.50	44193.95	9030.10	2533.66	89.61	8.41	0.90	0.59	0.12	0.02	0.00
45.00	46793.60	9561.28	2682.70	94.88	8.90	0.95	0.63	0.13	0.02	0.00
47.50	49393.24	10092.46	2831.73	100.15	9.40	1.00	0.66	0.14	0.02	0.00
50.00	51992.88	10623.64	2980.77	105.42	9.89	1.05	0.69	0.14	0.02	0.00

[a]Newtonian shear viscosities are taken from experimental measurements (Figure 5) and values of surface tension of haplogranitic melt are from *Bagdassarov et al.* [2000]. Abbreviations: $\eta_{Newtonian}$ = Newtonian shear viscosity of melt phase; Γ = surface tension; λ = bubble relaxation time.

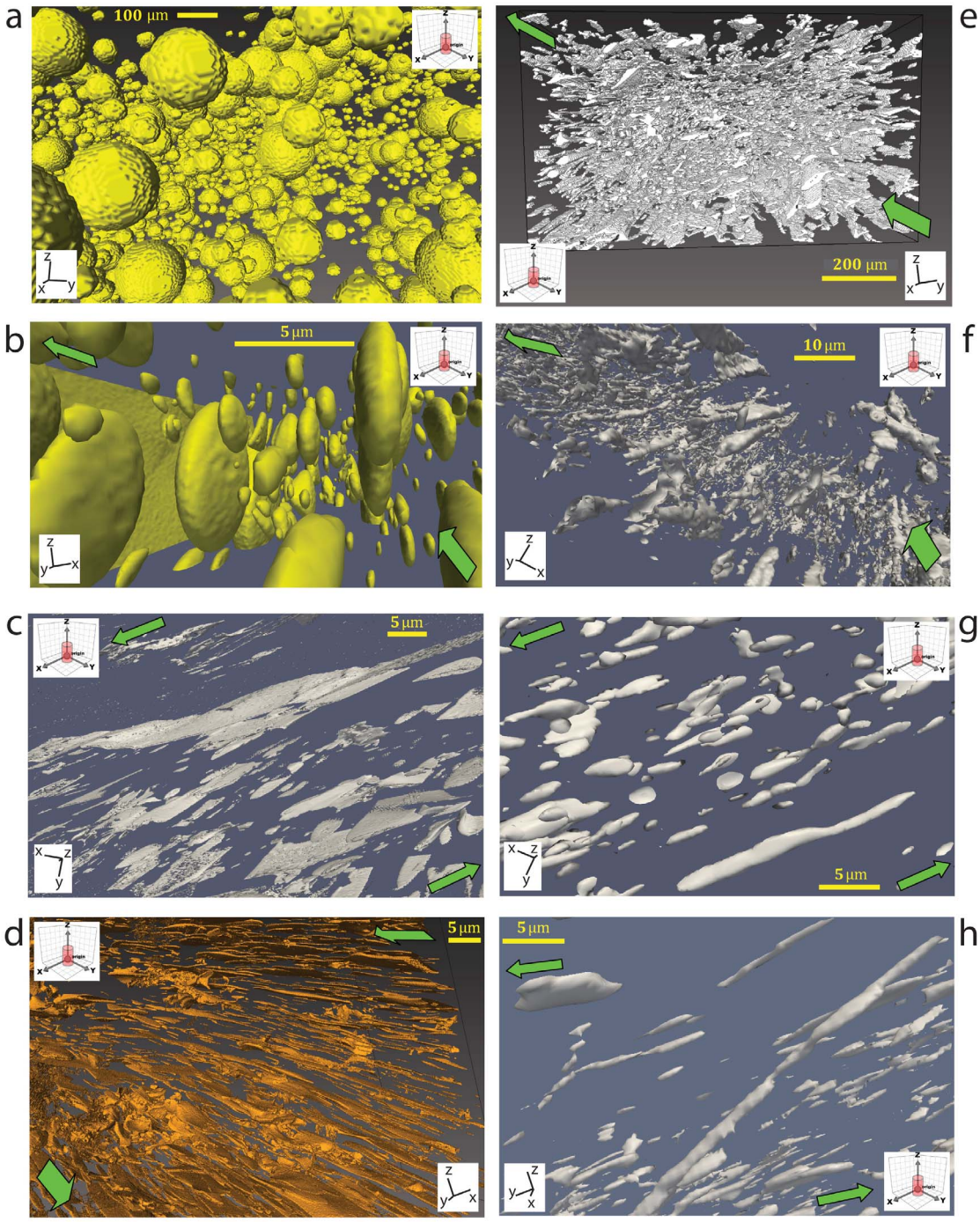

Figure 13. The 3D rendering of synchrotron-based X-ray tomographic microscopy data sets illustrating different bubble shapes: (a) starting material $HGGB_3$-30 displaying spherical bubbles; (b, c, d) unsteady flow regime with oblate bubbles (low strain with isolated gas bubbles in P1271 (Figure 13a) and high strain with extent of bubble coalescence in P1265 (Figures 13b and 13c); (e, f) transition from unsteady to steady flow conditions (high strain with dominant oblate bubbles affected by gas coalescence in P1270 (Figure 13e) and high strain with dominant prolate bubbles displaying signs of bubble break-up in P1268 (Figure 13f); (g and h) steady flow conditions with prolate bubbles (high strain with "bubble boudinage" (Figure 13g) and bubble break-up (Figure 13h) in OR119). The 3D rendering performed with both ParaView 3.8-RC1 (Figures 13b, 13c, 13f, and 13g) and Avizo® Fire (Figures 13a, 13d, and 13e).

conditions gravity forces are negligible suggesting that differential stress is responsible for the distribution of melt and crystals during deformation experiments [*Kohlstedt and Holtzman*, 2009].

[64] There is no wetting behavior of gas bubbles on quartz crystals [*Laporte*, 1994]. In fact, 2D images show the lack of any direct contact between bubbles and crystals, even when bubbles are very close to the quartz crystals (see Figure 11b, bottom). This is confirmed by experiments of *Hurwitz and Navon* [1994] showing that quartz crystals are inefficient nucleation sites for bubble nucleation and growth. *Laporte* [1994] examined the system quartz-(anorthite)-melt-vapor and reported that after five days at 1123 K, water bubbles were enclosed in melt and did not wet quartz crystals.

5.1. Dilute Magmatic Suspensions

5.1.1. Bubble Coalescence and Outgassing

[65] Crystal-poor magmas (24 vol.% crystals and initial 12 vol.% bubbles) exhibit shear thickening during deformation (Figures 3b, 4a and 12). Such a rheological behavior can be explained in terms of bubble coalescence and outgassing [*Gonnermann and Manga*, 2007; *Divoux et al.*, 2009]. Bubble-depleted portions are observed where bubble content is lower than in the starting material (7–8 vol.% from 12 vol.%; Figure 8b), BND decreases (Figure 7c) and the BSD broadens and coarsens (Figure 7a). These observations confirm that bubble coalescence and permeable loss of gas occurred during deformation. As already observed in *Caricchi et al.* [2011], gas escape occurs along the metal jacket. However, differently from the experimental set-up employed by *Caricchi et al.* [2011] using a central cylindrical electrode in the core of the sample where the gas was mostly escaping to the thermocouple hole (which is at 0.1 MPa and, thus, establishes an evident pressure gradient), in our experimental assembly the gas could escape only along the sleeve, and, more specifically, between the polycrystalline ceramic (displaying a slightly rough surface) and the metal jacket. The gas loss from the outer periphery of the sample (sample portion experiencing maximum deformation) is also confirmed by a comparison of image analysis data on bubble content and BND between portion of the samples located near the metallic jacket and in the core of the sample (Figure 7c). This analysis confirms the bubble depletion at the sample's margins. 3D renderings (Figures 13c–13d) of tomographic data sets reveal that bubbles are strongly stretched and flattened at high strain suggesting that bubbles were deformed under unsteady flow conditions, owing to low temperatures (723–773 K; i.e., high viscosity), as expected from equation (1). The planar deformation of bubbles increases the geometric possibility of coalescence, the generation of planar structures enriched in gas, which promotes the generation of gas channels and results in higher outgassing efficiency during deformation. In addition, bubble coalescence promotes strain localization [*Caricchi et al.*, 2011] as testified by the presence of bubble-depleted regions containing highly deformed bubbles (Figure 8b). Bubble coalescence is enhanced by the presence of bubbles of different sizes. *Lin and Lin* [2009] conducted experiments to evaluate in-line coalescence of two individual bubbles in a Non-Newtonian fluid and found that coalescence of two-unequal bubbles is more rapid than coalescence of two equal-sized bubbles. This suggests that the presence of coalesced bubbles (larger than the original bubbles) would promote the formation of gas channels/planes and creating a feedback mechanism. In such dilute suspensions, the lack of crystal breakage (Figure 8) suggests minor interaction between the particles, unable to impede the formation of gas-rich planes. The following question arises: Are bubble coalescence and outgassing related to increasing strain or strain rate? The results show that variations in rheological behavior are related to changes in strain rate, because no stress variations were observed with increasing strain (i.e., absence of shear weakening). This does not exclude that a certain amount of strain ($\gamma \geq 1.0$) is required to produce the microstructures observed after the experiments. For instance, runs P1264 and P1265 (Table 3 and Figure 3b) can be used to identify the dominating effect of strain rate over strain on producing shear thickening. These two experiments were performed at the same conditions, but they follow a different pattern of strain rate increase (Figure 3b and Table 3). The initial strain rate stepping in P1264 was performed at lower strain rates with respect to P1265. The results show that the strain required by the sample in P1264 to reach steady state flow (i.e., duration of the yielding stage) is larger than for P1265. The higher viscosity recorded for P1264 with respect to P1265 in the initial phases of deformation could be related to the more extended yielding stage in P1264 where bubble coalescence and outgassing is probably occurring. This marks the effective dependence of outgassing process on strain rate applied, since the same bubble loss observed in P1264 is achieved with higher strain rate (last $\dot{\gamma} = 2.53 \cdot 10^{-3}$ s^{-1}) in P1265 (Table 3 and Figure 3b). This dependence of bubble coalescence on strain rate at similar values of total strain has been observed in the experimental study of *Okumura et al.* [2006, 2008] where bubble coalescence is enhanced by increasing shear rate. Also in the decompression experiments of *Burgisser and Gardner* [2005] magma permeability is affected by bubble coalescence and, specifically, shear strongly catalyzes bubble interconnectivity in their open degassing setup (where the magma can volumetrically expand in the capsule headspace).

5.1.2. Application of the Concept of Critical Soil Mechanics to Magma Rheology

[66] The flow mechanics of shear thickening behavior in magmas due to gas loss can be explained by the concepts of critical state soil mechanics, already elegantly applied by *Rutter et al.* [2006] and *Caricchi et al.* [2007] for partially molten rocks. In the following we will make a parallel between a fluid saturated soil and our samples considering that in our experiments the "pore fluid" phase is constituted by melt and gas bubbles. Figure 14 (redrawn from *Rutter et al.* [2006] and *Caricchi et al.* [2007]) shows how the experimental results and the mechanics of deformation can be expressed in terms of effective mean stress (total mean stress minus pore fluid pressure) and differential stress (double maximum shear stress [*Ranalli*, 1995]). We consider two end-member bubble-bearing systems: crystal-rich (Figure 14a) and crystal-poor magmas (Figure 14b). In bubble-free systems and for experiments performed in simple shear the initial effective mean stress is zero because the melt pressure is equal to the confining pressure [*Caricchi*

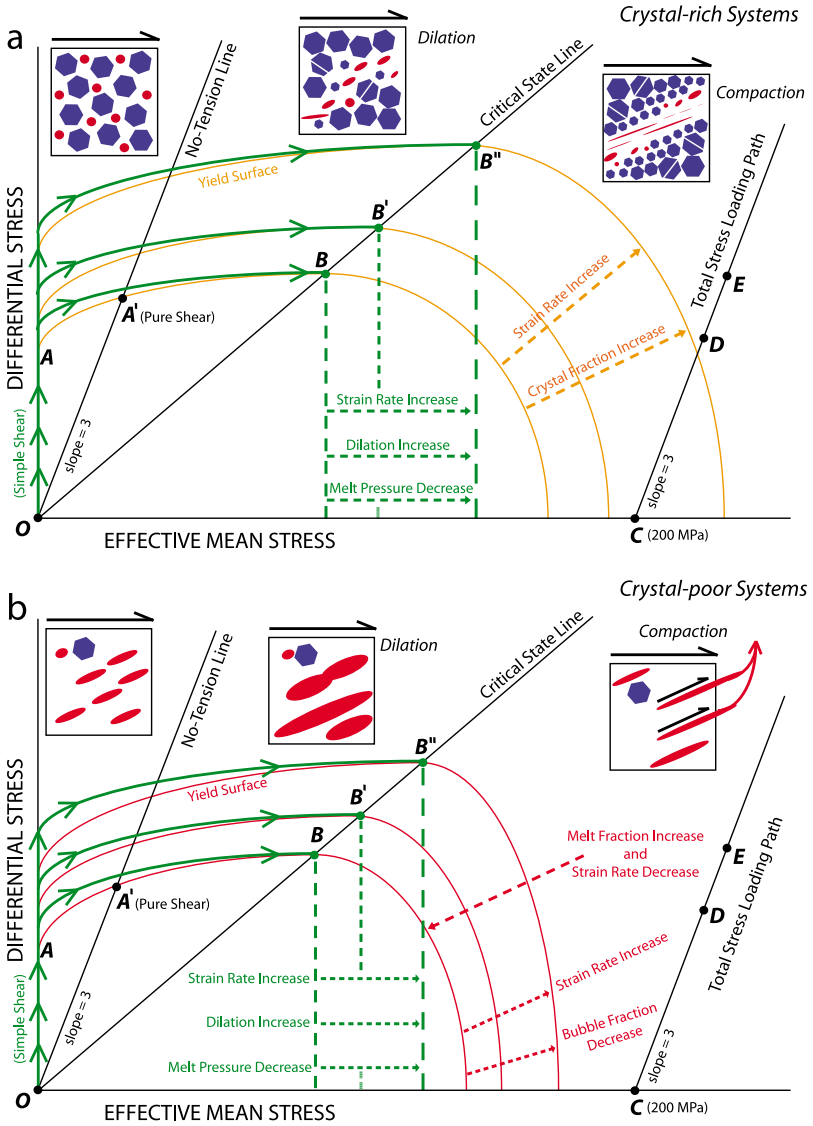

Figure 14. Relationship between experimental results and flow mechanics in terms of differential stress and effective mean stress: (figure redrawn from *Rutter et al.* [2006] and *Caricchi et al.* [2007]): (a) Crystal-rich and bubble-bearing systems as analogue for crystal-rich systems (55–65 vol.% crystals). The path OA represents the elastic loading trajectory for torsion experiments. At A (simple shear; A′ is the yield point for pure shear experiments, not performed in the present study), the loading path intersects the yielding surface where irreversible deformation of the sample starts. Increasing crystal fractions or applied strain rates expand the yielding surface; an increase of strain rate shifts the onset of flow from B to B′ and B″ (for more details, see *Rutter et al.* [2006] and *Caricchi et al.* [2007]). (b) Crystal-poor and bubble-bearing systems as analogue for crystal-poor systems (24–44 vol.% crystals). Both, relative increase of the melt fraction and reduction of the effective local strain rate, shrink the yield surface.

et al., 2007]. During elastic loading the differential stress increase (along OA) and the effective mean stress remains constant because simple shear stress implies that the compressive and extensive component of the stress are equal [*Caricchi et al.*, 2007]. Once the yielding envelop is reached, local dilation in the sample results in a local decrease of the melt pressure and the loading path starts deviating to the right-hand side of the diagram until flow at constant stress occurs in B (Figure 14a [*Caricchi et al.*, 2007; *Rutter et al.*, 2006]. In the following we will make use of the same concepts to discuss the rheological behavior of bubble- and crystal-bearing magmas.

5.1.3. The Origin of Shear Thickening in Bubble-Bearing and Crystal-Poor Magmas

[67] The starting conditions in a bubble- and crystal-bearing magma are identical to those in bubble-free systems (Figure 14b) but the gas bubbles react to local dilation (i.e., local decrease of pressure) by expanding. At the onset of yielding (point A, Figure 14b) the portion of the sample undergoing dilation suffers a decrease in local pressure, the gas bubbles expand and this favors coalescence and

generation of a permeable path for outgassing (Figure 14b). Once the gas is expelled from the system, the high temperature allows the melt to anneal in correspondence of these paths. The gas release from the sample keeps moving the yielding surface away from the origin of Figure 14b until a steady state situation (e.g., point B′; Figure 14b) is achieved and flow at constant stress occurs. This may explain the nature of shear thickening of crystal-poor magmas and the absence of strain effects (i.e., strain hardening) at constant strain rate, since gas escape occurs only during the yielding stage (along path A-B″; Figure 14b) where dilation and outgassing are gradually counterbalanced by gas compaction until flow at constant stress is achieved.

5.1.4. Fracture and Healing

[68] At low temperature (723 K; P1269 and P1271) crystal-poor magmas are affected by fracturing, which is testified by the sudden stress drops observed with increasing strain (Figure 3b). However, fracture healing also occurs, with the stress recovering after a drop, and is macroscopically evident in run P1271 (red line in Figure 3b). A previous experimental study from *Yoshimura and Nakamura* [2010] showed that fracture healing takes 1–3 h in water-poor (0.66 wt.% H_2O) natural rhyolitic obsidian (with polished surfaces) at 1123 K (melt viscosity of $1.51 \cdot 10^8$ Pa · s, calculated with the model of *Giordano et al.* [2008], according to the chemical composition reported in *Yoshimura and Nakamura* [2008]), at maximum confining pressure of 3 MPa. In our study, although we work at much lower temperature (723 K), the confining pressure (200 MPa) strongly shortens the time for fracture healing. We employed the equation for welding (or annealing or healing) time by viscous flow according to *Sparks et al.* [1999]:

$$\tau_v = \frac{\eta_{melt}}{\Delta P} \quad (2)$$

where τ_v is the healing time, η_{melt} is the viscosity of pure melt phase, ΔP is the effective applied load pressure (confining pressure minus pressure inside the fracture at its formation, which is zero if it is not filled by volatiles). We calculated the fracture healing time in run P1271 (red rheological curve in Figure 3b) in the last strain rate step ($4.67 \cdot 10^{-4}$ s^{-1}), using:

[69] - A melt viscosity of $7.76 \cdot 10^9$ Pa · s (melt viscosity of HGG measured at $4.58 \cdot 10^{-4}$ s^{-1} in run P1353 (773 K and 200 MPa), reported in Table 3 and Figure 5)

[70] - A ΔP of 200 MPa (which is the confining pressure of the experiment).

[71] The resulting healing time is 39 s. If this is the real healing time, it must be consistent with the amount of strain applied between two neighbor peaks of stress (corresponding to one complete cycle of stress drop and successive recovery) in Figure 3b. If we multiply the last strain rate ($4.67 \cdot 10^{-4}$ s^{-1}) applied in run P1271 (Figure 3b) with the calculated healing time (39 s), the strain obtained is 0.02. This value exactly corresponds to the "strain distance" between two neighbor peaks of stress in P1271 (Figure 3b).

[72] In conclusion, the dominant mechanical processes induced by deformation of crystal-poor magmas are bubble coalescence, formation of gas layers and successive outgassing. Although they require sufficient time (or strain) to occur (at least $\gamma > 1$; compare Figures 8a and 8b), at relatively high temperature (at least 773 K in haplogranitic magma), these processes are extremely fast (order of few seconds at strain rates higher than $1.00 \cdot 10^{-3}$ s^{-1}), because they occur during the yielding or *strain hardening* stage of the deformation. Here strain (or work) hardening at the transient yielding stage represents the first ductile response of the sample to the *change of strain rate* after the initial elastic linear increase of stress. It should not be confused with strain hardening occurring under conditions of steady state creep (when the sample "flows" after the transient yielding stage). If we consider the yielding stages after changing strain rate in run P1265 (see the blue rheological curve in the stress versus strain diagram in Figure 3b), we observe a stabilization of the stress after imposing a new strain rate (higher than the previous one) within 20 s maximum, from $5.28 \cdot 10^{-4}$ s^{-1} to $1.07 \cdot 10^{-3}$ s^{-1}, and 4 s maximum, from $2.45 \cdot 10^{-3}$ s^{-1} to $2.53 \cdot 10^{-3}$ s^{-1}. This is the reason why gas escape is invisible to any strain effect at steady state conditions of stress at a given constant strain rate. Shear thickening represents the unique recording of outgassing occurring during deformation of dilute magmatic suspensions. At lower temperature (723 K) magmas are strongly affected by extensive brittle response inducing diffuse fracturing in the melt phase.

5.2. Magmas With Intermediate Crystallinity

5.2.1. The Change of Non-Newtonian Regime: The Appearance of Shear Thinning

[73] Magmas with intermediate crystallinity, containing 44 vol.% crystals and initial 12 vol.% bubbles, mostly display a transient behavior while increasing strain rate, from shear thickening to shear thinning (Figures 3c and 4), with shear thickening characterizing only the rheology at low strain (up to approximately 1). Shear thinning is associated with crystal size reduction and the formation of shear zones. While aligning, crystal fracturing results in intensive crystal size reduction and promotes the formation of shear zones that facilitate the migration and flow of melt to produce melt-enriched zones. As previously discussed, melt and crystal rearrangement (including crystal breakage) can be explained in terms of local dilation-compaction processes occurring during the yielding stage of deformation before approaching the critical state of the material (Figure 14a). The magnitude of dilation and compaction processes is directly proportional to the applied differential stress (or strain rate) resulting in the shear thinning behavior observed [*Caricchi et al.*, 2007]. At the experimental conditions of these experiments, quartz has a brittle response [*Deubelbeiss et al.*, 2011]. Brittle interactions are favored by deformation that aligns solid particles in layers parallel to the mean flow direction. The local reduction of crystal size results in a local decrease of viscosity, which in turn, promotes additional shear localization. Crystal breakage is related to intense stress localization at grain contacts [*Forien et al.*, 2011].

5.2.2. Bubble Coalescence Versus Bubble Break-up

[74] We find microstructural features that clearly suggest the occurrence of both bubble coalescence (Figures 9a and 13b–13d) and bubble break-up (Figures 9b and 13f). Specifically, bubble break-up is evident within shear bands (Figure 9b) where the strain accommodation is highest. This process has been observed in numerous previous studies on bubble- or droplet-bearing suspensions undergoing simple

shear deformation [e.g., *de Bruijn*, 1993; *Müller-Fischer et al.*, 2008]. As shown in the X-ray synchrotron-based 3D rendering (Figures 13f–13h), bubbles are very thin (with a minimum thickness of 1 μm) and highly extended (up to 100 μm) filaments before their break-up. Under continuous deformation, these filaments are fated to be torn off (see "bubble boudinage" in Figure 13g) and generation of broken-off tips occurs. In many cases these tips (with 1 μm in equivalent diameter) partially relax to an ellipsoidal shape after break-up (Figures 13f and 13g). The break-up does not concern the bubble tips only, but also the fracture of the major bubble body (Figures 9b and 13h). This larger break-up favors the formation of smaller (daughter or satellite) bubbles, which can be ten times shorter than the original bubble prior to major break-up (Figure 9b). However, they do not relax, but they remain stretched and deformed, testifying that the strain rate in the shear zone is still high enough to deform them. Based on the microstructural information, bubble break-up occurs when the bubbles achieve very large elongation, typically greater than 10 times the initial bubble radius (e.g., compare Figures 13a and 13h). A similar observation was presented by *Müller-Fischer et al.* [2008] in their air bubble deformation experiments in glucose syrup and silicon oil. However, our observation totally departs from drop break-up [e.g., *Stone*, 1994] that occurs when the ratio between elongation axis and starting radius is about 40. The evident discrepancy of results is because of the genetic difference between gas bubbles and liquid drops, where a gas bubble is less viscous than a liquid drop. This implies that the viscosity ratio between gas bubble and melt is different from the viscosity ratio between liquid drop and suspending fluid. For instance, the drop/suspension viscosity ratio in *Bentley and Leal* [1986] and *Stone* [1994] is between $1.08 \cdot 10^{-3}$ and 100. In our experiments the CO_2-rich bubble/silicate melt viscosity ratio is between $1.02 \cdot 10^{-16}$ at 673 K and $8.48 \cdot 10^{-10}$ at 1023 K (where: melt viscosity at different temperatures has been measured in section 4.2.1; CO_2-rich bubble viscosity values at experimental temperature and pressure conditions are from NIST - National Institute of Standards and Technology). This discrepancy in viscosity ratio up to 13 order of magnitude would explain why the elongation and break-up of gas bubbles [e.g., *Müller-Fischer et al.*, 2008; this study] are not comparable to the deformation and rupture of liquid drops [e.g., *Bentley and Leal*, 1986; *Stone*, 1994] and why the break-up occurs at lower values of bubble elongation axis/starting radius ratio (10 in our experiments; 40 in drop break-up tests in *Stone* [1994]).

5.2.3. Rheological Transition: Shear Thickening to Shear Thinning Versus Unsteady Flow to Steady Flow

[75] We find a strong link between the change of Non-Newtonian regime (shear thickening to shear thinning) and the change of flow conditions (unsteady to steady flow) at 823 K (see section 4.5.2). For instance, at 823 K (see P1266, P1268 and P1276 in Table 3) deformation results in bubbles of different shape:

[76] - Initial oblate shape, which is the typical shape promoting bubble coalescence and outgassing and, thus, explains the occurrence of shear thickening with strain rate increase.

[77] - Final prolate shape, which inhibits the outgassing efficiency (since bubble coalescence occurs in one single direction) and, thus, contributes to the shear thinning regime.

[78] Given also the results on bubble relaxation time reported in Table 5, we should expect that: small (radius < 5 μm) bubbles become prolate ($\lambda < t_{deformation}$); large (radius > 5 μm) bubbles become oblate ($\lambda > t_{deformation}$). However, this is valid only for Newtonian viscosity of the melt in the absence of bubble coalescence and break-up inducing changes in bubble size (or equivalent radius). At 823 K, prior to deformation, most bubbles display 10–15 μm in average diameter at least (see P1270 in Figure 1); therefore, these bubbles are fated to deform as oblate object. This would favor coalescence, a consequent increase of bubble size and ensure that their oblate shape is maintained during deformation (preservation of unsteady flow conditions). This allows gas escape and promotes shear thickening. However, the release of gas produces a decrease in bubble content (Figure 7c), a decrease of their size, and an increase of the effective crystallinity of the system. At this point, the localization in strain is not anymore in gas planes (that already vanished with outgassing), but in melt-enriched portions between solid crystals. The residual bubbles (that are smaller in size after outgassing) are forced to change shape while deforming, because the conditions of deformation (increase of crystallinity and strain partitioning between crystals and melt) are changed. Therefore, the residual smaller bubbles are not able to coalesce because of the novel prolate shape. In addition, bubbles (as passive phases carried along with silicate melt) become unstable in the crystal-free shear bands and break up (Figure 9b). In turn, bubble break-up generates bubble daughters with smaller size (equivalent radius < 5 μm), favoring the prolate shape of bubble deforming and, thus, ensuring the steady flow conditions. The change of shape is determined by the increase of strain rate. The transition from shear thickening + unsteady flow conditions to shear thinning + steady flow conditions is observed at $\dot{\gamma} \geq 1.00 \cdot 10^{-3}$ s^{-1} (Table 3).

[79] In summary, a combination of the two Non-Newtonian effects (shear thickening and shear thinning) occurs at intermediate crystallinity. The predominance of one effect over the other mainly depends on temperature conditions and applied strain rate. At temperatures exceeding 773 K, shear thickening is followed by shear thinning. The passage from shear thickening to shear thinning is constantly located at $1.00 \cdot 10^{-3}$ s^{-1} highlighting that the rheology of such magmas is strongly strain rate dependent and independent of the total strain or time spent to deform the sample.

5.3. Crystal-Rich Magmas

5.3.1. Strain Partitioning

[80] Shear thinning is the dominant mechanism controlling the rheology of three-phase magmas with high crystallinity (55 vol.% crystals and 10 vol.% bubbles). Microstructural information assembled from different samples deformed at different values of strain, reveals that solid crystals are arranged in antithetic structures at high angle (−45° to −50°) under low strain (up to γ = 1.05). The formation of shear zones promotes crystal redistribution, characterized by antithetic alignment of the particles at lower angle (−25°). The strain partitioning marks the internal disparity between shear zones and particle clusters. Strongly stretched bubbles are concentrated in melt-enriched shear bands (Figure 10) and are, theoretically, liable to coalesce under deformation. However, differently from observations in recent

experiments of *Laumonier et al.* [2011], bubble break-up appears as the common process within shear bands. Bubble coalescence can be suppressed by several processes: (1) higher crystal content, which promotes the formation of shear bands and particle clusters, and strain/stress localization in the shear bands might lead to bubble break-up of the newly formed extended gas film due to very high local capillary numbers; (2) bubble relaxation time is shorter than the timescale of deformation resulting in prolate bubble shapes that deform in one direction (parallel to shear bands located between crystal clusters). Such deformation decreases the outgassing efficiency as coalescence can only occur if bubbles are located in the same plane and along the same direction. Due to lack of gas escape, the initial bubble content prior to deformation is preserved in the final deformed microstructures (except run P1140 displaying a loss of bubble volume of 1 vol.%).

5.3.2. Crystal Clusters and Rigid Bubbles

[81] Some experiments (P1191, P1193 and P1197) exhibit shear thickening, which is most probably caused by combined processes: low capillary numbers ($Ca < 1$) and consequent increase of effective crystal volume due to rigid bubbles attaining a potential maximum packing fraction, where a continuous crystal network could become the portion of the sample that accumulates most of the stress while deformation rate increases. This further promotes brittle failure of the magma at high temperature and pressure.

[82] In summary, three-phase crystal-rich magmas exhibit shear thinning as the dominant Non-Newtonian behavior related to crystal size reduction and shear banding. Bubble coalescence and outgassing processes are impeded due to higher crystal content, pronounced strain localization and bubble deformation producing prolate shapes in the temperature range 873–923 K. Bubble break-up is favored under these conditions. Shear thickening occurs as well that might be related to the formation of particle super-clusters that locally increase the stress while increasing the strain rate. This specific behavior invariably represents a preliminary step prior to fracturing the sample.

5.4. Crystal Mushes

5.4.1. Shear Zoning

[83] The rheology of crystal mushes (65 vol.% crystals and 9 vol.% bubbles) is characterized by accentuated shear thinning resulting from higher crystal content that enhances stress/strain disparity between bubble-melt-rich shear zones and surrounding particle aggregates. Crystals are antithetically arranged at high angle (mean of $-60°$); but in proximity of shear bands, they are aligned at slightly lower angle (about $-50°$). A close relation between CSD, crystal content and strain rate applied is observed and implies that crystal size reduction is a prominent process in these experiments. Promoted by impingement microcrack formation during deformation [*Passchier and Trouw*, 2005], crystal size reduction is highly favored at high crystal content and requires lower values of strain at a given strain rate than for comparable experiments with lower crystallinity. These magmas lack any signs of bubble coalescence and outgassing (Figure 13).

5.4.2. Shear Jamming

[84] Shear thickening was identified in three experiments (P1240, P1263 and P1491) and is ascribed to the same mechanism as discussed for crystal-rich magmas above. However, additional processes potentially occur in such crystal-rich magmas: *van der Molen and Paterson* [1979] observed a distinct change from suspension-like flow to framework-controlled (or solid-like) behavior at a crystal concentration between 65 and 70 vol.% in partially molten granites; whereas *Rutter and Neumann* [1995] observed a progressive change in strength over a wide range of crystal concentrations (from 23 to 97 vol.%). The formation of a continuous crystal network is caused by groups of solid particles that move together like super-particle cluster [*Petford*, 2009]. This implies that crystal-rich magmas can behave as solid rocks, where local blocking and chocking occur while deforming [*Petford and Koenders*, 2003]. A similar mechanism of melt flow blockage/jamming in the presence of a continuous crystal network could potentially operate in crystal mushes too and cannot a priori be excluded for our experiments.

[85] In summary, the rheologic response of crystal mushes to deformation is dominated by shear thinning due to effective rupture of the crystal framework, successive crystal size reduction and formation of shear zones. Bubble coalescence and outgassing processes are absent. Within shear bands, bubble break-up occurs due to massive strain localization. Prolate shapes of deformed bubbles would be expected in the chosen temperature range for deforming crystal mushes (873–1023 K). Bubbles are expected to behave rigidly over a wide range of strain rates, except for bubbles stretched in the shear zones. The observed shear thickening might be attributed to low capillary numbers ($Ca < 1$) and consequent increase of effective crystal volume; the increased strength of the crystal framework promotes solid-like behavior of the magma and favors its brittle failure.

5.5. The Complexity of Non-Newtonian Regimes in Three-Phase Magmas

[86] The definition of viscosity as internal resistance of the material to flow implies that local instabilities (shear bands, gas channels, gas loss, crystal size reduction, formation of super-particle clusters, bubble shape, rigid and/or soft response of gas bubbles) exert prominent control on magma viscosity and, hence, rheology. Non-Newtonian effects are the result of combined, different, even contrasting (strain rate-dependent) mechanical processes, acting concomitantly. The most frequent dominant Non-Newtonian regimes are:

for crystal-poor magmas (24–44 vol.% crystals; 12 vol.% bubbles):

$$(Shear\ Thickening)_{bulk} = (Thickening)_{gas\ loss} - (Thinning)_{bubble\ coalescence} - (Thinning)_{melt\ structure}$$

for crystal-rich magmas (55–65 vol.% crystals; 9–10 vol.% bubbles):

$$(Shear\ Thinning)_{bulk} = (Thinning)_{crystal\ size\ reduction+shear\ banding} + (Thinning)_{melt\ structure} + (Thinning)_{bubble\ break-up} - (Thickening)_{gas\ loss}$$

In the current experimental study, the rheology of magma is the result of continuous internal rearrangement of different phases submitted to deformation, as deformation rate increases. Initial Newtonian behavior of the investigated crystal-bubble-melt suspension gives rise to shear thinning and thickening at elevated strain rates. The rheology of deforming magmas is, however, highly complex since several phases (crystals, bubbles and melt) interact simultaneously with each other in different ways. The shear thickening effect observed in this study that is attributed to outgassing, was not described before. The study of *Thies* [2002], for example, investigated porous (up 60 vol.% pores) and crystal-bearing (5–15 vol.% needle shaped crystals) melts separately and modeled the rheology of the inferred three-phase systems as a function of three-step shear thinning behavior, where each phase contributes to shear thinning. Unfortunately, such a model does not work if all phases (melt, crystals and real gas-pressurized bubbles) simultaneously interact. Thus, we notice that combination of different rheologies in a unique model is inappropriate, since the respective binary rheologies of crystal-bearing magmas and bubble-bearing systems are genetically and unmistakably different.

[87] Although the investigated magma rheology is strongly strain rate dependent, we do not exclude that a certain amount of strain is required to achieve significant interactions between bubbles, crystals and melt and generate internal instabilities, such as bubble coalesce and crystal fragmentation.

[88] The proposal of *Caricchi et al.* [2007] that further deformation at higher strain rates will ultimately lead to Pseudo-Binghamian behavior has been evaluated by the present study on three-phase magma. Our data show that in three-phase system shear thinning or shear thickening behavior grades to brittle behavior with increasing strain rate, thus implying a physical passage from Non-Newtonian regime to a Mohr-Coulomb type behavior.

6. Applications to Natural Volcanic Systems

[89] Our experimental results provide some fundamental information toward the understanding of magma rheology and consequent eruption mechanisms.

6.1. Banded Obsidians and Shallow Crystal-Poor Intrusions

[90] Crystal-poor magmas can be compared to banded obsidian flows at the surface, and shallow intrusions stalled at depth. Banded obsidians are characterized by a continuous layering of crystal-poor glass and vesicle-rich planes [e.g., *Gonnermann and Manga*, 2005]. The vesicle-rich layers represent the clear account of previous bubble coalescence induced by deformation and present highly permeable gas planes, where gas loss occurred additionally reducing the tendency to explosive bubble pressurization/fragmentation. Outgassing induced by shearing can also explain the formation of obsidian pyroclasts by magma densification/compaction with degassing/outgassing in a zone of high shear rates at conduit margins [e.g., *Stasiuk et al.*, 1996; *Rust et al.*, 2004; *Rust and Cashman*, 2007]. Structures attributed to fracturing and healing (e.g., tuffisite veins in *Tuffen et al.* [2003]; healed fractures in pyroclastic obsidian in *Cabrera et al.* [2011]) demonstrate that such processes lead to an inevitable viscosity increase and brittle response of the magma depleting in volatiles during shearing.

[91] In the case of crystal-poor, subsurficial intrusions, the same processes (extensive outgassing and consequent increase in viscosity) result in the stalling of magma at depth. Outgassing induces a loss of driving force (enhanced by a drop in gas pressure) accompanied by microlite crystallization [e.g., *Hammer et al.*, 2000; *Cashman and Blundy*, 2000], both together contributing to a significant increase of the viscosity effectively terminating magma ascent.

6.2. Lava Domes and Near-Solidus Granitoid Plutons

[92] Lava domes (e.g., andesitic dome from Soufriere Hills Volcano, Montserrat, in *Murphy et al.* [2000]; dacitic dome from Santiaguito, Guatemala, in *Holland et al.* [2011]) and nearly fully crystallized granitoid intrusions (e.g., granodiorite, including blocks of diabase, quartz diorite and granite, from Crater Lake caldera, Oregon, USA, in *Bacon and Druitt* [1988] and *Bacon* [1992]; tonalite and granodiorite plutons from the Adamello Massif, Italy, in *Blundy and Sparks* [1992]; granodiorite and monzo-diorite from schlieren in Sawmill Canyon area, Sierra Nevada, California, USA, in *Paterson et al.* [2008]) are examples of highly crystallized and bubble-bearing magmas. Lava domes are generally crystal-rich [e.g., *Sparks*, 1997] and exhibit internal crystal fracturing [e.g., *Allen and McPhie*, 2003] and lateral shear zones, promoting ascent/extrusion along the conduit walls [e.g., *Hale and Wadge*, 2008]. The behavior of gas bubbles within the shear bands plays an important role. Given our microstructural results, bubble break-up within the shear zone tends to inhibit outgassing, conserves the content of bubbles and maintains lower viscosity in the shear bands. These weaker structures within a dome are susceptible to subsequent reactivation. As a consequence the preservation of bubbles in shear zones can affect the longevity of shear bands within a volcanic conduit and the final extrusion of highly viscous bodies, such as lava domes.

[93] At depth, mushy plutons can be mobilized by the addition of volatiles (mainly H_2O) and heat released by ascending hydrous mafic magmas [*Bachmann and Bergantz*, 2008] that induce a significant decrease of the bulk viscosity (and potentially the density) of the granitoid body. Mobilization of granitoid, partially crystallized mushes would be favored by strain localization and this could lead to a large-scale eruption (e.g., Fish Canyon [*Burgisser and Bergantz*, 2011]). If no strain localization occurs magma is essentially rheologically dead within the Earth's crust.

6.3. Efficiency of Outgassing in Magmas Ascending Along Volcanic Conduits

[94] In our experiments permeability and gas release occurred at low vesicularity (maximum 12 vol.% bubbles), which is in contrast with the higher percolation threshold estimated for natural systems. The location of the percolation threshold (which is the limit of vesicularity below which permeability is zero [*Rust and Cashman*, 2011]) has been variably placed [*Rust and Cashman*, 2011, and reference therein]. However, shearing occurring within volcanic conduits plays an important role in controlling the permeability thresholds in natural systems. For instance, torsional deformation experiments on bubble-bearing melt

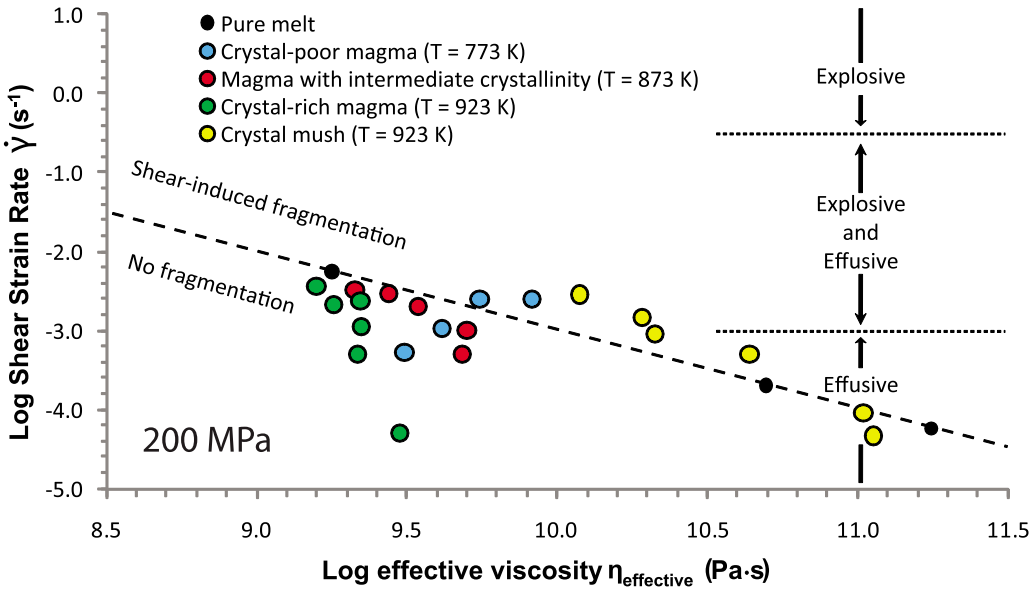

Figure 15. Logarithm of shear strain rate ($\dot{\gamma}$) versus logarithm of effective viscosity ($\eta_{effective}$): Results from four different runs (P1265 = crystal-poor magma; P1270 = magma with intermediate crystallinity; P1273 = crystal-rich magma; P1260 = crystal mush). The fragmentation onset has been measured during experimental determination of critical strain rates of pure melt (HGG) at different temperatures (673–723 K) under confining pressure (200 MPa).

[*Okumura et al.*, 2006, 2008, 2009; *Caricchi et al.*, 2011] demonstrate that simple shear can produce high permeability at vesicularity lower than the 43 vol.% observed in the decompression experiments of *Burgisser and Gardner* [2005]. The present study confirms that bubble coalescence can initiate at relatively low bubble content (12 vol.%) in crystal-poor magmas (up to 44 vol.% crystals), promoting formation of gas planes and gas release from the system. An increase of crystallinity seems to reduce bubble coalescence. The control of strain localization on gas permeability is also observed in natural pumice samples [*Klug and Cashman*, 1996; *Klug et al.*, 2002; *Wright et al.*, 2006; *Wright and Weinberg*, 2009; *Wright et al.*, 2009], although the vesicularity of such pumice samples is higher than the vesicularity in our starting materials (about 70 vol.% versus 12 vol.%) because of the additional vesiculation induced by decompression process during volcanic eruption. For the same reason, BSD and BND in natural samples are strongly affected by decompression processes; this makes difficult to directly compare our BSDs and BNDs with those from natural samples.

6.4. Shear-Induced Fragmentation: Explosive or Effusive Volcanic Activity?

[95] The current experiments allow inference on processes controlling shear-induced fragmentation [e.g., *Gonnermann and Manga*, 2003]. Figure 15 illustrates how shear deformation can promote magma fragmentation in both Non-Newtonian regimes (shear thickening and shear thinning). Crystal-poor magmas and crystal mushes represent the best candidates for shear fragmentation. In fact, in crystal-poor magmas outgassing induces the increase of magma viscoelastic response and failure; in crystal-rich magmas shear bands are weak regions stressed under high strain rates that are prone to failure. However, decompression is an inevitable consequence of magma ascent and, therefore, always operates in the background.

7. Summary, Conclusions and Perspectives

[96] The present experimental study emphasizes the rheologic complexity of real magmas composed of different phases (crystals, bubbles, melt). The experimental strain tests were conducted on a silica-rich (granitic) analogue material ($HGGB_3$) simulating magmas ranging from dilute suspensions (24 vol.% crystals) to crystal mushes (65 vol.% crystals), within a narrow range of bubble contents (9–12 vol.%). Experiments were performed at constant pressure (200 MPa), isothermally (673–1023 K), in strain rate stepping ($1 \cdot 10^{-5}$–$4 \cdot 10^{-3}$ s^{-1}) mode. The presence of bubbles causes a marked decrease of relative viscosity, compared to an identical, crystal-bearing system [*Caricchi et al.*, 2007]. The rheology of the three-phase system is strongly strain rate dependent, although reasonable values of strain (generally: $\gamma > 1$) are required to produce typical microstructures. Two dominant Non-Newtonian regimes were identified: shear thinning in crystal-rich magmas (44–65 vol.% crystals); shear thickening in crystal-poor systems (24–44 vol.% crystals). Shear thinning is predominantly associated with discrete redistribution of suspended crystals, their size reduction and formation of shear banding. Shear thickening is dominantly the expression of permeable outgassing occurring during deformation, which depletes the melt in volatiles and results in an increasing viscosity of the magmatic system (translated into a reduction of volumetric bubble content). We also observe both Non-Newtonian effects in some experiments

demonstrating the complex contemporaneous interaction occurring between melt, crystals and bubbles. To reconcile the rheological behavior of natural magmas, it is mandatory to combine experimental results and observations about their specific microstructures and the macro- and micro-textures/structures of natural rocks.

[97] Further rheological studies on these systems require extension to higher gas bubble content (up to 25 vol.%) to better constrain their role during deformation and quantify their influence on gas permeability in partially crystallized systems.

[98] **Acknowledgments.** The present research was supported by Swiss National Foundation (grant 200020–120221). Luca Caricchi was supported by NERC grant (NE/G012946/1). We wish to thank: Robert Hoffmann for his precious technical support at the Rock Deformation Laboratory of ETH-Zurich; Remi Champallier for the technical support at the Rock Deformation Laboratory in CNRS in Orleans; Stefanie Wirth and Adrian Gilli (Climate Geology, ETH-Zurich) for assisting with coulometric CO_2 analyses; Jean-Michel Lévy and Marina Aletti (ISTO, Orléans, France) for their impeccable contribution during FTIR analyses of our haplogranitic glasses; Peter Modregger (PSI, Villigen, Switzerland) for his fundamental supervision during X-ray tomographic scans at the TOMCAT beamline. We would like to further acknowledge: Alberto Luisoni AG (Switzerland) for the provision of quartz crystals used as solid particles in our magmas; Nabaltec AG (Germany) for the supply of very fine-grained aluminum hydroxide (APYRAL 60CD) used for the preparation of the starting material. The comments of Satoshi Okumura and Heather M. Wright greatly improved the manuscript. This work is dedicated to Luigi Burlini.

References

Abramoff, M. D., P. J. Magelhaes, and S. J. Ram (2004), Image processing with ImageJ, *Biophot. Int.*, *11*, 36–42.

Allen, S. R., and J. McPhie (2003), Phenocryst fragments in rhyolitic lavas and lava domes, *J. Volcanol. Geotherm. Res.*, *126*, 263–283, doi:10.1016/S0377-0273(03)00151-3.

Arbaret, L., M. Bystricky, and R. Champallier (2007), Microstructures and rheology of hydrous synthetic magmatic suspensions deformed in torsion at high pressure, *J. Geophys. Res.*, *112*, B10208, doi:10.1029/2006JB004856.

Ardia, P., D. Giordano, and M. W. Schmidt (2008), A model for the viscosity of rhyolite as a function of H_2O-content and pressure: A calibration based on centrifuge piston cylinder experiments, *Geochim. Cosmochim. Acta*, *72*, 6103–6123, doi:10.1016/j.gca.2008.08.025.

Bachmann, O., and G. W. Bergantz (2008), Rhyolites and their source mushes across tectonic settings, *J. Petrol.*, *49*, 2277–2285, doi:10.1093/petrology/egn068.

Bacon, C. R. (1992), Partially melted granodiorite and related rocks ejected from Crater Lake caldera, Oregon, *Trans. R. Soc. Edinburgh Earth Sci.*, *83*, 27–47, doi:10.1017/S0263593300007732.

Bacon, C. R., and T. H. Druitt (1988), Compositional evolution of the zoned calkaline magma chamber of Mount Mazama, Crater Lake, Oregon, *Contrib. Mineral. Petrol.*, *98*, 224–256, doi:10.1007/BF00402114.

Bagdassarov, N. S., and D. B. Dingwell (1992), A rheological investigation of vesicular rhyolite, *J. Volcanol. Geotherm. Res.*, *50*, 307–322, doi:10.1016/0377-0273(92)90099-Y.

Bagdassarov, N. S., and D. B. Dingwell (1993a), Frequency-dependent rheology of vesicular rhyolite, *J. Geophys. Res.*, *98*, 6477–6487, doi:10.1029/92JB02690.

Bagdassarov, N. S., and D. B. Dingwell (1993b), Deformation of foamed rhyolites under internal and external stresses: An experimental investigation, *Bull. Volcanol.*, *55*, 147–154, doi:10.1007/BF00301512.

Bagdassarov, N. S., and A. Dorfman (1998a), Granite rheology: Magma flow and melt migration, *J. Geol. Soc.*, *155*, 863–872, doi:10.1144/gsjgs.155.5.0863.

Bagdassarov, N. S., and A. Dorfman (1998b), Viscoelastic behavior of partially molten granites, *Tectonophysics*, *290*, 27–45, doi:10.1016/S0040-1951(98)00010-9.

Bagdassarov, N. S., D. B. Dingwell, and S. L. Webb (1994), Viscoelasticity of crystal-bearing and bubble-bearing rhyolite melts, *Phys. Earth Planet. Inter.*, *83*, 83–99, doi:10.1016/0031-9201(94)90066-3.

Bagdassarov, N. S., A. Dorfman, and D. B. Dingwell (2000), Effect of alkalis, phosphorus, and water on the surface tension of haplogranite melt, *Am. Mineral.*, *85*, 33–40.

Barnes, H. A. (1989), Shear thickening (dilatancy) in suspensions of non-aggregating solid particles dispersed in Newtonian liquids, *J. Rheol.*, *33*, 329–366, doi:10.1122/1.550017.

Barnes, H. A. (1997), Thixotropy: A review, *J. Rheol.*, *70*, 1–33.

Behrens, H., C. Romano, M. Nowak, F. Holtz, and D. B. Dingwell (1996), Near-infrared spectroscopic determination of water species in glasses of system MAlSi(3)O(8) (M = Li, Na, K): An interlaboratory study, *Chem. Geol.*, *128*, 41–63, doi:10.1016/0009-2541(95)00162-X.

Behrens, H., N. Tamic, and F. Holtz (2004), Determination of the molar absorption coefficient for the infrared absorption band of CO_2 in rhyolitic glasses, *Am. Mineral.*, *89*, 301–306.

Bentley, B. J., and L. G. Leal (1986), An experimental investigation of drop deformation and breakup in steady, two-dimensional linear flows, *J. Fluid Mech.*, *167*, 241–283.

Blank, J. G., and R. A. Brooker (1994), Experimental studies of carbon dioxide in silcate melts: Solubility, speciation and stable isotope behavior, in *Volatiles in Magmas*, *Rev. Mineral. Geochem.*, vol. 30, edited by M. R. Carroll and J. R. Holloway, pp. 157–186, Mineral. Soc. of Am., Washington, D. C.

Blundy, J., and R. S. J. Sparks (1992), Petrogenesis of mafic inclusions in granitoids of the Adamello Massif, Italy, *J. Petrol.*, *33*, 1039–1104.

Blundy, J., K. V. Cashman, and M. Humphreys (2006), Magma heating by decompression-driven crystallization beneath andesite volcanoes, *Nature*, *443*, 76–80, doi:10.1038/nature05100.

Brückner, R., and J. Deubener (1997), Description and interpretation of the two phase flow behaviour of melts with suspended crystals, *J. Non-Cryst. Solids*, *209*, 283–291, doi:10.1016/S0022-3093(96)00571-6.

Burgisser, A., and G. W. Bergantz (2011), A rapid mechanism to remobilize and homogenize crystalline magma bodies, *Nature*, *471*, 212–215, doi:10.1038/nature09799.

Burgisser, A., and J. E. Gardner (2005), Experimental constraints on degassing and permeability in volcanic conduit flow, *Bull. Volcanol.*, *67*, 42–56, doi:10.1007/s00445-004-0359-5.

Cabrera, A., R. F. Weinberg, H. M. N. Wright, S. Zlotnik, and R. A. F. Cas (2011), Melt fracturing and healing: A mechanism for degassing and origin of silicic obsidian, *Geology*, *39*, 67–70, doi:10.1130/G31355.1.

Caricchi, L. (2008), Rheology and physical properties of crystal-bearing magmas, PhD thesis, Inst. Mineral. Petrol., ETH-Zurich, Zurich.

Caricchi, L., L. Burlini, P. Ulmer, T. Gerya, M. Vassalli, and P. Papale (2007), Non-Newtonian rheology of crystal-bearing magmas and implications for magma ascent dynamics, *Earth Planet. Sci. Lett.*, *264*, 402–419, doi:10.1016/j.epsl.2007.09.032.

Caricchi, L., D. Giordano, L. Burlini, and P. Ulmer (2008), Rheological properties of magma from the 1538 eruption of Monte Nuovo (Phlegrean Fields, Italy): An experimental study, *Chem. Geol.*, *256*, 158–171, doi:10.1016/j.chemgeo.2008.06.035.

Caricchi, L., A. Pommier, M. Pistone, J. Castro, A. Burgisser, and D. Perugini (2011), Strain-induced magma degassing: Insights from simple-shear experiments on bubble bearing melts, *Bull. Volcanol.*, *73*, 1245–1257, doi:10.1007/s00445-011-0471-2.

Cashman, K., and J. Blundy (2000), Degassing and crystallization of ascending andesite and dacite, *Philos. Trans. R. Soc. London A*, *358*, 1487–1513, doi:10.1098/rsta.2000.0600.

Champallier, R., M. Bystricky, and L. Arbaret (2008), Experimental investigation of magma rheology at 300 MPa: From pure hydrous melt to 76 vol.% of crystals, *Earth Planet. Sci. Lett.*, *267*, 571–583, doi:10.1016/j.epsl.2007.11.065.

Chong, J. S., E. B. Christiansen, and A. D. Baer (1971), Rheology of concentrated suspensions, *J. Appl. Polym. Sci.*, *15*, 2007–2021, doi:10.1002/app.1971.070150818.

Cordonnier, B., K.-U. Hess, Y. Lavallée, and D. B. Dingwell (2009), Rheological properties of dome lavas: Case study of Unzen volcano, *Earth Planet. Sci. Lett.*, *279*, 263–272, doi:10.1016/j.epsl.2009.01.014.

de Bruijn, R. A. (1993), Tipstreaming of drops in simple shear flows, *Chem. Eng. Sci.*, *48*, 277–284, doi:10.1016/0009-2509(93)80015-I.

Deubelbeiss, Y., B. Kaus, J. P. Connolly, and L. Caricchi (2011), Potential causes for the non-Newtonian rheology of crystal-bearing magmas, *Geochem. Geophys. Geosyst.*, *12*, Q05007, doi:10.1029/2010GC003485.

Deubener, J., and R. Brückner (1997), Influence of nucleation and crystallisation on the rheological properties of lithium disilicate melt, *J. Non-Cryst. Solids*, *209*, 96–111, doi:10.1016/S0022-3093(96)00554-6.

Devine, J. D., J. E. Gardner, H. P. Brack, G. D. Layne, and M. J. Rutherford (1995), Comparison of microanalytical methods for estimating H_2O contents of silicic volcanic glasses, *Am. Mineral.*, *80*, 319–328.

Dingwell, D. B. (1995), Relaxation in silicate melts: Some applications, in *Structure, Dynamics and Properties of Silicate Melts*, *Rev. Mineral. Geochem.*, vol. 32, edited by J. F. Stebbins, P. F. McMillan, and D. B. Dingwell, pp. 21–66, Mineral. Soc. of Am., Washington, D. C.

Dingwell, D. B., and S. L. Webb (1990), Relaxation in silicate melts, *Eur. J. Mineral.*, *2*, 427–449.

Dingwell, D. B., N. S. Bagdassarov, G. Y. Bussod, and S. L. Webb (1993), Magma rheology, in *Experiments at High Pressure and Applications to the Earth's Mantle*, *Mineral. Assoc. Canada, Short Course Handbooks*, vol. 21, edited by R. W. Luth, pp. 131–196, Mineral. Assoc. Can., Québec, Québec, Canada.

Dingwell, D. B., C. Romano, and K.-U. Hess (1996), The effect of water on the viscosity of a haplogranitic melt under P-T-X conditions relevant to silicic volcanism, *Contrib. Mineral. Petrol.*, *124*, 19–28, doi:10.1007/s004100050170.

Divoux, T., E. Bertin, V. Vidal, and J.-C. Géminard (2009), Intermittent outgassing through a non-Newtonian fluid, *Phys. Rev. E*, *79*, 056204, doi:10.1103/PhysRevE.79.056204.

Fischer, K. (1935), New method for the quantum analytical instruction of the water proofing from liquids and solid bodies, *Angew. Chemie*, *48*, 394–396.

Forien, M., L. Arbaret, A. Burgisser, and R. Champallier (2011), Experimental constrains on shear-induced crystal breakage in magmas, *J. Geophys. Res.*, *116*, B08217, doi:10.1029/2010JB008026.

Gaillard, F., B. Scaillet, M. Pichavant, and J. L. Beny (2001), The effect of water and fO(2) on the ferric-ferrous ratio of silicic melts, *Chem. Geol.*, *174*, 255–273, doi:10.1016/S0009-2541(00)00319-3.

Gardner, J. E. (2007), Bubble coalescence in rhyolitic melts during decompression from high pressure, *J. Volcanol. Geotherm. Res.*, *166*, 161–176, doi:10.1016/j.jvolgeores.2007.07.006.

Giordano, D., J. K. Russell, and D. B. Dingwell (2008), Viscosity of magmatic liquids: A model, *Earth Planet. Sci. Lett.*, *271*, 123–134, doi:10.1016/j.epsl.2008.03.038.

Gonnermann, H. M., and M. Manga (2003), Explosive volcanism may not be an inevitable consequence of magma fragmentation, *Nature*, *426*, 432–435, doi:10.1038/nature02138.

Gonnermann, H. M., and M. Manga (2005), Flow banding in obsidian: A record of evolving textural heterogeneity during magma deformation, *Earth Planet. Sci. Lett.*, *236*, 135–147, doi:10.1016/j.epsl.2005.04.031.

Gonnermann, H. M., and M. Manga (2007), The fluid mechanics inside a volcano, *Annu. Rev. Fluid Mech.*, *39*, 321–356, doi:10.1146/annurev.fluid.39.050905.110207.

Hale, A. J., and G. Wadge (2008), The transition from endogeneous to exogeneous growth of lava domes with the development of shear bands, *J. Volcanol. Geotherm. Res.*, *171*, 237–257, doi:10.1016/j.jvolgeores.2007.12.016.

Hammer, J. E., K. V. Cashman, and B. Voight (2000), Magmatic processes revealed by textural and compositional trends in Merapi dome lavas, *J. Volcanol. Geotherm. Res.*, *100*, 165–192, doi:10.1016/S0377-0273(00)00136-0.

Herrmann, A. G., and D. Knake (1973), Coulometric method for the determination of total, carbonate and non-carbonate carbon in igneous, metamorphic and sedimentary rocks, *Z. Anal. Chem.*, *266*, 196–201, doi:10.1007/BF00428060.

Hess, K.-U., B. Cordonnier, Y. Lavallée, and D. B. Dingwell (2008), Viscous heating in rhyolite: An in situ experimental determination, *Earth Planet. Sci. Lett.*, *275*, 121–126, doi:10.1016/j.epsl.2008.08.014.

Holland, A. S. P., I. M. Watson, J. C. Phillips, L. Caricchi, and M. P. Dalton (2011), Degassing processes during lava dome growth: Insights from Santiaguito lava dome, Guatemala, *J. Volcanol. Geotherm. Res.*, *202*, 153–166, doi:10.1016/j.jvolgeores.2011.02.004.

Holtz, F., H. Behrens, D. B. Dingwell, and R. P. Taylor (1992a), Water solubility in aluminosilicate melts of haplogranite, composition at 2 kbar, *Chem. Geol.*, *96*, 289–302, doi:10.1016/0009-2541(92)90060-I.

Holtz, F., M. Pichavant, P. Barbey, and W. Johannes (1992b), Effects of H_2O on liquidus phase relations in the haplogranite system at 2 and 5 kbar, *Am. Mineral.*, *77*, 1223–1241.

Holtz, F., H. Behrens, D. B. Dingwell, and W. Johannes (1995), H_2O solubility in haplogranitic melts: Compositional, pressure and temperature-dependence, *Am. Mineral.*, *80*, 94–108.

Holtz, F., A. Becker, M. Freise, and W. Johannes (2001), The water-undersaturated and dry Qz-Ab-Or system revisited. Experimental results at very low water activities and geological implications, *Contrib. Mineral. Petrol.*, *141*, 347–357, doi:10.1007/s004100100245.

Holtzman, B. K., D. L. Kohlstedt, and J. P. Morgan (2005), Viscous energy dissipation and strain partitioning in partially molten rocks, *J. Petrol.*, *46*, 2569–2592, doi:10.1093/petrology/egi065.

Hui, H. J., and Y. X. Zhang (2007), Toward a general viscosity equation for natural anhydrous and hydrous silicate melts, *Geochim. Cosmochim. Acta*, *71*, 403–416, doi:10.1016/j.gca.2006.09.003.

Hui, H. J., Y. X. Zhang, Z. J. Xu, and H. Behrens (2008), Pressure dependence of the speciation of dissolved water in rhyolitic melts, *Geochim. Cosmochim. Acta*, *72*, 3229–3240, doi:10.1016/j.gca.2008.03.025.

Hui, H. J., Y. X. Zhang, Z. J. Xu, P. Del Gaudio, and H. Behrens (2009), Pressure dependence of viscosity of rhyolitic melts, *Geochim. Cosmochim. Acta*, *73*, 3680–3693, doi:10.1016/j.gca.2009.03.035.

Hurwitz, S., and O. Navon (1994), Bubble nucleation in rhyolitic melts: Experiments at high pressure, temperature, and water content, *Earth Planet. Sci. Lett.*, *122*, 267–280, doi:10.1016/0012-821X(94)90001-9.

Kameda, M., T. Katsumata, and M. Ichihara (2008), Deformation of bubbles in a highly viscous pipe flow, *Fluid Dyn. Res.*, *40*, 576–584, doi:10.1016/j.fluiddyn.2007.12.010.

Kerrick, D. M., and G. K. Jacobs (1981), A modified Redlich-Kwong equation for H_2O, CO_2 and H_2O-CO_2 mixtures at elevated pressures and temperatures, *Am. J. Sci.*, *281*, 735–767, doi:10.2475/ajs.281.6.735.

Ketcham, R. A., and W. D. Carlson (2001), Acquisition, optimization and interpretation of X-ray computed tomographic imagery: Applications to the geosciences, *Comput. Geosci.*, *27*, 381–400, doi:10.1016/S0098-3004(00)00116-3.

Klug, C., and K. V. Cashman (1996), Permeability development in vesiculating magmas: Implications for fragmentation, *Bull. Volcanol.*, *58*, 87–100, doi:10.1007/s004450050128.

Klug, C., K. V. Cashman, and R. Bacon (2002), Structure and physical characteristics of pumice from the climactic eruption of Mount Mazama (Crater Lake), Oregon, *Bull. Volcanol.*, *64*, 486–501, doi:10.1007/s00445-002-0230-5.

Kohlstedt, D. L., and B. K. Holtzman (2009), Shearing melt out of the Earth: An experimentalist's perspective on the influence of deformation on melt extraction, *Annu. Rev. Fluid Mech.*, *39*, 561–593.

Lange, R. A., and I. S. E. Carmichael (1987), Densities of Na_2O-K_2O-CaO-MgO-FeO-Fe_2O_3-Al_2O_3-TiO_2-SiO_2 liquids: New measurements and derived partial molar properties, *Geochim. Cosmochim. Acta*, *51*, 2931–2946, doi:10.1016/0016-7037(87)90368-1.

Laporte, D. (1994), Wetting behavior of partial melts during crustal anatexis: The distribution of hydrous silicic melts in polycrystalline aggregates of quartz, *Contrib. Mineral. Petrol.*, *116*, 486–499, doi:10.1007/BF00310914.

Larsen, J. F., M. H. Denis, and J. E. Gardner (2004), Experimental study of bubble coalescence in rhyolitic and phonolitic melts, *Geochim. Cosmochim. Acta*, *68*, 333–344, doi:10.1016/S0016-7037(03)00412-5.

Laumonier, M., L. Arbaret, A. Burgisser, and R. Champallier (2011), Porosity redistribution enhanced by strain localization in crystal-rich magmas, *Geology*, *39*, 715–718, doi:10.1130/G31803.1.

Lavallée, Y., K.-U. Hess, B. Cordonnier, and D. B. Dingwell (2007), Non-Newtonian rheological law for highly crystalline dome lavas, *Geology*, *35*, 843–846, doi:10.1130/G23594A.1.

Lavallée, Y., P. G. Meredith, D. B. Dingwell, K.-U. Hess, J. Wassermann, B. Cordonnier, A. Gerik, and J. H. Kruhl (2008), Seismogenic lavas and explosive eruption forecasting, *Nature*, *453*, 507–510, doi:10.1038/nature06980.

Lejeune, A. M., and P. Richet (1995), Rheology of crystal-bearing silicate melts: An experimental study at high viscosities, *J. Geophys. Res.*, *100*, 4215–4229, doi:10.1029/94JB02985.

Lejeune, A. M., Y. Bottinga, T. W. Trull, and P. Richet (1999), Rheology of bubble-bearing magmas, *Earth Planet. Sci. Lett.*, *166*, 71–84, doi:10.1016/S0012-821X(98)00278-7.

Lin, T.-J., and G.-M. Lin (2009), Mechanisms of in-line coalescence of two-unequal bubbles in a non-Newtonian fluid, *Chem. Eng. J.*, *155*, 750–756, doi:10.1016/j.cej.2009.09.019.

Llewellin, E. W., and M. Manga (2005), Bubble suspension rheology and implications for conduit flow, *J. Volcanol. Geotherm. Res.*, *143*, 205–217, doi:10.1016/j.jvolgeores.2004.09.018.

Llewellin, E. W., H. M. Mader, and S. D. R. Wilson (2002), The rheology of a bubbly liquid, *Proc. R. Soc. London A*, *458*, 987–1016, doi:10.1098/rspa.2001.0924.

Malfait, W., C. Sanchez-Valle, P. Ardia, E. Medard, and P. Lerch (2011), Compositional dependent compressibility of dissolved water in silicate glasses, *Am. Mineral.*, *96*, 1402–1409, doi:10.2138/am.2011.3718.

Manga, M., and M. Loewenberg (2001), Viscosity of magmas containing highly deformable bubbles, *J. Volcanol. Geotherm. Res.*, *105*, 19–24, doi:10.1016/S0377-0273(00)00239-0.

Mangan, M. T., L. Mastin, and T. W. Sisson (2004a), Gas evolution in eruptive conduits: Combining insights from high temperature and pressure decompression experiments with steady-state flow modeling, *J. Volcanol. Geotherm. Res.*, *129*, 23–36, doi:10.1016/S0377-0273(03)00230-0.

Mangan, M. T., T. W. Sisson, and W. B. Hankins (2004b), Decompression experiments identify kinetic controls on explosive silicic eruptions, *Geophys. Res. Lett.*, *31*, L08605, doi:10.1029/2004GL019509.

Marone, F., B. Muench, and M. Stampanoni (2010), Fast reconstruction algorithm dealing with tomography artifacts, in *Developments in X-ray Tomography VII*, edited by S. R. Stock, *Proc. SPIE*, *7804*, 780410, doi:10.1117/12.859703.

Mastin, L. G. (2005), The controlling effect of viscous dissipation on magma flow in silicic conduits, *J. Volcanol. Geotherm. Res.*, *143*, 17–28, doi:10.1016/j.jvolgeores.2004.09.008.

Mecklenburgh, J., and E. H. Rutter (2003), On the rheology of partially molten synthetic granite, *J. Struct. Geol.*, *25*, 1575–1585, doi:10.1016/S0191-8141(03)00014-2.

Mueller, S., E. W. Llewellin, and H. M. Mader (2010), The rheology of suspensions of solid particles, *Proc. R. Soc. London A*, *466*, 1201–1228, doi:10.1098/rspa.2009.0445.

Müller-Fischer, N., P. Tobler, M. Dressler, P. Fischer, and E. J. Windhab (2008), Single bubble deformation and breakup in simple shear flow, *Exp. Fluids*, *45*, 917–926, doi:10.1007/s00348-008-0509-1.

Murphy, M. D., R. S. J. Sparks, J. Barclay, M. R. Carroll, and L. G. Brewer (2000), Remobilization of andesite magma by intrusion of mafic magma at the Soufriere Hills Volcano, Montserrat, West Indies, *J. Petrol.*, *41*, 21–22.

Okumura, S., and S. Nakashima (2005), Molar absorptivities of OH and H_2O in rhyolitic glass at room temperature and at 400–600°C, *Am. Mineral.*, *90*, 441–447, doi:10.2138/am.2005.1740.

Okumura, S., M. Nakamura, and A. Tsuchiyama (2006), Shear-induced bubble coalescence in rhyolitic melts with low vesicularity, *Geophys. Res. Lett.*, *33*, L20316, doi:10.1029/2006GL027347.

Okumura, S., M. Nakamura, A. Tsuchiyama, T. Nakano, and K. Uesugi (2008), Evolution of bubble microstructure in sheared rhyolite: Formation of a channel-like bubble network, *J. Geophys. Res.*, *113*, B07208, doi:10.1029/2007JB005362.

Okumura, S., M. Nakamura, S. Takeuchi, A. Tsuchiyama, T. Nakano, and K. Uesugi (2009), Magma deformation may induce non-explosive volcanism via degassing through bubble networks, *Earth Planet. Sci. Lett.*, *281*, 267–274, doi:10.1016/j.epsl.2009.02.036.

Okumura, S., M. Nakamura, T. Nakano, K. Uesugi, and A. Tsuchiyama (2010), Shear deformation experiments on vesicular rhyolite: Implications for brittle fracturing, degassing, and compaction of magmas in volcanic conduits, *J. Geophys. Res.*, *115*, B06201, doi:10.1029/2009JB006904.

Pal, R. (2003), Rheological behavior of bubble-bearing magmas, *Earth Planet. Sci. Lett.*, *207*, 165–179, doi:10.1016/S0012-821X(02)01104-4.

Papale, P., R. Moretti, and D. Barbato (2006), The compositional dependence of the saturation surface of $H_2O + CO_2$ fluids in silicate melts, *Chem. Geol.*, *229*, 78–95, doi:10.1016/j.chemgeo.2006.01.013.

Passchier, C. W., and R. A. J. Trouw (2005), *Microtectonics*, 366 pp., Springer, Berlin.

Paterson, M. S. (1970), A high-pressure, high-temperature apparatus for rock deformation, *Int. J. Rock Mech. Min. Sci.*, *7*, 517–526, doi:10.1016/0148-9062(70)90004-5.

Paterson, M. S. (2001), A granular flow theory for the deformation of partially molten rock, *Tectonophysics*, *335*, 51–61, doi:10.1016/S0040-1951(01)00045-2.

Paterson, M. S., and D. L. Olgaard (2000), Rock deformation tests to large shear strains in torsion, *J. Struct. Geol.*, *22*, 1341–1358, doi:10.1016/S0191-8141(00)00042-0.

Paterson, S. R., J. Žák, and V. Janoušek (2008), Growth of complex sheeted zones during recycling of older magmatic units into younger: Sawmill Canyon area, Tuolumne batholith, Sierra Nevada, California, *J. Volcanol. Geotherm. Res.*, *177*, 457–484, doi:10.1016/j.jvolgeores.2008.06.024.

Petford, N. (2003), Rheology of granitic magmas during ascent and emplacement, *Annu. Rev. Fluid Mech.*, *31*, 399–427.

Petford, N. (2009), Which effective viscosity?, *Mineral. Mag.*, *73*, 167–191, doi:10.1180/minmag.2009.073.2.167.

Petford, N., and M. A. Koenders (2003), Shear-induced pressure changes and seepage phenomena in a deforming porous layer: I, *Geophys. J. Int.*, *155*, 857–869, doi:10.1111/j.1365-246X.2003.02076.x.

Pieri, M., L. Burlini, K. Kunze, I. Stretton, and D. L. Olgaard (2001), Rheological and microstructural evolution of Carrara marble with high shear strain: Results from high temperature torsion experiments, *J. Struct. Geol.*, *23*, 1393–1413, doi:10.1016/S0191-8141(01)00006-2.

Ranalli, G. (1995), *Rheology of the Earth*, 2nd ed., 413 pp., Chapman and Hall, London.

Rust, A. C., and K. V. Cashman (2007), Multiple origins of obsidian pyroclasts and implications for changes in the dynamics of the 1300 B.P. eruption of Newberry Volcano, USA, *Bull. Volcanol.*, *69*, 825–845, doi:10.1007/s00445-006-0111-4.

Rust, A. C., and K. V. Cashman (2011), Permeability controls on expansion and size distributions of pyroclasts, *J. Geophys. Res.*, *116*, B11202, doi:10.1029/2011JB008494.

Rust, A. C., and M. Manga (2002a), Effects of bubble deformation on the viscosity of dilute suspensions, *J. Non-Newtonian Fluid Mech.*, *104*, 53–63, doi:10.1016/S0377-0257(02)00013-7.

Rust, A. C., and M. Manga (2002b), Bubble shapes and orientations in low Re simple shear flow, *J. Colloid Interface Sci.*, *249*, 476–480, doi:10.1006/jcis.2002.8292.

Rust, A. C., K. V. Cashman, and P. J. Wallace (2004), Magma degassing buffered by vapor flow through brecciated conduit margins, *Geology*, *32*, 349–352, doi:10.1130/G20388.2.

Rutter, E. H., and D. H. K. Neumann (1995), Experimental deformation of partially molten Westerly granite under fluid-absent conditions, with implications for the extraction of granitic magmas, *J. Geophys. Res.*, *100*, 15,697–15,715, doi:10.1029/94JB03388.

Rutter, E. H., K. H. Brodie, and D. H. Irving (2006), Flow of synthetic, wet, partially molten "granite" under undrained conditions: an experimental study, *J. Geophys. Res.*, *111*, B06407, doi:10.1029/2005JB004257.

Schulze, F., H. Behrens, F. Holtz, J. Roux, and W. Johannes (1996), The influence of H_2O on the viscosity of a haplogranitic melt, *Am. Mineral.*, *81*, 1155–1165.

Schwarzenbach, E. M. (2011), Serpentinization, fluids and life: Comparing carbon and sulfur cycles in modern and ancient environments, PhD thesis, Inst. Geochem. Petrol., ETH-Zurich, Zurich.

Smith, J. V. (1997), Shear thickening dilatancy in crystal-rich flows, *J. Volcanol. Geotherm. Res.*, *79*, 1–8, doi:10.1016/S0377-0273(97)00020-6.

Sparks, R. S. J. (1997), Causes and consequences of pressurization in lava dome eruptions, *Earth Planet. Sci. Lett.*, *150*, 177–189, doi:10.1016/S0012-821X(97)00109-X.

Sparks, R. S. J., S. R. Tait, and Y. Yanev (1999), Dense welding caused by volatile resorption, *J. Geol. Soc.*, *156*, 217–225, doi:10.1144/gsjgs.156.2.0217.

Stampanoni, M., et al. (2006), Trends in synchrotron-based tomographic imaging: The SLS experience, in *Developments in X-ray Tomography V*, edited by U. Bonse, *Proc. SPIE*, *6318*, 63180M, doi:10.1117/12.679497.

Stasiuk, M. V., J. Barclay, M. Carroll, C. Jaupart, C. Ratte, and R. S. J. Sparks (1996), Degassing during magma ascent in the Mule Creek vent (USA), *Bull. Volcanol.*, *58*, 117–130, doi:10.1007/s004450050130.

Stein, D. J., and F. J. Spera (1992), Rheology and microstructure of magmatic emulsions: Theory and experiments, *J. Volcanol. Geotherm. Res.*, *49*, 157–174, doi:10.1016/0377-0273(92)90011-2.

Stein, D. J., and F. J. Spera (2002), Shear viscosity of rhyolite-vapor emulsions at magmatic temperatures by concentric cylinder rheometry, *J. Volcanol. Geotherm. Res.*, *113*, 243–258, doi:10.1016/S0377-0273(01)00260-8.

Stone, H. A. (1994), Dynamics of drop deformation and breakup in viscous fluids, *Annu. Rev. Fluid Mech.*, *26*, 65–102, doi:10.1146/annurev.fl.26.010194.000433.

Taylor, G. I. (1934), The formation of emulsions in definable fields of flow, *Proc. R. Soc. London, Ser. A*, *146*, 501–523, doi:10.1098/rspa.1934.0169.

Thies, M. (2002), Herstellung und rheologische Eigenschaften von pörosen Kalk-Natron-Silicatschmelzen, PhD thesis, Prozesswissenschaften, Univ. of Berlin, Berlin.

Tuffen, H., D. B. Dingwell, and H. Pinkerton (2003), Repeated fracture and healing of silicic magma generate flow banding and earthquakes?, *Geology*, *31*, 1089–1092, doi:10.1130/G19777.1.

van der Molen, I., and M. S. Paterson (1979), Experimental deformation of partially melted granite, *Contrib. Mineral. Petrol.*, *70*, 299–318, doi:10.1007/BF00375359.

Webb, S. L., and D. B. Dingwell (1990a), Non-Newtonian rheology of igneous melts at high stresses and strain rates: Experimental results for rhyolite, andesite, basalt, and nephelinite, *J. Geophys. Res.*, *95*, 15,695–15,701, doi:10.1029/JB095iB10p15695.

Webb, S. L., and D. B. Dingwell (1990b), The onset of non-Newtonian rheology of silicate melts: A fiber elongation study, *Phys. Chem. Miner.*, *17*, 125–132, doi:10.1007/BF00199663.

Wright, H. M. N., and R. F. Weinberg (2009), Strain localization in vesicular magma: Implications for rheology and fragmentation, *Geology*, *37*, 1023–1026, doi:10.1130/G30199A.1.

Wright, H. M. N., J. J. Roberts, and K. V. Cashman (2006), Permeability of anisotropic tube pumice: Model calculations and measurements, *Geophys. Res. Lett.*, *33*, L17316, doi:10.1029/2006GL027224.

Wright, H. M. N., K. V. Cashman, E. H. Gottesfeld, and J. J. Roberts (2009), Pore structure of volcanic clasts: Measurements of permeability and electrical conductivity, *Earth Planet. Sci. Lett.*, *280*, 93–104, doi:10.1016/j.epsl.2009.01.023.

Yoshimura, S., and M. Nakamura (2008), Diffusive dehydration and bubble resorption during open-system degassing of rhyolitic melts, *J. Volcanol. Geotherm. Res.*, *178*, 72–80, doi:10.1016/j.jvolgeores.2008.01.017.

Yoshimura, S., and M. Nakamura (2010), Fracture healing in a magma: An experimental approach and implications for volcanic seismicity and degassing, *J. Geophys. Res.*, *115*, B09209, doi:10.1029/2009JB000834.

Zhang, Y. X., Z. J. Xu, and Y. Liu (2003), Viscosity of hydrous rhyolitic melts inferred from kinetic experiments, and a new viscosity model, *Am. Mineral.*, *88*, 1741–1752.